

6-25-2010

Analysis and modeling of phase noise in LOCSET and the AFRL high power fiber test bed

Don Seeley

Follow this and additional works at: https://digitalrepository.unm.edu/ose_etds

Recommended Citation

Seeley, Don. "Analysis and modeling of phase noise in LOCSET and the AFRL high power fiber test bed." (2010).
https://digitalrepository.unm.edu/ose_etds/39

This Thesis is brought to you for free and open access by the Engineering ETDs at UNM Digital Repository. It has been accepted for inclusion in Optical Science and Engineering ETDs by an authorized administrator of UNM Digital Repository. For more information, please contact disc@unm.edu.

Donald David Seeley

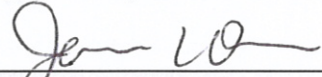
Candidate

Physics

Department

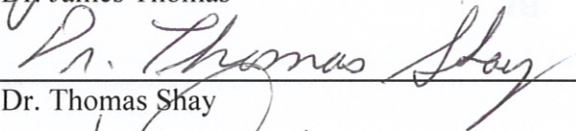
This thesis is approved, and it is acceptable in quality and form for publication:

Approved by the Thesis Committee:



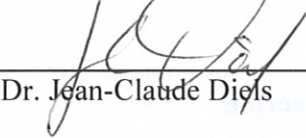
Dr. James Thomas

, Co-Chairperson



Dr. Thomas Shay

, Co-Chairperson



Dr. Jean-Claude Diels

, Member

**Analysis and Modeling of Phase Noise in LOCSET and the
AFRL High Power Fiber Test Bed**

BY

Donald David Seeley

**Bachelor of Science in Electrical Engineering
University of New Mexico
1982**

THESIS

Submitted in Partial Fulfillment of the
Requirements for the Degree of

Master of Science

Optical Science and Engineering

The University of New Mexico
Albuquerque, New Mexico

May, 2010

ACKNOWLEDGMENTS

The experience of returning to school to pursue a Master's degree after so many years was difficult but had a very positive impact on my career and has enriched me both professionally and personally. I thank all my instructors, fellow students, and co-workers who supported this adventure.

I heartily acknowledge Dr. Shay, my thesis advisor, for providing me an exciting and relevant research topic and for the continuous support provided through the many months of researching and writing this paper. His tremendous knowledge of the subject is most impressive.

I thank my graduate advisor, Dr. Thomas, for the sound guidance and support; Dr. Diels for serving on my committee and a special thanks to Dr. Rudolph, who encouraged me many years ago that I could achieve this goal.

I thank Ben Pulford for the advice, support and, especially, the data to make this research complete, interesting, and worthwhile, and my editor, Halee Baird, for the many hours she spent to correct my grammar, punctuation, and spelling.

I thank my children, Autumn, Kevin and Katie. Thank you so much for your understanding and support as I took so much time away from you as a father to reach this goal. I thank my mother for giving me the confidence to believe in myself and for teaching me early in life the amazing things I could accomplish with hard work and perseverance. I love you so much. Lastly, most special thanks to the love of my life, my wife, partner and best friend: Nancy, thank you for standing by me through these long years, your love and support are the greatest gifts of all.

**Analysis and Modeling of Phase Noise in LOCSET and the
AFRL High Power Fiber Test Bed**

BY

Donald David Seeley

ABSTRACT OF THESIS

Submitted in Partial Fulfillment of the
Requirements for the Degree of
Master of Science

Optical Science and Engineering

The University of New Mexico
Albuquerque, New Mexico

May, 2010

**Analysis and Modeling of Phase Noise in LOCSET and the AFRL High
Power Fiber Test Bed**

by

Donald David Seeley

Bachelor of Science in Electrical Engineering, University of New Mexico, 1982

Master of Science in Optical Science and Engineering, University of New Mexico, 2010

ABSTRACT

High power ytterbium doped fiber amplifier arrays in a Master Oscillator-Power Amplifier configuration and the phase noise in such a system is studied. An effective method of coherently combining the elements in such an array is LOCSET. A potential drawback to the effectiveness in LOCSET is the increased phase noise that is present in higher power amplifiers. The theory of LOCSET and the impact of this noise on LOCSET is researched. A mathematical model of model is developed to study this issue. The theory of phase noise and linewidth broadening due to amplified spontaneous emission is presented. Previous research on the magnitude of phase noise in ytterbium doped fiber amplifier is investigated and compared to the phase noise measurements at the AFRL high power fiber test bed. Phase noise measurements from the AFRL high power fiber test bed are provided to support this research and these data are analyzed in both an open loop configuration and when the control loop is closed by LOCSET. The ability of LOCSET to reduce this noise is analyzed and compared to the predicted results from LOCSET model.

TABLE OF CONTENTS

LIST OF FIGURES	viii
LIST OF TABLES	xi
CHAPTER 1 INTRODUCTION	1
CHAPTER 2 THEORY	12
Section 2.1 Ytterbium Fiber Laser Amplifiers	12
Section 2.2 Phase Noise due to Amplified Spontaneous Emission	16
Section 2.3 Previous Phase Noise Experiments.....	21
Section 2.4 Theory of LOCSET.....	25
Section 2.5 LOCSET Two-Element Analysis	37
Section 2.6 Coherent Combination Efficiency	39
CHAPTER 3 LOCSET MODEL.....	41
CHAPTER 4 DESCRIPTION OF EXPERIMENTS AND EQUIPMENT	44
Section 4.1 High Power Fiber Amplifier Laboratory	44
Section 4.2 Phase Noise Experiments.....	47
CHAPTER 5 RESULTS	50
Section 5.1 Analysis of Open Loop Phase Transient and Noise Data.....	50
Section 5.2 Analysis of Open Loop Phase Noise Power Spectrum.....	58
Section 5.3 Modeling of Open Loop Phase Noise and LOCSET Bandwidth.....	60
Section 5.4 Analysis of Closed Loop Data and LOCSET Model Results.....	63
Section 5.5 Results of Two Element Analysis.....	70
CHAPTER 6 CONCLUSION AND FUTURE WORK	77
Section 6.1 Summary of Work and Results.....	77

Section 6.2 Suggestions for Future Work	82
APPENDICES	84
APPENDIX 1 DERIVATION OF LOCSET	84
APPENDIX 2 LOCSET ELECTRONIC SCHEMATIC.....	93
APPENDIX 3 MATHCAD PROGRAMS.....	95
REFERENCES	114

LIST OF FIGURES

Figure 1.1 Spectral beam combining..	4
Figure 1.2 Spectral beam combining method using two gratings and power amplifier array...	5
Figure 1.3 Coherent beam combining method using active phasing.....	6
Figure 2.1 Typical fiber amplifier	12
Figure 2.2 Energy levels of Ytterbium..	13
Figure 2.3 Absorption and emission cross sections of Yb.....	14
Figure 2.4 Stimulated Brillouin Scattering.....	15
Figure 2.5 Phasor diagram showing phase deviation $\delta\phi$ due to ASE.....	17
Figure 2.6 Coherent beam combining method using active phasing	25
Figure 2.7 Self synchronous LOCSET control loop block diagram for two elements....	31
Figure 2.8 Self synchronous LOCSET control loop block diagram for the i th element...33	33
Figure 2.9 Linear control loop model for self-synchronous LOCSET	34
Figure 2.10 Strehl ratio plot of RMS phase deviation for 16 elements	40
Figure 4.1 Nufern Amplifier in AFRL High Power Fiber Laser Test Bed.....	44
Figure 4.2 Arrangement of Amplifier in AFRL High Power Fiber Laser Test Bed.....	44
Figure 4.3 Schematic of AFRL fiber laser amplifier.....	45
Figure 4.4 Experimental set up for open loop phase noise measurement.....	47
Figure 4.5 Experimental set up for closed loop phase noise measurement.....	48
Figure 5.1 Open loop phase noise data versus time for three experiments.....	50
Figure 5.2 Representative open loop phase noise versus time for 30 seconds.....	51
Figure 5.3 Data points of the slope of the phase transient data versus time.....	52

Figure 5.4 Steady state phase noise versus time.....	53
Figure 5.5 Phase noise versus time for steady state operation and after turn off of the amplifier.	54
Figure 5.6 Phase noise versus time for short time span in steady state.....	55
Figure 5.7 Phase structure function curve for open loop phase noise in steady state.....	56
Figure 5.8 Phase noise versus time over very short time duration	57
Figure 5.9 Phase noise power spectrum versus frequency for three spectra.....	58
Figure 5.10 Phase noise power spectrum for 0-45 seconds, 45-200 seconds and 0-200 seconds.....	59
Figure 5.11 Actual open loop phase noise and LOCSET modeled closed loop phase noise versus frequency.....	60
Figure 5.12 LOCSET Control Loop Gain for 2 elements and 16 elements.....	61
Figure 5.13 Intensity of two beams with random phase versus time.....	63
Figure 5.14 Intensity of two high power beams with phases locked by LOCSET	63
Figure 5.15 Intensity of a single high power beam..	64
Figure 5.16 Intensity of single reference (low power) beam only.....	64
Figure 5.17 Phase noise frequency spectrum for closed loop phase noise..	66
Figure 5.18 Modeled closed loop data, Closed loop data calculated from intensity data and open loop data plotted versus frequency.....	67
Figure 5.19 Power detector signal with no light.....	68
Figure 5.20 Two element analysis. High frequency and low frequency.....	71
Figure 5.21 Two element analysis. Low frequency and high frequency	72
Figure 5.22 Two element analysis. Step function and low frequency.....	73

Figure 5.23 Two element analysis. Low frequency and step function.....	74
Figure 5.24 Two element analysis. Step function and high frequency.....	75
Figure 5.25 Two element analysis. High frequency and step function.....	76

LIST OF TABLES

Table 3.1 Electronic Constants used in LOCSET Model and Experiments	42
Table 5.1 Results of Linear Regression Calculation on Phase Transient Data.....	52
Table 5.2 Cases examined in two element analysis.....	70

I. Introduction

Following the invention of the laser a half century ago, an amazingly wide variety of applications have been discovered for these devices. Whether it is communications, entertainment, surgery or the checkout stand, lasers have many very successful applications and have led to an improvement in quality of life and personal convenience. The lasers involved in most of these applications are at relatively low to moderate powers, but certain applications require or can be more effective with much higher powers. High power welding lasers are employed in a variety of manufacturing operations with power levels of several kilowatts to even tens of kilowatts. A variety of military applications utilizing lower power lasers have been successfully developed and deployed, and applications for high power lasers have been investigated for several decades, but high power military laser weapons are still being researched and developed and have not been deployed. Missions being considered require very high powers focused at long ranges from several to hundreds of kilometers, so the qualities of the lasers differ significantly from those of the welding lasers in that a very high quality, near-diffraction limited beam is required so the energy can be focused to rather small areas at those ranges. Lasers with these qualities, when integrated on a military platform with a beam control system, hold the potential to offer unique advantages over conventional kinetic weapons. In order for a weapon to be deployed, other military considerations such as the integration of the weapon with the mobile platforms and the logistic supportability of the weapon in the battlefield environment must also be considered. Chemical laser technology has achieved very high powers with reasonably good beam quality and has demonstrated a military capability [1], but these chemical lasers suffer from

large volume and weight, making them impractical for integration on a mobile platform, and require dangerous and exotic chemicals, making them logistically unsuitable for military applications. Consequently, the chemical laser technology remains undeployed.

What is desired is a robust, small, light-weight and logistically suitable device. An all electrically powered laser with excellent electrical to optical efficiency is being seriously considered as a potential solution [2]. A highly efficient device will not only reduce the prime power requirements but also reduce the thermal management burden, thus effectively reducing the size and weight of the total system. A prime candidate for an electrical laser is the diode pumped solid state laser, which has demonstrated remarkable electrical to optical efficiency compared to other electrically-driven laser devices. Ongoing research recently completed is the development of laboratory devices exceeding 100 kW [3], an entry level power goal for the missions under consideration. These devices are developed with electrical to optical efficiency nearing 17%. The architectures vary, but the most mature technologies are diode-pumped neodymium slab lasers. Newer technology being investigated that can provide even better efficiency is the high power fiber laser. In particular, Ytterbium Doped Fibers Lasers (YDFL) have the potential to provide some substantial improvements in efficiency over electrically-driven neodymium slab architectures. This is due to the excellent overlap of the pump power and laser mode in the fiber laser architecture and also because the ytterbium quantum defect is less than that of neodymium. These effects allow the YDFL to produce about twice the electrical efficiency as neodymium slab lasers. A common and effective architecture is the Master Oscillator Fiber Amplifier (MOPA) configuration, which allows the amplified output beam to maintain the very good laser characteristics of the master oscillator (MO). Such a MO would have a single mode output for excellent beam quality, a

specific and controlled polarization and a narrow spectral linewidth to provide for beam combination, which is discussed below.

This improvement, along with the continuing advancement of diode efficiency, when realized on an HEL system on a tactical platform, could offer enough improvements in efficiency to lead to the reduced size and weight to perhaps finally realize a deployed laser weapon system. The limitation of fiber lasers, however, is the average power that can be obtained from a single device. Theoretical limits suggest this is at the 5-10 kilowatt range. However, several schemes have been proposed to combine the outputs of fiber lasers to produce powers at the hundreds of kilowatt regime. Over the last few years, several technologies for combining multiple fiber lasers have begun to look promising, but much more research and development is required to fully understand which approaches have the best potential for a given application and have the capability to efficiently scale to high powers.

Toward this goal, some of the more promising techniques that have been proposed and demonstrated at low powers include wavelength combination or spectral beam combining, polarization combination, temporal multiplexing, Talbot re-imaging and active co-phasing of coherent beams. However, these techniques introduce new challenges of their own, depending on the particular combining technique, such as the coherence of the resultant beam, beam spatial quality, the efficiency of the combiner, the ability to focus the combined beams and the number of beams that can be reliably and practically combined. To combine fibers to a very high level would require a high number of fiber lasers, each with high power. Assuming near perfect combining efficiency, a nominal solution for a 100 kW device would be 100 elements at 1 kW for a near 100 kW system. These numbers can vary greatly

depending on the ability to scale single fibers to high power, which would make the number of elements smaller and would perhaps make the combining issues simpler, but introduces the issue of dealing with high power single apertures, which would likely introduce other problems. On the other hand, increasing the number of elements to be combined will create increased complexity in the combining scheme but would perhaps avoid some high power issues until the final output is created.

Arguably the two most popular beam combination methods currently being researched are spectral beam combining and active coherent beam combining. Spectral beam combining involves operating each individual fiber laser at a slightly different wavelength and then combining the outputs incoherently by use of a dispersive element. In this method the beams are overlaid one on the other and share the same beam path out of the output mirror. A typical geometry is shown in Figure 1.

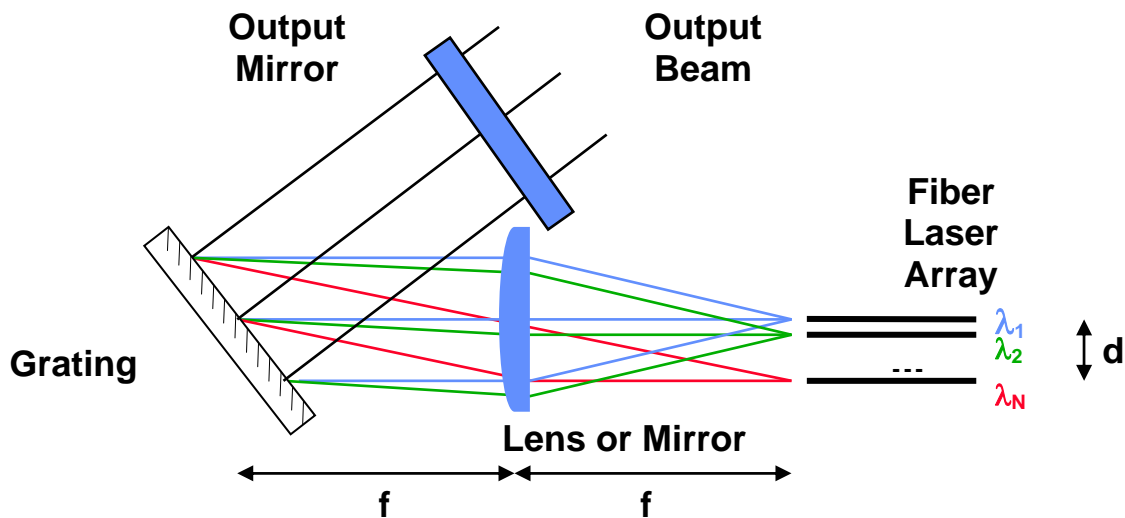


Figure 1.1. Spectral beam combining. [4]

In this example, each individual fiber laser shares a common output mirror through the use of the grating. The output of each fiber is spatially combined at the grating and feedbacks to the fiber lasers from the output mirror. Another architecture is to replace the output mirror with a mirror and output a portion of the fiber laser into a power amplifier as shown in Figure 1.2. The output of the fiber amplifiers are then combined with a grating that

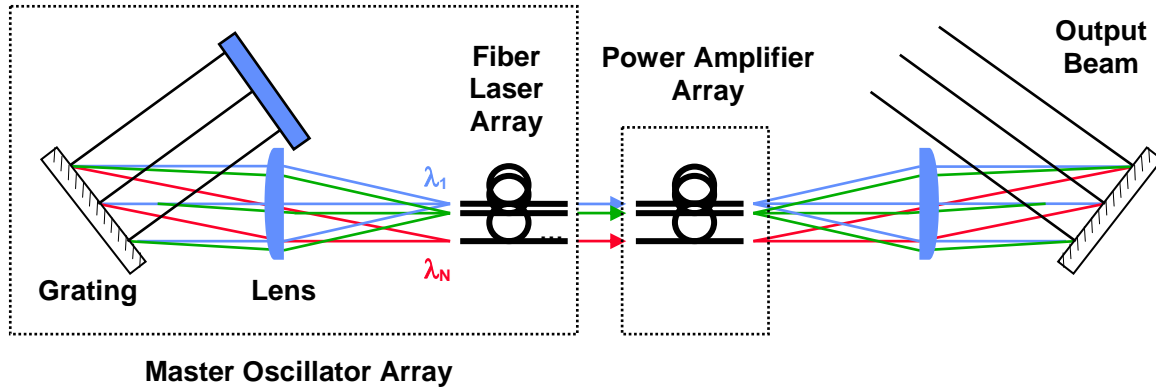


Figure 1.2. Spectral beam combining method using two gratings and power amplifier array. [4]

is identical to the grating within the cavity of the fiber lasers. One equation that governs the behavior of this system (Figure 1.1) is

$$d = f \Delta \lambda \left(\frac{d\beta}{d\lambda} \right) \quad (1)$$

where d is the distance shown that is the length of the linear fiber array, $\Delta \lambda$ is the wavelength separation of the individual fibers, f is the focal length of the lens and $d\beta/d\lambda$ is the angular dispersion of the grating. No phasing or considerations similar to coherent combining are required, but controlling the wavelength separation between the individual fibers is very important. In order to scale this architecture to a high number of elements, the linewidth of the individual fibers must be controlled to a very small $\Delta \lambda$ and still must remain within the

requirement set by the resolution of the grating. This is a significant engineering challenge for this combining approach. Reducing the number of elements by increasing the power in each element introduces other issues. Phase noise from the fiber amplifiers will result in a spectral broadening so severe that phase noise increase from increased power in single fiber amplifiers could be an issue and must be investigated.

The active coherent beam combining approach combines the beams by actively co-phasing all the beams together and requires the beams to be mutually coherent so combination occurs by constructive interference. This requires the MOPA configuration. In addition to being coherent, the beams must also be of the same polarization in order to combine. A novel approach, and the one studied for this paper, is Locking of Optical Coherence by Single-detector Electronic-frequency Tagging (LOCSET) and is shown in

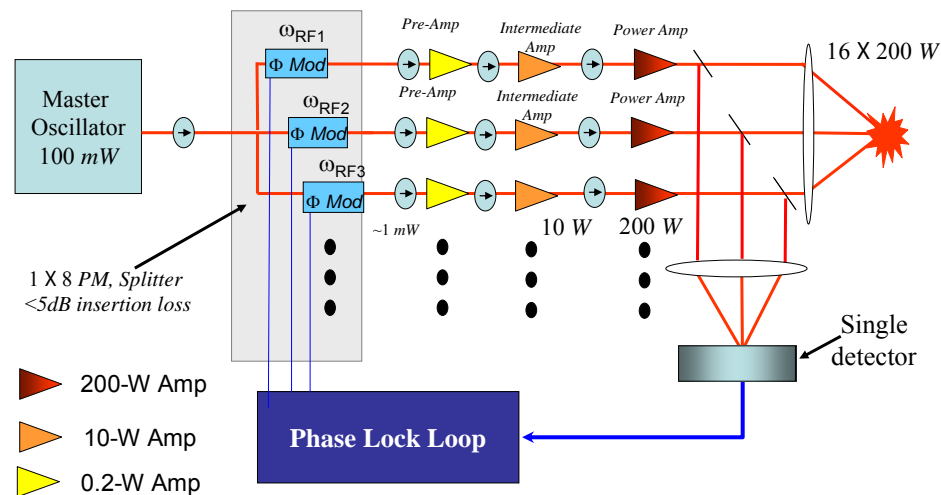


Figure 1.3. Coherent beam combining method using active phasing (LOCSET). [5]

Figure 1.3. The master oscillator provides the coherence source for each individual fiber amplifier to be combined, and its signal is split among those amplifiers. Individual power oscillators cannot be used since each fiber laser must be coherently combined; thus, only power amplifiers driven by a common master oscillator can be used. This ensures each fiber amplifier is coherent with the other fiber amplifier. The master oscillator is split into an array of elements, and following the splitter, each element has an individual electro-optic phase modulator to provide piston phase control. Following the electro-optic phase modulator, the signal is sent into each fiber amplifier element. A sample of the output of each fiber amplifier is taken and fed into a single detector in the example shown, where the phase of each element is detected relative to the ensemble average of the other array elements phase; in other configurations, multiple detectors, one for each amplifier are used and phase information is compared to a reference beam from the MO. In LOCSET, which is later described in much further detail, each element is provided a unique RF phase modulation, and phase control electronics sense the phase of each amplifier through the single detector and adjust the phase of each element to be equal so that all amplifiers output the same phase. In this way the phase of each power amplifier chain is identical, thus providing for coherent combining of the beams. Clearly, the methods of active coherent beam combining need good phase information, and very noisy phase will be problematic. As mentioned previously, for spectral beam combining, the phase noise will lead to linewidth broadening, which will be problematic for that method. Thus, understanding and controlling phase noise is an important aspect of beam combining and is the motivation of this research.

From the discussions of the two beam combining techniques described above, both require consideration of the phase noise on the individual fiber amplifiers. Phase noise can

be viewed as random changes in phase. If the phase noise spectrum is mostly at frequencies too high to be controlled by the feedback loop in the coherent combination schemes, then that phase noise cannot be corrected and a loss of coherent combination efficiency will result. On the other hand, when temporally averaged, phase noise can be viewed as a spectral broadening of the fiber amplifier with the resultant impact on the spectral combination techniques to be a loss of bandwidth as the linewidth of each of the individual fiber amplifiers to be combined has now increased. In severe cases, of linewidth broadening, accurate path length matching may be necessary.

As discussed above, for coherent combination to work well, the individual lasers must be coherent and of the same phase. To achieve the required coherent combination, the phase errors between individual fibers must be able to be controlled within a small fraction of the wavelength. Thus, of interest is the magnitude of the phase noise, that is, the increase of linewidth and the frequency at which the noise occurs. These are required in order to design a servo system that can manage this noise within the levels of the system requirements. The minimum linewidth is controlled by the master oscillator of the system and then is increased by the phase noise of the amplifiers. Several experiments have shown that the phase noise of low power and even moderate power amplifiers is well within what seems to be reasonable system requirements. Based on the data obtained from their experiments, this phase noise in an individual fiber varies from -0.2 to $+0.2$ waves for a 1 watt fiber and 0.1 to 0.4 waves for a 10 watt fiber [6]. The frequency of this noise was mostly below 10 kHz but did increase with the higher powers. For that system, a 10 kHz phase correction servo would need 10 kHz of bandwidth. However, this research was conducted at power levels of individual amplifiers

well below 100 W, and previous research has shown that phase noise increases as amplifier power increases [7].

Other than the inherent noise in the master oscillator, the source for phase noise can be broken down into three categories: phase noise resulting from the amplification process, phase noise due to the heating of the fiber and phase noise caused by mechanical disturbances of the amplifiers from the external environment. The first can be characterized by the parameters of the master oscillator and the pump. The research discussed above and other research suggests that even when the environment is kept as pristine as possible, the phase noise or spectral broadening due to noise in the amplification process is typically well below the theoretical values estimated by the equation [8]:

$$\delta\nu \approx \sqrt{\frac{B_0^2 n_{sp}^2 h\nu \Delta\nu_s (G-1)^2}{4\pi G P_s^{in}}} \quad (2)$$

where $\delta\nu$ is the spectral broadening due to phase noise, n_{sp} is the spontaneous emission factor of the amplifier, $h\nu$ is the average energy of the photons, G is the gain of the amplifier, $\Delta\nu_s$ is the full width half maximum of the laser signal spectrum, B_0 is the optical bandwidth of the laser and P_s^{in} is the input signal power of the optical amplifier. Heating of the fiber has been characterized by a slow change in phase eventually reaching steady state. The noise due to the mechanical disturbances from the environment may play a larger role in phase noise than the other processes, especially when operated on a military platform in a battlefield environment; however, little, if any, research has been done to understand and characterize the phase noise resulting from known mechanical disturbances.

It should now be clear that phase noise in high power fiber amplifiers is an important consideration in the development of high power fiber laser systems. The motivation and

objectives of this research are to characterize phase noise in high power (150 watt) fiber amplifiers and greater (as available), model the effect of phase noise on the LOCSET beam combining technique and assess the impact to the performance of LOCSET due to this phase noise and phase noise that may be inherent in higher power fiber amplifiers.

As YDFAs have matured, a test bed consisting of sixteen 150 watt YDFAs is being assembled at the Air Force Research Laboratory Directed Energy Directorate (AFRL-RD) on Kirtland Air Force Base, New Mexico. One of the major research efforts being undertaken by AFRL-RD with these amplifiers is to investigate the LOCSET beam combining technique. As part of this research, the open loop phase noise of the amplifiers is being measured and, after LOCSET has been applied to the amplifiers, the closed loop intensity from two elements is being measured. The open loop phase noise will be analyzed to understand the phase transient due to heating effects of the fiber and the phase noise due to the inherent mechanical disturbance of the system. The closed loop intensity data will be analyzed by the laboratory and closed loop phase noise will be analyzed. In addition, a computer model of the LOCSET beam combining system will be developed. The measured open loop phase noise will be used as the input to the model, and the closed loop phase noise after LOCSET will be the resultant output. The results of this model will be compared to the data obtained from the test bed, and the model will be validated for the fiber amplifier test bed.

In summary, the goal of this research is to understand the phase noise environment in high power fiber amplifiers, how it scales with increasing power and the effect of this phase noise environment on the LOCSET beam combination technique. In particular, the phase noise of the AFRL-RD high power fiber amplifier test bed with inherent and induced

mechanical disturbances will be analyzed and characterized and compared to previous research. A mathematical model of the LOCSET beam combining technique will be programmed and validated to provide a simulation test bed to analyze how LOCSET responds to various phase noise environments. For the first time, a fully coupled model for the LOCSET beam combining technique is developed and presented.

II. Theory

Section 2.1. Ytterbium Fiber Laser Amplifiers

This research utilizes the results of experiments using high power Ytterbium Doped Fiber Amplifiers (YDFA) in a silica glass host, which is the most common host for a fiber medium. Although erbium is widely used for commercial applications in the telecommunications industry, ytterbium (Yb) fiber lasers are seeing wide use for high power laser applications for a variety of reasons discussed here [9]. A schematic of a typical optical fiber amplifier is shown in Figure 2.1. In order to allow for coherent beam combination, the master oscillator must be polarized and of a fairly narrow linewidth and fiber must be polarization maintaining.

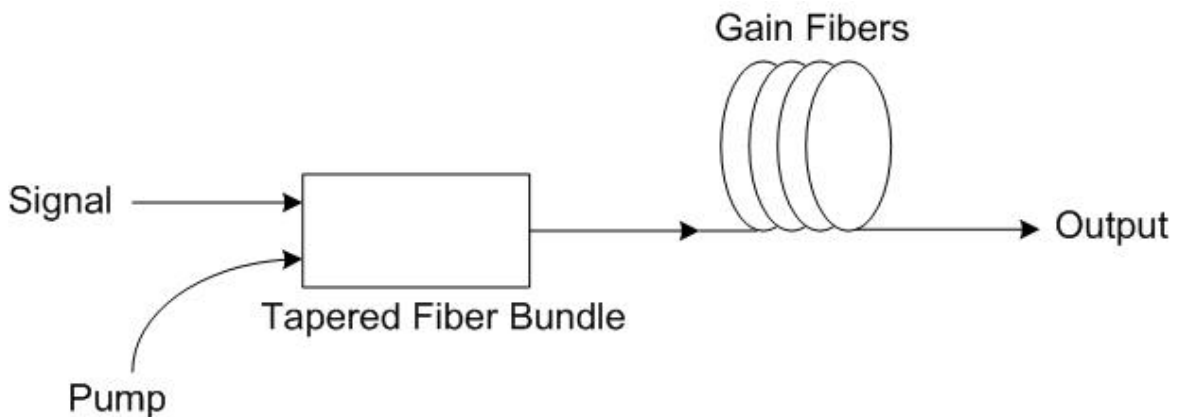


Figure 2.1. Typical fiber amplifier with co-pumping scheme using a tapered fiber bundle as the coupling source for pump light into the cladding.

Yb has a very broad gain bandwidth from ~ 975 to ~ 1200 nm and can be pumped to very high output powers because high doping levels are possible. Figure 2.2 shows the energy levels of ytterbium and the lasing and pumping frequencies.

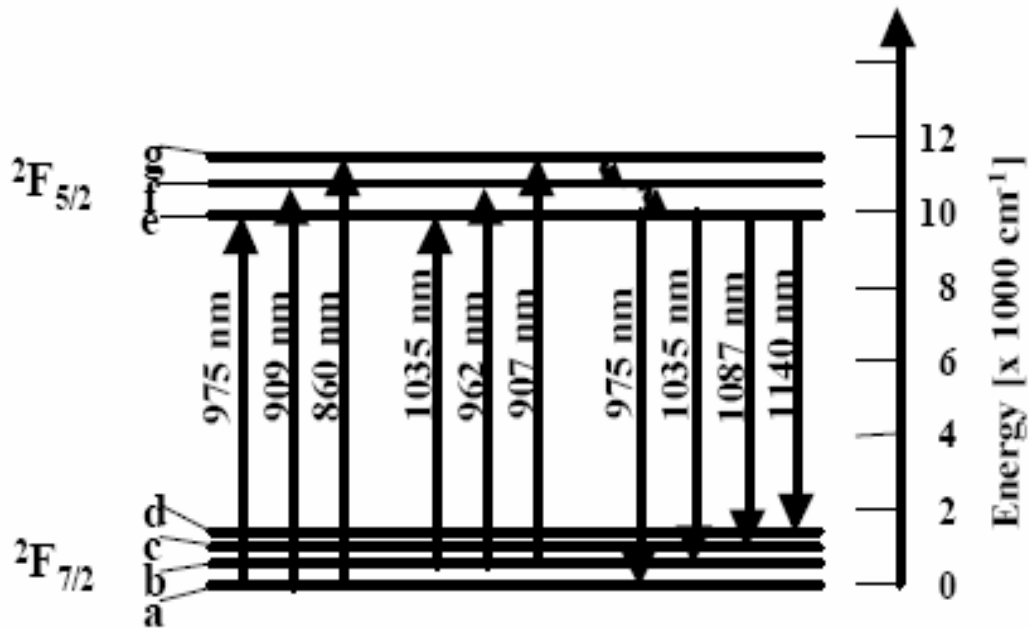


Figure 2.2 Energy levels of Ytterbium.

YDFL have several advantages for high power applications. The lasing is as shown between the excited state $^2F_{5/2}$ manifold and the $^2F_{7/2}$ ground state manifold, which consists of three and four sub manifolds respectively. These close energy levels provide for quasi-three-level lasing. Due to the absence of other higher energy levels, excited state absorption of pump or signal energy occurs in Yb. This, combined with a very low quantum defect with pump wavelength at 915 - 975 nm and lasing at ~ 1080 nm, achieves very efficient energy extraction from the amplifiers with a strong saturating signal. Photon conversion efficiencies of 85 to 90% are achievable as well as excellent slope efficiencies, which have been measured at $>80\%$. Excellent beam quality is achieved with near diffraction limited output. A broad absorption spectrum (~ 40 nm) allows for a wide choice of pump wavelengths, and a large saturation fluence and long fluorescence lifetime are other advantages of Yb for high power fiber amplifiers. Figure 2.3 shows the absorption and emission cross sections of Yb.

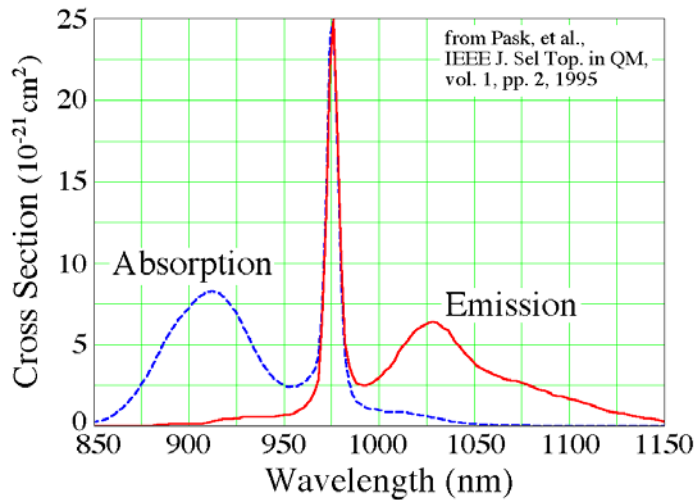


Figure 2.3. Absorption (blue dashed) and emission (red solid) cross sections of Yb in germanosilicate glass.

An important design change for higher power applications that is used for YDFA and other high power fiber amplifiers is cladding pumping. This is where the pump light is injected into the cladding of the fiber rather than the core. The signal is still injected into the core and the modes of the inner cladding have some overlap with the modes of the core so that the pump photons reach the core and are absorbed. These photons remain in the core until absorption due to total internal reflection. The main advantage of clad pumping is that it allows divergent fiber pump sources such as a high power lower brightness diode array that require a much larger numerical aperture to be efficiently injected into the fiber. This allows the pump launch efficiency to be very high and alignment tolerances to become much less stringent [9]. In order to provide suitable absorption of the clad pump, the fiber lengths need to be longer than those required for a core pumped system.

A problem encountered when trying to scale an YDFA to large power and maintain single frequency operation is that the signal wave generates a Brillouin gain, causing a

backward traveling Stokes wave. With high pump power, the Brillouin wave can build up substantial power in the fiber and can extract gain, which limits the amplifier gain. The process is called Stimulated Brillouin Scattering (SBS) and is shown schematically in 2.4. In the figure, an incident laser beam of ω_L scattering from the refractive index variation associated with a sound wave of frequency Ω . Since the acoustic wave fronts are moving away from the incident laser wave, the scattered light is shifted downward in frequency to the Stokes frequency. This interaction can lead to stimulated light scattering because the

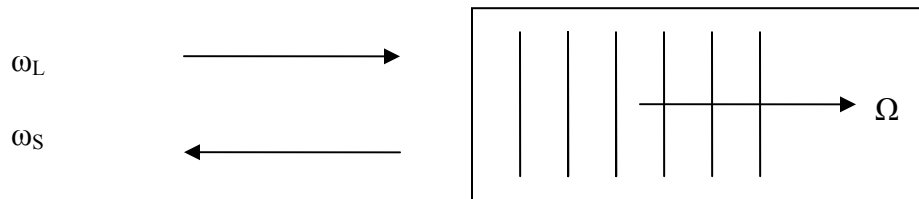


Figure 2.4. Stimulated Brillouin Scattering [10].

interference of the Stokes fields and the laser contain a frequency component of a difference frequency. The low frequency acoustic waves essentially create a grating in the media, causing a reflection. SBS has been used for phase conjugation and pulse compression but presents problems due to its limiting of fiber optic intensities [11]. Methods to mitigate SBS include thermal gradients along the fiber, which causes the reverse Stokes waves to set up at different frequencies based on the temperatures and thus do not have gain through the fiber, and larger core diameters, which reduce the intensity of the signal and hence reduce the buildup of the SBS.

Section 2.2: Phase Noise due to Amplified Spontaneous Emission

A fundamental cause of phase noise in an optical amplifier is Amplified Spontaneous Emission (ASE). The derivation for the phase noise and linewidth broadening due to ASE is given as follows [8]: An ideal amplifier can be viewed as a device that takes an input field

E_{in} and amplifies it by a factor \sqrt{G} where G is the power gain of the amplifier. In an ideal amplifier that is free from spontaneous emission, the output signal E_{out} is given by

$E_{out} = \sqrt{G}E_{in} e^{-ink_o L}$ where L is the amplifier length, n the index of refraction and k_o the

signal wave vector in a vacuum. The mean ASE power at the amplifier output, P_{ASE} , in an optical bandwidth B_o is given by:

$$P_{ASE} = n_{sp} h\nu B_o (G - 1) \quad (3)$$

where n_{sp} is the spontaneous emission factor [8]

$$n_{sp} \equiv \frac{\eta N_2}{\eta N_2 - N_1} \quad (4)$$

where N_1 and N_2 are the atomic population densities of laser system levels 1 and 2,

respectively, and $\eta = \frac{\sigma_e}{\sigma_a}$ where σ_e and σ_a are the emission and absorption cross sections,

respectively. The ASE photon rate, Ψ , at the output is given by $\Psi = \frac{P_{ASE}}{h\nu}$. The mean of the

arrival time of photons during the ASE event time, t_{ASE} , is given by the reciprocal of the

photon rate, that is, $t_{ASE} = \frac{1}{\Psi} = \frac{h\nu}{P_{ASE}}$, which from equation (3) is

$$t_{ASE} = \frac{1}{n_{sp} B_o (G - 1)} \quad (5)$$

Assume an ASE event occurs in the optical amplifier during a time t_{ASE} resulting in noise to both the amplitude and the phase of the output signal. Amplitude noise results from the coherent combination of the portion of the ASE field that is in phase with the signal, while phase noise results from the out of phase component of the ASE field with the signal field. This can be diagrammed as shown in Figure 2.5 [12, 13, 14].

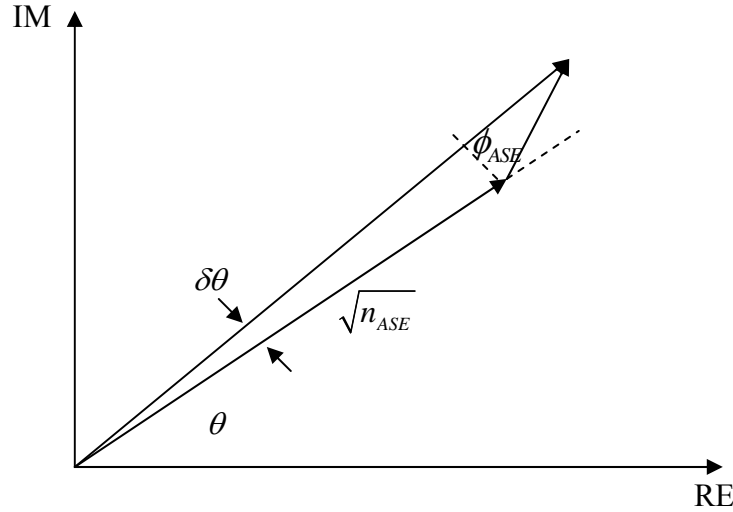


Figure 2.5. Phasor diagram showing phase deviation $\delta\theta$ associated with the emission of a single photon with random phase angle ϕ_{ASE} , when the mean signal photon number is n_{ASE} corresponding to a signal field of $\sqrt{n_{ASE}}$.

The figure shows the phasor diagram for a single ASE event, that is, the emission of a single spontaneous photon with a random phase angle ϕ_{ASE} ($-\pi < \phi_{ASE} < \pi$). The undeviated phase of the laser is θ . The phase noise in the laser due to this single event, $\delta\theta$, caused by the ASE event, ϕ_{ASE} , can be seen from the figure as

$$\tan(\delta\theta) \approx \delta\theta = \frac{1}{\sqrt{n_{ASE}}} \cos(\phi_{ASE}) \quad (6)$$

where n_{ASE} is the number of signal photons generated by the event. Averaging over a large

number of random events $\overline{\cos(\phi_{ASE})} = \frac{1}{\sqrt{2}}$, the average phase deviation, $\Delta\theta_{ASE}$, due to a

large number of events is

$$\Delta\theta_{ASE} = \frac{1}{\sqrt{2n_{ASE}}} \quad (7)$$

where $\Delta\theta_{ASE}$ is the time averaged deviation to the phase θ due to ASE phase noise. The

amplified signal power is GP_s^{in} and the average number of signal photons, $\langle n_s \rangle$, during t_{ASE}

is given by:

$$\langle n_s \rangle = \frac{GP_s^{in}}{h\nu} t_{ASE} = \frac{GP_s^{in}}{h\nu} \frac{1}{n_{sp} B_o (G-1)} \quad (8)$$

Combining equations (7) and (8) gives

$$\Delta\theta_{ASE} = \sqrt{\frac{h\nu B_o (G-1)}{\eta_d 2GP_s^{in}}}. \quad (9)$$

To derive the equation for linewidth broadening due to phase noise, consider the effect of N spontaneous emission events on the phase of the signal during a time T. Since the ASE events are random and can have any value between $-\pi$ and π with equal probability, the net change in the phase of the signal can be written as

$$\langle [\Delta\theta(N)]^2 \rangle = \langle (\delta\theta)^2 \rangle N \quad (10)$$

The number of spontaneous transitions into a single mode in a time T is given by [14] as

$$N(T) = \frac{\mu T}{t_c} \quad (11)$$

where μ is the laser inversion factor and t_c is the photon lifetime. Combining equations (10)

and (11) yeilds

$$\Delta\theta(t) = \langle (\delta\theta(t))^2 \rangle^{\frac{1}{2}} = \sqrt{\frac{1}{2n_{ASE}} \frac{\mu T}{t_c}} \quad (12)$$

$$(13)$$

Cowle [13] derives the spectral density function of an amplifier to be

$$S(\omega) = \frac{\langle E^2 \rangle}{4\pi} \frac{\frac{1}{4n_{ASE} t_c}}{\left(\frac{\mu}{4n_{ASE} t_c} \right)^2 + (\omega - \omega_0)^2} \quad (14)$$

Equation (14) shows that the Lorentzian linewidth with the FWHM is given by

$$\Delta\omega = \frac{\mu}{2n_{ASE} t_c} \quad (15)$$

Combining equations (12) and (15), it is shown that the phase variance, $\Delta\theta$, corresponding to a time T of a signal source having a Lorentzian spectrum of FWHM $\Delta\nu$ is and having Guassian phase noise, is given as

$$\Delta\theta^2(T) = \Delta\omega T = 2\pi\Delta\nu T \quad (16)$$

Let $\Delta\phi_s$ be the input signal phase deviation and $\Delta\nu_s$ be the input signal linewidth. Then

from equation (16)

$$\Delta\phi_s^2(t_{ASE}) = 2\pi\Delta\nu_s t_{ASE} \quad (17)$$

Combining equations (5) and (17)

$$2\pi\Delta\nu_s t_{ASE} = \frac{2\pi\Delta\nu_s}{n_{sp} B_o (G - 1)} \quad (18)$$

From the model developed by Cowle [13], the amount of spectral broadening $\delta\nu$ due to the amplifier relative to the input signal $\Delta\nu_s$ can be approximated by the ratio $\Delta\theta_{ASE} / \Delta\phi_s$.

Combining equations (9) and (18) yields

$$\frac{\delta\nu}{\Delta\nu_s} \approx \frac{\Delta\phi}{\Delta\theta} = \sqrt{\frac{n_{sp}^2 h\nu B_o^2 (G - 1)^2}{4\pi G \Delta\nu_s P_s^{in}}} \quad (19)$$

resulting in the expression for the linewidth broadening due to ASE phase noise

$$\delta\nu \approx \sqrt{\frac{n_{sp}^2 h\nu B_o^2 \Delta\nu_s (G - 1)^2}{4\pi G P_s^{in}}} \quad (20)$$

Phase noise due to ASE, Equation (9) and line width broadening due to phase noise are the equations as derived by Desurvire [8] and are referenced in several research papers as discussed in the next section.

Section 2.3: Previous Phase Noise Experiments

Linewidth broadening due to phase noise has been measured in a number of experiments. In work referenced by Desurvire [8], fair agreement between equation (20) and experimental data was realized. In research by Moller [15], however, typical values for an erbium doped fiber laser were used in equation (20), which resulted in a calculated theoretical value of $\delta\nu$ to be 4.2 kHz, yet in the experiment that was conducted in the research, the value was found to be smaller than 10 Hz. Other research has shown that the amplified linewidth was approximately the same as the seed linewidth [16, 17, 18], and any increase due to ASE is negligible or not large enough to be measured by the experiment. Much more study of the derivation of this equation and the specific configurations of these other experiments is required to fully understand the shortcomings of this derivation and the situations in which it applies.

Although these previous experiments measured the linewidth broadening due to amplified phase noise, only a few instances of prior research measure the temporal and spectral content of phase noise. One example of this research by Augst [6] measured the detailed temporal and spectral content of the phase noise of a commercial IPG ytterbium fiber laser amplifier operating at 1 and 10 watts. It was found that steady state phase noise was not achieved for eight minutes after turn on of the amplifier, indicating that the heating of the fiber continued long after steady state power was achieved. The maximum phase drift was found to be immediately after the turn on of the amplifier and was reported at 20 waves/sec. This rapid phase drift immediately after turning the amplifier on is attributed to a rapid temperature rise of the fused silica fiber, resulting in a change of the index of refraction. The total drift of phase was reported as 2000 waves, which corresponds to a

temperature increase of the fiber of 10 degrees C. Thermal expansion also contributed to the phase drift with a reported value of 2 waves/sec. In this paper $\lambda / 10$ was considered an approximate threshold to maintain phase noise. This value was exceeded on the order of milliseconds

$$T_{phase_noise} = 5m\ sec \quad (21)$$

where T_{phase_noise} is the period of the phase noise. This indicates a control bandwidth of several to tens of kilohertz would be required to control the phase noise within an acceptable level for coherent beam combination. The authors attributed this rapid phase noise to temperature variations, mechanical resonances, acoustic noise and cooling fans.

In the work by Jones [7], a laboratory 200 watt ytterbium fiber amplifier was used to measure the phase noise. This research contrasts that of Augst by utilizing a laboratory amplifier on an open optical table rather than a packaged commercial laser and at a much higher operating power. In this configuration, cooling was by passive air convection and by conduction into a supporting drum; thus, there was no possibility of induced rapid phase fluctuation due to cooling fans or air buffeting. In this work, after the pump reached full power, the phase drift was found to be dependant on the power of the amplifier and an empirical equation of the phase drift was found to be

$$\phi(t) = 2\pi\alpha P_{out} t + \phi_n(t) \quad (22)$$

where P_{out} is the output power of the amplifier, t is time and α is a constant that was found to be 0.17 waves/watt-sec. $\phi_n(t)$ is the amplifier phase noise, a random fluctuation. The power dependant drift term was attributed to heating of the optical components in thermal contact with the fiber. In this research $\lambda / 20$ was used as a threshold for acceptable phase

deviation for coherent combining. The paper showed that a closed loop bandwidth of multi kilohertz would be needed to control the initial rapid phase change, but a much lower bandwidth of 50 Hz would be sufficient in steady state since the phase deviations are well below the threshold required for coherent combination. The phase changes reduced significantly after the initial startup, which was attributed to variations in pump power due to changes in the current to the pump diodes.

In another publication of the work by Jones et. al. [19], three distinct features of the phase drift were described: an abrupt change in the phase initially after turn on of the pump is attributed to the change in refractive index due to the population inversion induced by the pump beam; a slower power proportional change is attributed to the heating of the fiber core, cladding and coating; and finally a linear increase in output phase with time, indicating the presence of a slower thermal effect, is attributed to heating of the fiber spool. The larger time constant is required to account for the thermal mass of the spool in comparison to that of the fiber. A deterministic phase change equation was generated as follows

$$\frac{\Delta\phi(t)}{2\pi} \approx k_1 \left(1 - e^{-\frac{t}{\tau_p}} \right) + k_2 P \left(1 - e^{-\frac{t}{\tau_f}} \right) + k_3 Pt \quad (23)$$

where $\Delta\phi(t)$ with respect to time, P is power in watts, $k_1 = 17$ waves, $k_2 = 8.0$ waves/W and $k_3 = 0.17$ waves/(sec • W) are constants, τ_p is the rise time of the pump power which was between 100 msec and 30 sec depending on output power, and τ_f is the thermal time constant of the fiber equal to 4 sec in this experiment. In addition to these drifts, phase noise is reported at a low magnitude but is sufficient to require correction to attain a $\lambda / 20$ control of the amplifier. In this case the authors report a 200 Hz bandwidth requirement to control the phase to this level of fidelity. The contrast of the two experiments discussed above is

significant. Although much more output power was obtained in the research by Jones et. al., a pristine laboratory environment was able to keep the phase noise to a remarkably low level requiring only less than 1 kHz bandwidth of control in steady state. The work by Augst, however, utilizing a commercial device not designed for low phase noise and with cooling fans and other mechanical disturbances, was shown to have a much higher degree of phase noise at steady state requiring tens of kHz bandwidth of correction. It is clear from this research and from the prior sections that mechanical disturbances may be the leading cause of phase noise.

Section 2.4 Theory of LOCSET

As previously discussed, the accurate control of the phase of parallel fiber amplifiers is required to coherently combine the beams. LOCSET is a very effective method to achieve this control. The architecture required for the LOCSET method uses a common master oscillator that is split to serve as a single seed beam for multiple fiber amplifier elements as shown in Figure 2.6. Two similar techniques are used by LOCSET: the self referencing and self synchronous methods. In each method the fiber elements are modulated at unique RF frequencies. In the self referencing LOCSET, one element is not modulated, and the technique causes the phase of the remaining elements to lock to the phase of the unmodulated element. In the self synchronous LOCSET, all elements are modulated, and the technique causes the phase of the elements to lock to the mean phase of all the elements. Here we will consider only the theory of self synchronous LOCSET [20].

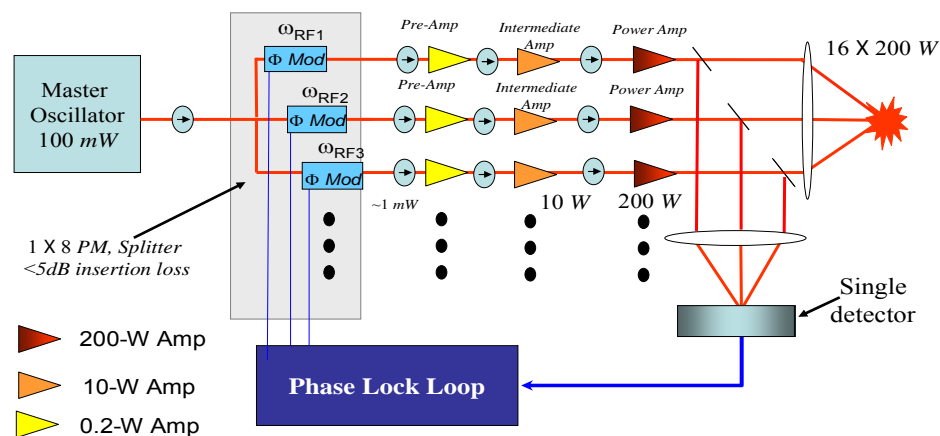


Figure 2.6. Coherent beam combining method using active phasing (LOCSET) [5].

The master oscillator is split into multiple signals for each amplifier in the array. Before seeding the amplifiers, the phase of each signal for each element is adjusted by a phase modulator. As described, this adjustment minimizes the phase error for that element and, in the case of self synchronous LOCSET, corrects the phase to an average phase for all elements. The adjustment is provided by an error control signal to the phase modulator from the phase control electronics shown in the diagram as the phase lock loop. At this point, the individual signals for each element are modulated at unique RF frequencies, which provide a unique identifier to the phase control electronics of each element's phase information. The master oscillator signals seed the fiber laser amplifiers, and a sample of each amplifier's output is combined onto a single photo detector. The signal from this photodetector contains the phase information of each element along with that element's unique modulation frequency. As will be described, the phase control electronics demodulate the phase of each individual element and appropriately and individually provide the error correction signal to the phase modulators. Thus, the time dependant phase disturbances and differences from the amplification process within each fiber laser amplifier element are corrected and the output beams of each amplifier are in phase. The current from the photodetector is

$$i_{PD}(t) = R_{PD} A \sqrt{\frac{\epsilon_o}{\mu_o}} E_{in}^2 \quad (24)$$

where R_{PD} is the responsivity of the photodetector and A is the area of the photodetector; μ_o and ϵ_o are the magnetic and electric permeabilities of free space, respectively; and E_{in} is the total electric field incident on the detector.

Assume there are N elements that are plane waves having identical polarization and each element's phase is modulated at unique frequencies ω_i where $i = 1 \dots N$. The electric field for the i th element, E_i , is given by:

$$E_i = E_{io} \cos(\omega_L t + \phi_i + \beta \sin(\omega_i t)) \quad (25)$$

where E_{io} is the magnitude of the i th electric field, ϕ_i is the optical phase of the i th element, β_i is the magnitude of the phase modulation of the i th element and ω_L is the frequency of the master oscillator laser. Substituting the trigonometric equation for the cosine of the sum of two angles equation (25) becomes

$$E_i(t) = E_{io} \cdot [\cos(\omega_L t + \phi_i) \cos(\beta_i \sin \omega_i t) - \sin(\omega_L t + \phi_i) \sin(\beta_i \sin(\omega_i t))] \quad (26)$$

The total electric field incident on the detector is the sum of all the electric fields that are incident on the detector; thus,

$$E_{in} = \sum_{i=1}^N E_{io} [\cos(\omega_L t + \phi_i) \cos(\beta_i \sin \omega_i t) - \sin(\omega_L t + \phi_i) \sin(\beta_i \sin(\omega_i t))] \quad (27)$$

Combining equations (24) and (27) an expression for the photo current is

$$i_{PD}(t) = R_{PD} A \sqrt{\frac{\epsilon_o}{\mu_o}} \left\{ \sum_{i=1}^N E_{io} (\cos(\omega_L t + \phi_i) \cos(\beta_i \sin(\omega_i t)) - \sin(\omega_L t + \phi_i) \sin(\beta_i \sin(\omega_i t))) \right\}^2 \quad (28)$$

or,

$$i_{PD}(t) = R_{PD} A \sqrt{\frac{\epsilon_o}{\mu_o}} \left(\sum_{i=1}^N E_{i_o} \left(\text{Cos}(\omega_L t + \phi_i) \text{Cos}(\beta_i \text{Sin}(\omega_i t)) - \text{Sin}(\omega_L t + \phi_i) \text{Sin}(\beta_i \text{Sin}(\omega_i t)) \right) \bullet \right. \\ \left. \sum_{j=1}^N E_{j_o} \left(\text{Cos}(\omega_L t + \phi_j) \text{Cos}(\beta_j \text{Sin}(\omega_j t)) - \text{Sin}(\omega_L t + \phi_j) \text{Sin}(\beta_j \text{Sin}(\omega_j t)) \right) \right) \quad (29)$$

or, using the distributive property of multiplication, equation (29) can be written as

$$i_{PD}(t) = R_{PD} A \sqrt{\frac{\epsilon_o}{\mu_o}} \sum_{i=1}^N \sum_{j=1}^N E_{i_o} E_{j_o} \left[\begin{array}{l} \text{Cos}(\omega_L t + \phi_i) \text{Cos}(\beta_i \text{Sin}(\omega_i t)) \text{Cos}(\omega_L t + \phi_j) \text{Cos}(\beta_j \text{Sin}(\omega_j t)) - \\ \text{Sin}(\omega_L t + \phi_i) \text{Sin}(\beta_i \text{Sin}(\omega_i t)) \text{Cos}(\omega_L t + \phi_j) \text{Cos}(\beta_j \text{Sin}(\omega_j t)) - \\ \text{Cos}(\omega_L t + \phi_i) \text{Cos}(\beta_i \text{Sin}(\omega_i t)) \text{Sin}(\omega_L t + \phi_j) \text{Sin}(\beta_j \text{Sin}(\omega_j t)) + \\ \text{Sin}(\omega_L t + \phi_i) \text{Sin}(\beta_i \text{Sin}(\omega_i t)) \text{Sin}(\omega_L t + \phi_j) \text{Sin}(\beta_j \text{Sin}(\omega_j t)) \end{array} \right] \quad (30)$$

Rearranging, equation (30) is written as

$$i_{PD}(t) = R_{PD} A \sqrt{\frac{\epsilon_o}{\mu_o}} \sum_{i=1}^N \sum_{j=1}^N E_{i_o} E_{j_o} \left[\begin{array}{l} \text{Cos}(\omega_L t + \phi_i) \text{Cos}(\omega_L t + \phi_j) \text{Cos}(\beta_i \text{Sin}(\omega_i t)) \text{Cos}(\beta_j \text{Sin}(\omega_j t)) - \\ \text{Sin}(\omega_L t + \phi_i) \text{Cos}(\omega_L t + \phi_j) \text{Sin}(\beta_i \text{Sin}(\omega_i t)) \text{Cos}(\beta_j \text{Sin}(\omega_j t)) - \\ \text{Cos}(\omega_L t + \phi_i) \text{Sin}(\omega_L t + \phi_j) \text{Cos}(\beta_i \text{Sin}(\omega_i t)) \text{Sin}(\beta_j \text{Sin}(\omega_j t)) + \\ \text{Sin}(\omega_L t + \phi_i) \text{Sin}(\omega_L t + \phi_j) \text{Sin}(\beta_i \text{Sin}(\omega_i t)) \text{Sin}(\beta_j \text{Sin}(\omega_j t)) \end{array} \right] \quad (31)$$

Using the trigonometric identities,

$$\sin \alpha \sin \beta = \frac{1}{2} \cos(\alpha - \beta) - \frac{1}{2} \cos(\alpha + \beta)$$

$$\sin \alpha \cos \beta = \frac{1}{2} \sin(\alpha + \beta) + \frac{1}{2} \sin(\alpha - \beta)$$

$$\cos \alpha \cos \beta = \frac{1}{2} \cos(\alpha - \beta) + \frac{1}{2} \cos(\alpha + \beta)$$

$$\cos \alpha \sin \beta = \frac{1}{2} \sin(\alpha + \beta) - \frac{1}{2} \sin(\alpha - \beta),$$

and, using the Fourier series expansion for $Cos(\beta_i Sin(\omega_i t))$ and $Sin(Sin\beta_j(\omega_j t))$, [21]

$$\cos(x \sin \theta) = J_0(x) + 2 \sum_{n=1}^{\infty} J_{2n}(x) \cos(2n\theta)$$

$$\sin(x \sin \theta) = 2 \sum_{n=1}^{\infty} J_{2n-1}(x) \sin((2n-1)\theta),$$

where J_n represents the Bessel function of the first kind of order n . Equation (31) becomes

$$i_{pd}(t) = R_{pd} \frac{A}{2} \sqrt{\frac{\epsilon_0}{\mu_0}} \sum_{i=1}^N E_{i0} \left\{ \sum_{j=1}^N E_{j0} \left[\begin{aligned} & \left(\cos(\phi_i - \phi_j) - \cos(2\omega_L t + \phi_i + \phi_j) \right) \bullet \\ & \left(J_0(\beta_i) + 2 \sum_{n_i=1}^{\infty} J_{2n_i}(\beta_i) \cos(2n_i \omega_i t) \right) \bullet \\ & \left(J_0(\beta_j) + 2 \sum_{n_j=1}^{\infty} J_{2n_j}(\beta_j) \cos(2n_j \omega_j t) \right) - \\ & \left(\sin(2\omega_L t + \phi_i + \phi_j) + \sin(\phi_i - \phi_j) \right) \bullet \\ & \left(2 \sum_{n_i=1}^{\infty} J_{2n_i-1}(\beta_i) \sin((2n_i-1)\omega_i t) \right) \bullet \\ & \left(J_0(\beta_j) + 2 \sum_{n_j=1}^{\infty} J_{2n_j}(\beta_j) \cos(2n_j \omega_j t) \right) - \\ & \left(\sin(2\omega_L t + \phi_i + \phi_j) + \sin(\phi_i - \phi_j) \right) \bullet \\ & \left(J_0(\beta_i) + 2 \sum_{n_i=1}^{\infty} J_{2n_i}(\beta_i) \cos(2n_i \omega_i t) \right) \bullet \\ & \left(2 \sum_{n_j=1}^{\infty} J_{2n_j-1}(\beta_j) \sin((2n_j-1)\omega_j t) \right) + \\ & \left(\cos(\phi_i - \phi_j) - \cos(2\omega_L t + \phi_i + \phi_j) \right) \bullet \\ & \left(2 \sum_{n_i=1}^{\infty} J_{2n_i-1}(\beta_i) \sin((2n_i-1)\omega_i t) \right) \bullet \\ & \left(2 \sum_{n_j=1}^{\infty} J_{2n_j-1}(\beta_j) \sin((2n_j-1)\omega_j t) \right) \end{aligned} \right] \quad (32)$$

The terms oscillating at optical frequency of $2\omega_L t$ can be neglected, since these are well

beyond the bandwidth of the optical detector. Since $P_i = E_i^2 A \sqrt{\frac{\epsilon_o}{\mu_o}}$, where P_i is the power

into the detector from the i th element, the term $A \sqrt{\frac{\epsilon_o}{\mu_o}} \sum_{i=1}^N E_{io} \sum_{j=1}^N E_{jo}$ can be written

as $\sum_{i=1}^N \sqrt{P_i} \sum_{j=1}^N \sqrt{P_j}$. Equation (32) then becomes

$$i_{PD}(t) = \frac{R_{PD}}{2} \sum_{i=1}^N \sqrt{P_i} \sum_{j=1}^N \sqrt{P_j} \left(\begin{array}{l} \text{Cos}(\phi_i - \phi_j) (J_o(\beta_i) + 2 \sum_{n_i=1}^{\infty} J_{2n_i}(\beta_i) \cos(2n_i \omega_i t)) \bullet \\ (J_o(\beta_j) + 2 \sum_{n_j=1}^{\infty} J_{2n_j}(\beta_j) \cos(2n_j \omega_j t)) - \\ \text{Sin}(\phi_i - \phi_j) (2 \sum_{n_i=1}^{\infty} J_{2n_i-1}(\beta_i) \sin((2n_i - 1)\omega_i t)) \bullet \\ (J_o(\beta_j) + 2 \sum_{n_j=1}^{\infty} J_{2n_j}(\beta_j) \cos(2n_j \omega_j t)) - \\ \text{Sin}(\phi_i - \phi_j) (J_o(\beta_i) + 2 \sum_{n_i=1}^{\infty} J_{2n_i}(\beta_i) \cos(2n_i \omega_i t)) \bullet \\ (2 \sum_{n_j=1}^{\infty} J_{2n_j-1}(\beta_j) \sin((2n_j - 1)\omega_j)) + \\ (\text{Cos}(\phi_i - \phi_j) (2 \sum_{n_i=1}^{\infty} J_{2n_i-1}(\beta_i) \sin((2n_i - 1)\omega_i t)) \bullet \\ (2 \sum_{n_j=1}^{\infty} J_{2n_j-1}(\beta_j) \sin((2n_j - 1)\omega_j)) \end{array} \right) \quad (33)$$

This term shows the beating of the phase modulated elements against each other. The photo current is demodulated in the phase control electronics to generate the error signal term.

Demodulation in the RF domain will be used to generate the error signal for each optical amplifier element. Figure 2.7 shows a typical block diagram of the signal processing electronics of a two element array system. Each of the element's electronics is identical

except for the different phase modulation/demodulation frequencies. The photo current is split into N separate elements, and each element is multiplied by $\sin(\omega_i t)$, where ω_i corresponds to the initial modulation frequencies for the i th element. Each of these signals is then integrated over a time τ in the signal processing electronics. τ is selected to

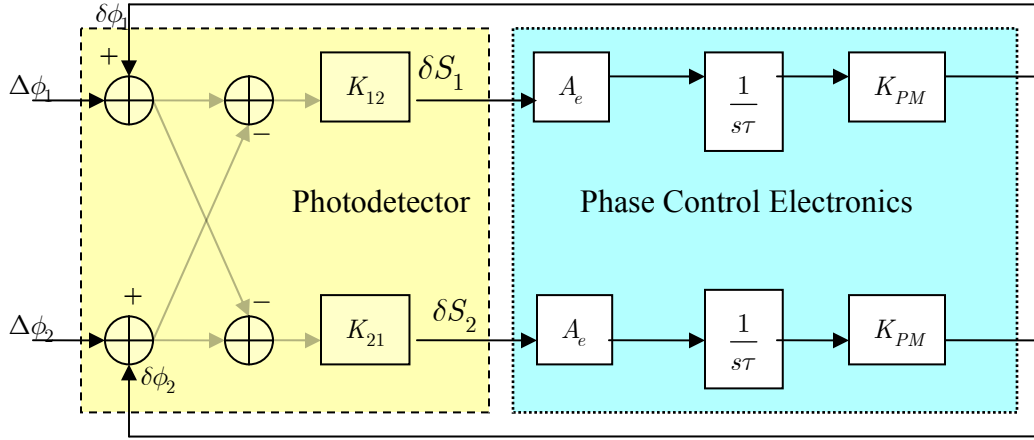


Figure 2.7 Self Synchronous LOCSET control block diagram for two elements.

be large enough to isolate the individual phase control signals of the phase modulated elements and small enough to provide adequate bandwidth to cancel the phase disturbances from the fiber amplifiers as discussed in the previous section. That is $\tau \gg 2\pi / |(\omega_i - \omega_j)|$ for all i and j when $i \neq j$, and $\tau \ll T_{Phase_Noise}$ where T_{Phase_Noise} is the period of the phase excursion that needs to be controlled for efficient coherent combination. The phase control error signal for an arbitrary i th element self synchronous LOCSET is then

$$S_{SSi} = \frac{1}{\tau} \int_0^{\tau} i_{PD}(t) \sin(\omega_i t) dt \quad (34)$$

which, to a very good approximation is

$$S_{SSi} = R_{PD} \sqrt{P_i} J_1(\beta_i) \left(\sum_{j=1}^N \sqrt{P_j} J_o(\beta_j) \text{Sin}(\phi_{j_o} - \phi_{i_o}) \right) \quad (35)$$

The details of this step in the derivation are quite tedious and are provided in Appendix 1.

From equation (35) the closed loop performance of the self synchronous LOCSET can be analyzed. The phases for the i th array element are,

$$\phi_i(t) = \phi_{i_o} + \Delta\phi_i(t) \quad (36)$$

where ϕ_{i_o} represents the mean phase of the i th element and $\Delta\phi_i(t)$ represents the time varying component of the i th element when the control loop is open. Substituting equation (36) into (35),

$$S_{SSi} = R_{PD} \sqrt{P_i} J_1(\beta_i) \left(\sum_{j=1}^N \sqrt{P_j} J_o(\beta_j) \text{Sin}(\phi_{j_o} - \phi_{i_o} + \delta\phi_j(t) - \Delta\phi_i(t)) \right) \quad (37)$$

where $\delta\phi_j(t)$ represent the closed loop phase control error for the j th element. It is assumed that the set point for the mean phase is adjusted to be equal such that $\phi_{i_o} = \phi_{j_o}$ and that the control loop gain is high so that the phase disturbances are small such that $\text{sin}(\delta\phi_j(t) - \Delta\phi_i(t)) \approx \delta\phi_j(t) - \Delta\phi_i(t)$ then,

$$S_{SSi} = R_{PD} \sqrt{P_i} J_1(\beta_i) \sum_{j=1}^N \sqrt{P_j} J_o(\beta_j) (\delta\phi_j(t) - \Delta\phi_i(t)) \quad (38)$$

Figure 2.7 is a simplified linear systems model block diagram for the self synchronous LOCSET control loop for two elements. The dashed region is the photodetector, which shows the summation of the open loop and closed loop phase signals.

K_{12} and K_{21} are the terms multiplying the phase control signals within the photodetector as derived above. In general from Appendix 1,

$$K_{ij} = R_{PD} \sqrt{P_i} J_1(\beta_i) \sqrt{P_j} J_0(\beta_j) \quad (39)$$

The dotted region is the phase control electronics, which show the integration of the signal in the Laplace domain $\frac{1}{sT}$, where s represents the Laplace variable $j\omega$, the RF amplification of the error signal A_e and the phase modulator's voltage to phase conversion factor K_{PM} . In the control loop, the phase of the element is subtracted from the closed loop phase of the second element. This gives insight into the more general linear control loop for a generic i th element. Figure 2.8 is the general linear systems model block diagram for the self

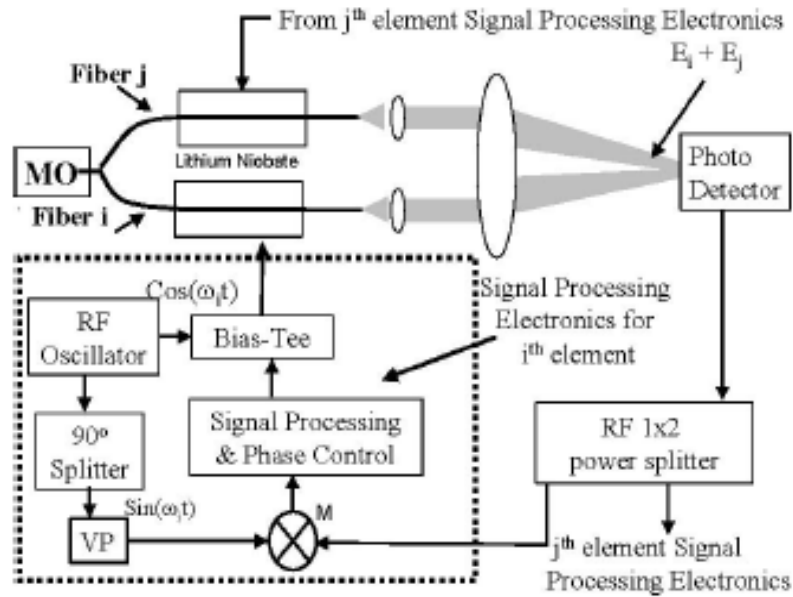


Figure 2.8 Self Synchronous LOCSET control loop block diagram for the i th element [22].

synchronous LOCSET control loop for the i th element. In this figure, the functions of the phase control electronics have been combined. In the control loop, the open loop phase of

the i th element is subtracted from the mean closed loop phase of the remaining elements. This function is performed in the optical photodetector, and the electronic signal processing and phase modulators functions are represented in the block on the far right of Figure 2.8. From the linearized block diagram shown in Figure 2.9, the closed loop phase error for the

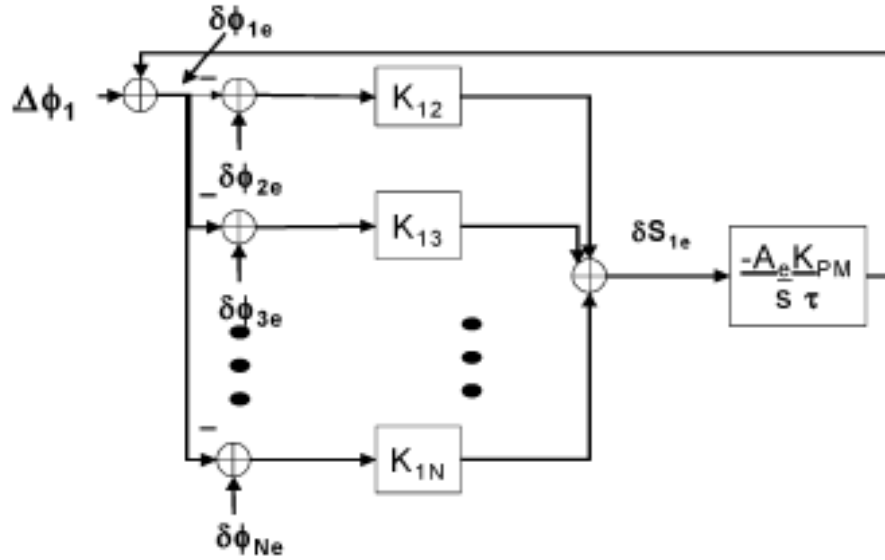


Figure 2.9 Linear control loop model for self-synchronous LOCSET [20].

i th element, $\delta\phi_i$, due to the external phase error in the i th element, $\Delta\phi_i$, and the closed loop phase error of the remaining elements can be derived. Analyzing the model, an expression for $\delta\phi_i$ is

$$\delta\phi_i(s) = \Delta\phi_i + \frac{A_e K_{PM}}{s\tau} \sum_{\substack{j=1 \\ j \neq i}}^N K_{ij} (\delta\phi_j(s) - \delta\phi_i(s)) \quad (40)$$

where s represent the Laplace variable $j\omega$, A_e represents the RF amplifier gain, K_{PM} represents the phase modulator's voltage to phase conversion factor and τ represents the

integrator time constant. The first term in summation $\sum_{\substack{j=1 \\ j \neq i}}^N K_{ij} \delta\phi_j(s)$ is the sum of

uncorrelated phase control error signals or zero mean random numbers. Consequently, with large N, that sum will approach zero. Equation (40) can then be written as

$$\delta\phi_i(s) = \frac{\Delta\phi_i}{1 + \frac{A_e K_{PM}}{s\tau} \sum_{\substack{j=1 \\ j \neq i}}^N K_{ij}} \quad (41)$$

or

$$\delta\phi_i(s) = \frac{s\Delta\phi_i}{s + \frac{A_e K_{PM}}{\tau} \sum_{\substack{j=1 \\ j \neq i}}^N K_{ij}}. \quad (42)$$

For the i th element the signal exiting the photodetector is

$$\delta\phi_i(s) R_{PD} \sqrt{P_i} J_1(\beta_i) \sum_{j=1}^N \sqrt{P_j} J_o(\beta_j) \quad (43)$$

Equation (42) shows the closed loop electronic bandwidth of the system as

$$BW = \frac{A_e K_{PM}}{\tau} \sum_{\substack{j=1 \\ j \neq i}}^N K_{ij} \quad (44)$$

Assuming that the noise in the photodetector is dominated by shot noise, the signal to noise ratio for the i th element will be

$$SNR_i = \frac{\left(\delta\phi_{i_rms} R_{PD} \sqrt{P_i} J_1(\beta_i) \sum_{j=1}^N \sqrt{P_j} J_o(\beta_j) \right)^2}{2qBR_{PD} \sum_{j=1}^N P_j} \quad (45)$$

where $\delta\phi_{ie_rms}$ is the root-mean-squared phase error in closed loop operation, q is the charge of an electron and B is the electronic bandwidth of the system. Substituting equation (44) into (45) results in

$$SNR_i = \frac{\left(\delta\phi_{ie_rms} R_{PD} J_1(\beta_i) \sqrt{P_i} \sum_{\substack{j=1 \\ j \neq i}}^N J_o(\beta_j) \sqrt{P_j} \right)^2}{2q \frac{A_e K_{PM}}{\tau} \sum_{\substack{j=1 \\ j \neq i}}^N K_{ij} R_{PD} \sum_{j=1}^N \sqrt{P_j}} \quad (46)$$

If β_j is small so that $J_o(\beta_j) \approx 1$, the powers of the elements are equal so that the coupling elements, K_{ij} , are equal and N is much larger than 1, then the signal to noise ratio can be shown more clearly, and equation (46) becomes

$$SNR_i = \frac{\delta\phi_{ie_rms}^2 R_{PD} J_1(\beta_i)^2 P_i \pi \tau}{q A_e K_{PM} K_{ij}} \quad (47)$$

This result clearly shows that the signal to noise ratio is independent of the number of elements and that the self synchronous LOCSET will remain stable as the number of elements increases.

Section 2.5 LOCSET Two-Element Analysis

In the control analysis of LOCSET, a fundamental assumption was that the open loop fluctuations $\Delta\phi_j$ are unrelated to the open fluctuations $\Delta\phi_i$. In this section, a two element control analysis of LOCSET is developed to better understand that assumption. The control circuit for the two elements is simple enough that the equations for $\delta\phi_i$, $i = 1, 2$, as a function of both $\Delta\phi_j$, $j = 1, 2$, can be developed and are analyzed for a variety of input functions. The two element control circuit is shown in Figure 2.7. For further simplicity, assume $K_{12} = K_{21} = K_o$ and from the previous section, $K_o = R_{PD} \sqrt{P_1} J_1(\beta_1) \sqrt{P_2} J_0(\beta_2)$. Assuming $\beta_1 = \beta_2$ and $P_1 = P_2$, the control diagram is analyzed and the following equations are derived:

$$\delta\phi_1 = \frac{(BW + s)\Delta\phi_1 + BW\Delta\phi_2}{2BW + s} \quad (48)$$

and

$$\delta\phi_2 = \frac{BW\Delta\phi_1 + (BW + s)\Delta\phi_2}{2BW + s} \quad (49)$$

where $BW = \frac{A_e K_{PM} K_o}{\tau}$. As can be seen, for large BW, equations (48) and (49) are

approximately

$$\delta\phi_1 = \delta\phi_2 = \frac{\Delta\phi_1 + \Delta\phi_2}{2}. \quad (50)$$

which shows that LOCSET is equalizing the output phase of each element and setting it to the average of the inputs. When $\Delta\phi_1 = \Delta\phi_2$, a trivial case occurs resulting in

$\delta\phi_1 = \delta\phi_2 = \Delta\phi_1 = \Delta\phi_2$, which show that LOCSET is equalizing the output phases of each element.

What needs to be explored is smaller BW and the coupling of frequencies from the input of one element 2 to the output of the other element. To provide this understanding, equation (48) is programmed into Mathcad, and various functions for $\Delta\phi_1$ and $\Delta\phi_2$ are used to excite the control system, and the effect on $\delta\phi_1$, the output of element 1, is studied. The functions explored are cosine functions $b \cos(at)$, where a and b are varied, representing phase noise at a frequency a , and a step function, at constant phase noise at all times. Parameter space explored is high and low frequencies for the cosine inputs. The program for this analysis is provided in Appendix 3 and the results are presented and discussed in Section 5.5.

Section 2.6 Coherent Combination Efficiency

As mentioned in a previous section, the amount of phase deviation must be kept small to allow for efficient coherent combination and the ability of the LOCSET control system to perform, which is the subject of this research. The research discussed by Augst [6] suggested $\lambda / 10$ was an acceptable threshold under which acceptable combining performance could be achieved, while Jones [7] suggested $\lambda / 20$. There are two important contributions to phase deviation in the LOCSET system: the phase deviation due the LOCSET-imposed sinusoidal term to generate the error signal, β_i , and the residual phase deviations due to the noise in the control loop that LOCSET is unable to correct. The effect on combining efficiency of the former is discussed here, and data on the later is collected and discussed in later sections. The root-mean-squared phase deviation ϕ_{rms} due to the imposed sinusoidal phase modulation amplitude of β_i in a single array element is

$$\phi_{rms} = \frac{\beta_i}{\sqrt{2}}. \quad (51)$$

LOCSET is designed to provide the same phase modulation amplitude to each array element such that $\beta_i = \beta_j$ for all i and j . In research by Nabors [23], the effect of uncorrelated phase deviations on coherently combined arrays was studied. The effect on the far field Strehl ratio of a coherently combined array due to an uncorrelated phase deviation is given as

$$SR = e^{-\phi_{rms}^2} + \frac{1 - e^{-\phi_{rms}^2}}{N} \quad (52)$$

where N is the number of elements in the array and SR is the Strehl ratio, defined as the ratio of peak far-field intensity of a beam divided by the peak intensity from a uniformly illuminated aperture having the same total power. Figure 2.10 shows the resulting Strehl

ratio due to RMS phase deviations from 0 to 0.2 for a 16 element array. The amplitude of the phase modulation in LOCSET, β_i , typically used is 0.1, which yields $\phi_{rms} = 0.0707$, resulting in a Strehl ratio of 0.995. The value of $\lambda / 10$ is the same as β_i , while the value of $\lambda / 20$ results in $\phi_{rms} = 0.0354$, resulting in a Strehl ratio of 0.9988.

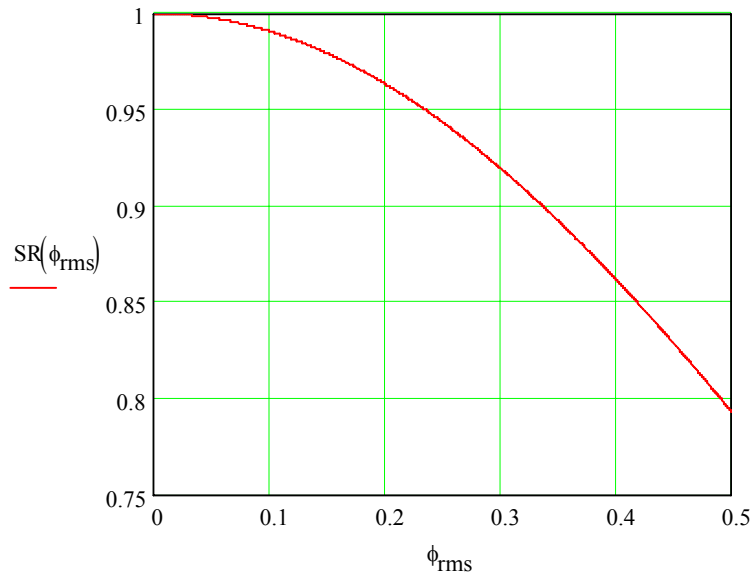


Figure 2.10. Strehl ratio plot of RMS phase deviation for 16 elements.

Equation (52) illustrates how the combination efficiency for this research will be measured; that is, the Strehl ratio as calculated in equation (52) will be the measurement to ascertain LOCSET's ability to control phase noise and provide beams that can be coherently combined. The RMS phase value and the resultant Strehl ratio will be calculated for the closed loop phase errors.

III. LOCSET Model

Using Mathcad version 11.0a, a model of the control diagram shown in Figure 2.9 of LOCSET was developed. The input of the model is the electronic constants $R_{PD}, A_e, K_{PM}, \tau$, the number of elements in the system N , the phase modulation magnitude for each element β_i where $i = 1, \dots, N$, the power of each element P_i , where $i = 1, \dots, N$, the number of data points M and the data points $(f_{ik}, \Delta\phi_{ik})$, where $i = 1, \dots, N, k = 1, \dots, M$, $\Delta\phi_{ik}$ represents the measured open loop phase noise for the i th element at frequency f_{ik} . The model was designed for $N \leq 16$ and no limit on M except those inherent in using range variables, vectors and matrices in Mathcad, which are approximately 15,000. The inputs into the model consisted of three Excel files, one containing the electronic constants, one containing the power data and one containing the phase noise data. An alternate configuration for smaller numbers of elements is separate files for each element's frequency and phase, which was used for two elements. The first file contains the electronic constants and is a $3 \times (6+N)$ Excel file, with the first column containing the name of the constant, the second column containing the value of the constant used by Mathcad, and the third column containing the units of the constant. The second file is a $N \times 2$ file, with the first column containing the element number and the second column containing the power in watts of that element. The third file is a $(2N) \times M$ file, with the odd columns holding the data $f_{2i-1,k}$ and the even columns holding the data $\Delta\phi_{2i,k}$, where $i = 1, \dots, N$. Alternatively, $N \times 2 \times M$ files each contain the data $f_{2i-1,k}$ in the odd columns and the even columns hold the data $\Delta\phi_{2i,k}$, where $i = 1, \dots, N$. The model executes equation (43) and (42) to obtain the closed loop phase noise of the LOCSET system

and outputs an Excel file that is an NxM matrix, containing the data $\delta\phi_{ik}$ with the same frequency $f_{i,k}$ as the input phase noise data. Data plots and other calculation can then be performed on the output data. The model first calculates a matrix containing the values of K_{ij} as per equation (39)

$$K_{ij} = R_{PD} \sqrt{P_i} J_1(\beta_i) \sqrt{P_j} J_0(\beta_j)$$

and then calculates $\sum_{\substack{j=1 \\ j \neq i}}^N K_{ij}$ for each i for use in the final calculation, which is equation (42)

$$\delta\phi_{ie}(s) = \frac{s\Delta\phi_i}{s + \frac{A_e K_{PM}}{\tau} \sum_{\substack{j=1 \\ j \neq i}}^N K_{ij}}$$

The power of the Mathcad range variable is used extensively in the model, which greatly simplifies the model and allows for easy execution of the calculations. The model also calculates the bandwidth for each element in both radians and hertz and computes the control loop gain as a function of frequency for each element. A generic Mathcad model

Variable Description	LOCSET Theory symbol	Mathcad variable identifier	Value	Units
Power Detector electronic circuit sensitivity	R_{PD}	Rpd	1883	V/W
RF amplifier gain	A_e	Ae	177.5	none
phase modulators voltage to phase conversion factor	K_{PM}	Kpm	1.26	rads/V
integrator time constant	τ	τ	0.16	microseconds
Amplitude of modulation	β_i	β_i	0.1	Fraction of period

Table 3.1. Electronic constants used in LOCSET model and experiments.

which was used to calculate the 16 element bandwidth and control loop gain discussed later and a model tailored to the data used in this research for a two element system were used in

this research and are shown in with representative plots in Appendix 3. The electronic constants that were used both in the model and in the collection of the data are shown in Table 3.1. The power reaching the detector in the experiments was held as closely as possible to approximately $15 \mu\text{W}$, which is the value used in the models. This value was chosen because the detector saturates at about $50 \mu\text{W}$. In the 16 element model, it was assumed a detector that has a much higher saturation value (several mW) was used, and the value of the power per element on the detector was kept at $15 \mu\text{W}$. Such a detector is available but was not used in these experiments.

IV. Description of Experiments and Equipment

Section 4.1 High Power Fiber Amplifier Laboratory

The phase noise experiments were conducted at the Air Force Research Laboratory (AFRL) High Power Fiber Test Bed. The test bed is a government facility consisting of 16 150W fiber lasers that are suitable for coherent beam combination experiments; that is, the fiber lasers are polarization-maintaining and capable of narrow-linewidth and high power operation without deleterious non-linear effects such as stimulated Brillouin scattering. Figure



Figure 4.1. Nufern amplifier in the AFRL High Power Fiber Laser Test Bed.

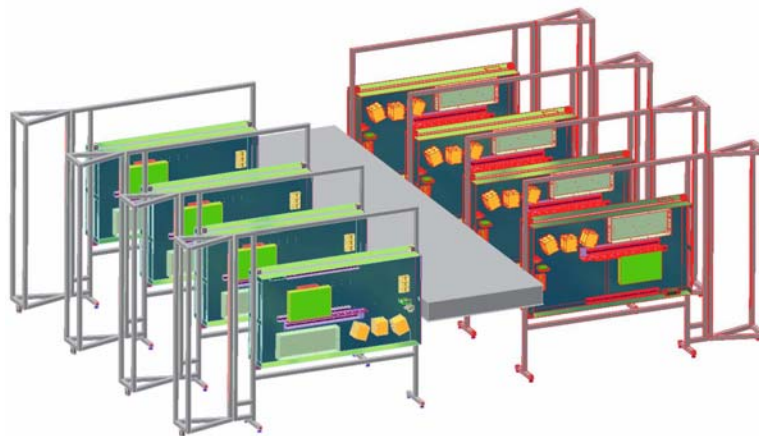


Figure 4.2 Arrangement of amplifiers in AFRL High Power Fiber Laser Test Bed.

4.1 shows a photograph of one of the 16 units. The purpose of this test bed is to characterize the operation of the high power fiber lasers and provide an independent laboratory environment for testing coherent beam combination techniques. The 16 units are arranged in a laboratory as shown in Figure 4.2. A common master oscillator is used to provide a coherent signal to each amplifier. A JDSU Nonlinear Planar Ring Oscillator operating at about 700 mW is used in these experiments. The power from the oscillator is amplified and then sent into a polarization maintaining optical fiber that feeds a 1 x 2 fiber splitter, and each of these two signals feeds a 1 x 8 fiber splitter to form the low-power master oscillator sources for the sixteen elements of the test bed at approximately 10 mW each. The light from each element then passes through a phase modulator, coupled into a polarization-maintaining optical fiber and subsequently coupled into a pre-amplifier to

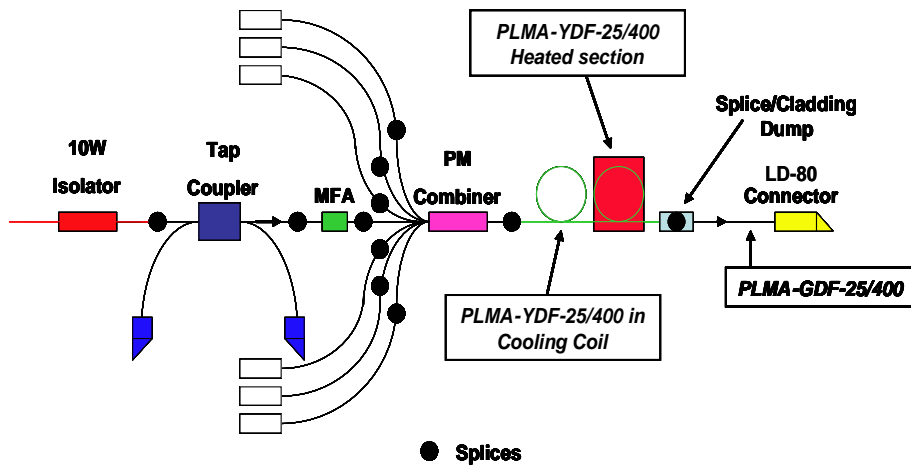


Figure 4.3. Schematic of a typical AFRL fiber laser amplifier.

increase the power in each element to approximately 200 mW. After the preamplifier, the power is coupled into an intermediate amplifier, which increases the power in each element to approximately 5 W. This optical power then feeds the final power amplifier as shown in Figure 4.3. The components shown in the figure are optically isolated to prevent any

feedback from the amplifier to the amplification stages before it. A tap coupler is used to monitor the signal and any feedback from the amplifier and a mode field adapter (MFA) is used to transition the power between the different sized fibers.

The polarization maintaining fiber of each element is fed into a pump combiner, where it is pumped by fiber coupled diode bars, which feed the PLNA-YDF 25/400 gain fiber. The gain fiber is cladding pumped and has a heated section and a cooling section as shown. This two temperature method mitigates SBS by providing a thermal gradient in the fiber. The input optical power from the intermediate amplifier is amplified in the gain fiber to 150 W, and the remaining pump power is coupled to a cladding dump where any unabsorbed pump power is removed. From there the output light is coupled into a PLNA-GDF 25/400 delivery fiber and out coupled to the experiment.

Several experiments were conducted to obtain the phase noise data and to obtain intensity data with the closed LOCSET phase control loop open and closed. The LOCSET electronics were used as described in the theory section. A detailed electronic schematic of these electronics is provided as Appendix 2.

Section 4.2 Phase Noise Experiments

In the phase noise experiments, the master oscillator is split into two elements, and each element configuration varied for the different purposes of the experiment. Phase noise data was taken by sampling the output of a single high power fiber amplifier and interfering it with a low power, unamplified, sample from the seed source in a Mach-Zehnder interferometer configuration, and measuring the beat frequency produced from the interference. The unamplified reference beam from the seed source is frequency shifted by approximately 80 MHz by an acousto-optic modulator, and the elements are then combined by a 2 x 2 fiber combiner. The beat frequency is detected by a photo diode, and the signal is demodulated by a Tektronix RSA3300B Real-Time Spectrum Analyzer to obtain the phase noise data in both time and frequency domain. The open loop phase noise data configuration is shown in Figure 4.4. In this configuration, one element does not undergo any

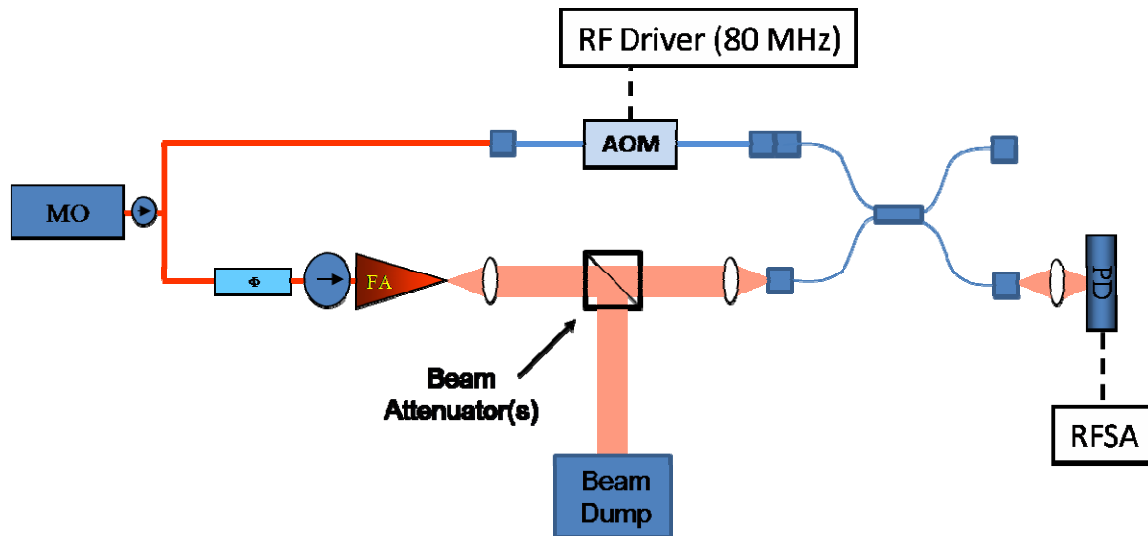


Figure 4.4 Experimental set up for open loop phase noise measurement.

amplification in order to keep that element as noise-free as possible. The other element is amplified to various power levels, attenuated, and interfered with the frequency-shifted

reference beam as discussed above. Three sets of data from this experiment were collected and used in this research. The first two were continuous operation of the amplifier for a total of approximately 200 seconds, with both amplifier turn on and steady state operation. The third was continuous operation of the amplifier for 50 seconds, including amplifier turn on, followed by 150 seconds of un-amplified operation where the amplifier was turned off after 50 seconds. Data collection of the intermediate amplification continued, providing phase noise data, continued through the unamplified power amplifier. The data was analyzed to provide phase noise versus time and then transformed to provide phase noise versus frequency. Analysis of the collected data is discussed in Chapter V.

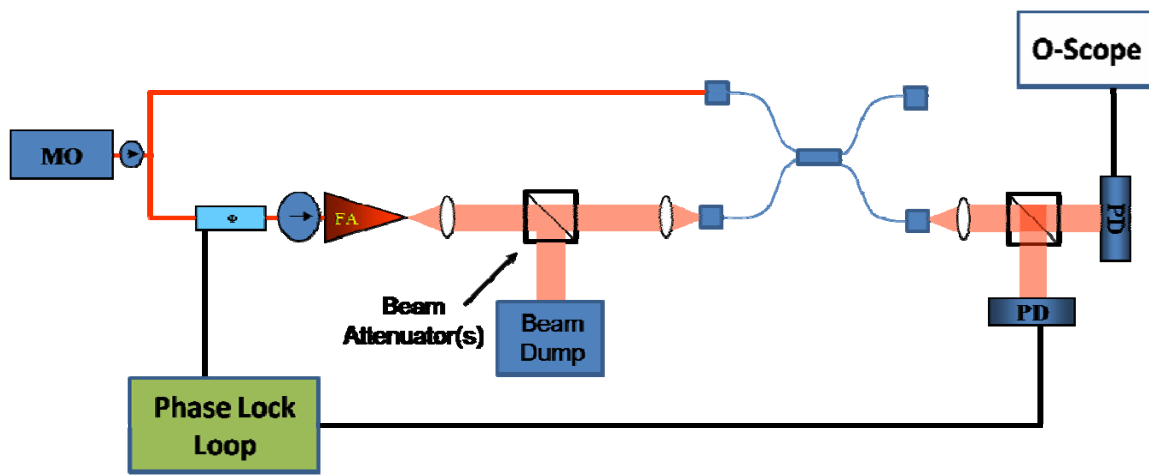


Figure 4.5 Experimental set up for closed loop phase noise measurement.

Due to equipment failure and limited available time for these experiments in the laboratory, the measurement of the phase noise during phase locking with the setup described above was unable to be accomplished. The following experimental setup was used instead, and is shown in Figure 4.5. The output of the fiber amplifier is attenuated and then interfered with a reference beam (sampled from the seed source) via a 2 x 2 splitter. The combined beam is then split into two separate beams via a beam splitter. Each beam is then incident on

a separate photodetector. The signal from one photodetector is used in the LOCSET control loop for phase optimization. The second photodetector is used for independent monitoring of the system performance. The intensity data measured by the independent photodetector was then analyzed and a relative measurement of the phase information was determined. Both the intensity data and the analyzed phase noise from that data are discussed in Chapter V, Results.

V. RESULTS

Section 5.1. Analysis of Open Loop Phase Transient and Noise Data

Open loop phase was recorded for three data sets. In each case, data were recorded from the turn on of the amplifier for 200 seconds. The first two cases, shown in Figures 5.1a and 5.1b, the amplifier was operated continuously through the data recording. In the third case, shown in Figure 5.1c, the amplifier was turned off after approximately 60 seconds of operation.

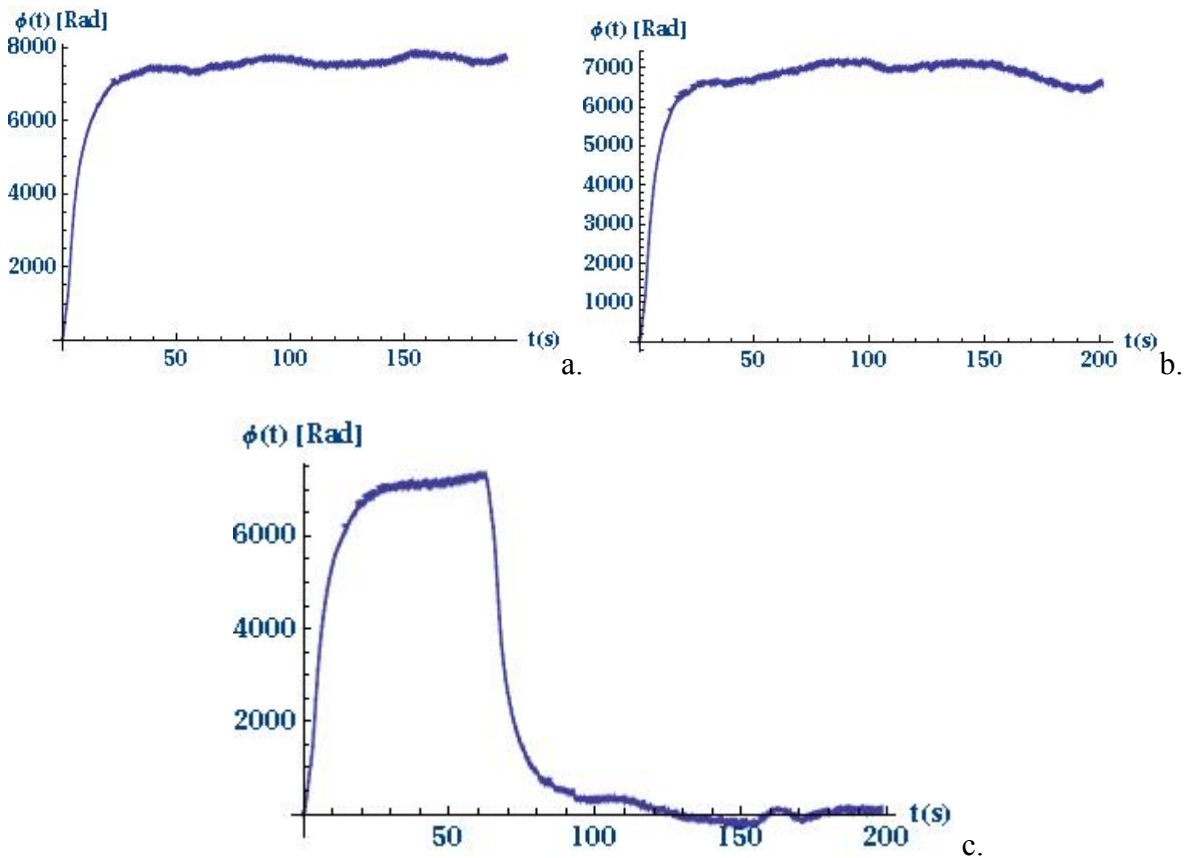


Figure 5.1 Open loop phase noise data versus time for three experiments. a and b are 200 are fiber amplifier start for 200 seconds of operation. c is fiber amplifier start for 50 seconds of operation and 150 seconds of cool down.

The phase noise at the beginning of each run was found to be very similar, so discussion will be on one representative data set. The first 30 seconds is shown in Figure 5.2.

As can be seen, inflection points are evident at approximately four seconds and one at

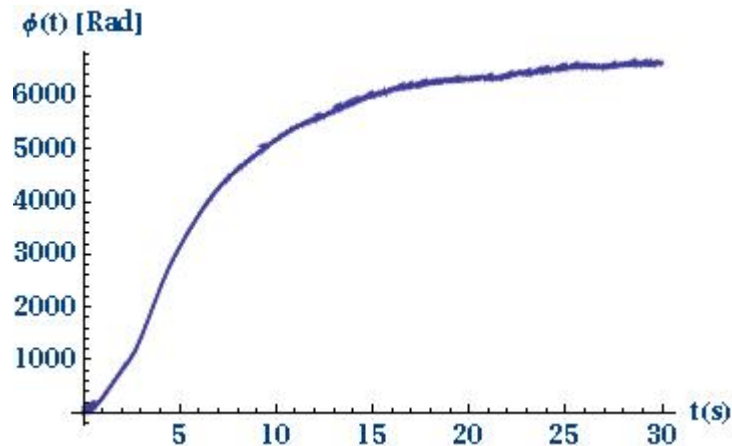


Figure 5.2. Representative open loop phase noise versus time for 30 seconds of initial operation.

approximately 10 seconds. In between these points, the data appears somewhat linear. The slower initial linear rise was found to be unusual when compared with previous experiments [6, 7, 19]. Upon investigation, it was found that only one of the two sets of diode pumps is activated initially, and the second set is activated a few seconds later. Also, the AFRL system uses an RC circuit to slow the initial current surge. A problem was encountered in integrating these amplifiers with the power supplies. A current spike was encountered upon initial turn on of the amplifiers. To manage this spike, an RC circuit was installed which delayed the full current for several seconds. Primarily, the delay in activating the diode pumps and, to a lesser degree, the RC circuit causes the amplifier current to ramp which causes the heating of the fiber to be slower for the first few seconds of operation. The slopes of the phase versus time data were calculated on the data sets using a linear regression for the

periods 1-3 seconds, 4-6 seconds and 11-16 seconds to compare with previous results from other experiments. The results of that calculation are shown in Table 5.1.

Linear Regression	Radians/sec			Waves/sec		
	Run #	2	4	5	2	4
1-3 sec	543	540	493	86.4	85.9	78.5
4-6 sec	682	772	833	108.5	122.9	132.6
11-16 sec	147	156	144	23.4	24.8	22.9

Table 5.1. Results of Linear Regression Calculation on Phase Transient Data.

This data compares to the previous research of Augst [6] where the initial rate of increase was 20 waves/sec before reaching steady state. The data from Jones [19] resulted in a much higher rate of phase transient of approximately 320 waves/sec. This is calculated at two seconds after start up when the pump is at full power from the deterministic equation

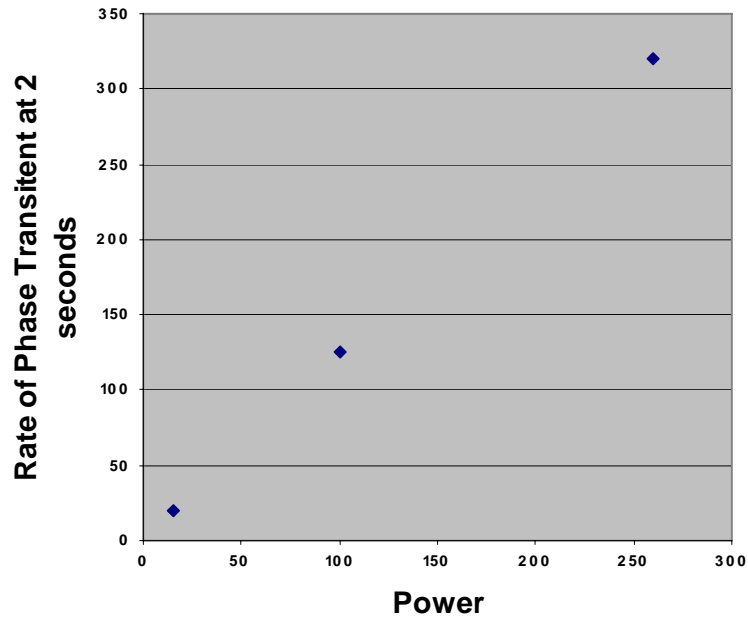


Figure 5.3. Data points of the slope of the phase transient data versus time indicating the linear nature of the phase changes due to power during initial heating of the fiber amplifier.

provided in that reference. The data discussed from these three experiments are plotted together in Figure 5.3. That is, the rate of change of phase transient versus power are plotted for the Augst [6] experiment, the Jones [19] experiment and the AFRL data. As can be seen, the results indicate a linear behavior of the data. The data were analyzed and a best fit slope of 1.22 Hz/W and an intercept of 2.03 Hz were computed.

Figure 5.4 shows phase noise recorded in the AFRL system, that is, the steady state behavior of the phase after the phase transient when the system appears to be in steady state after 20 seconds of operation. As can be seen in the data, a large fluctuation of phase is still

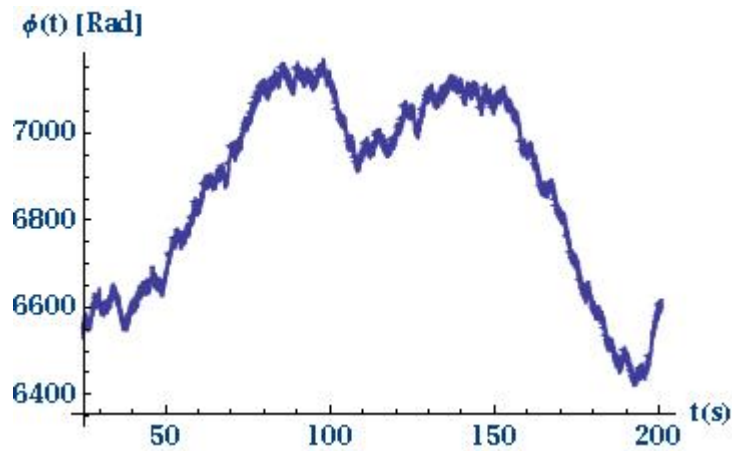


Figure 5.4 Steady state phase noise versus time.

evident. This fluctuation is most likely due to the large industrial chiller that provides cooling to the fiber amplifiers. The chiller provides cooling water at $17^{\circ} \pm 1.5\text{-}2^{\circ}$ C. This phase change would correspond to the path length change of the fiber on the cold spool during the temperature swings of the chiller. Three meters of fiber are on the cold spool, and the thermal length constant of the silica fiber used is

$$\alpha = \frac{\Delta n l}{n l \Delta T} = 1.2 \times 10^{-5} C^{-1} \quad (53)$$

where Δnl is the change of length of the fiber times the index of refraction, nl is the length of the fiber times the index of refraction, and ΔT is the change of temperature. The data is reviewed to determine the maxima seen at 95 seconds and minima seen at 190 seconds which are 7160 and 6440 radians, respectively resulting in a $\Delta\phi$ of 720 radians, which corresponds to about 115 waves, which at the wavelength of operation would be about 120 microns. Assuming for the small changes in temperature, the index of refraction of the silica fiber remains constant, then from equation (53)

$$\Delta T = \frac{\Delta nl}{nl\alpha} = \frac{120 \times 10^{-6} m}{3m \cdot 1.2 \times 10^{-5} C^{-1}} = 3.3^{\circ}C \quad (54)$$

This result substantially supports the understanding of the large phase drifts in steady state being due to the large industrial chiller. The data recorded when the amplifier was turned off is also of interest, and this data (from 25 to 200 seconds) is shown in Figure 5.5. A negative phase transient is evident immediately upon turn off, and the slope of the transient is measured with a linear regression and found to be -760 rad/sec. This is very similar to the rate of change on start up of the amplifier, which was measured at 833 rad/sec. After the

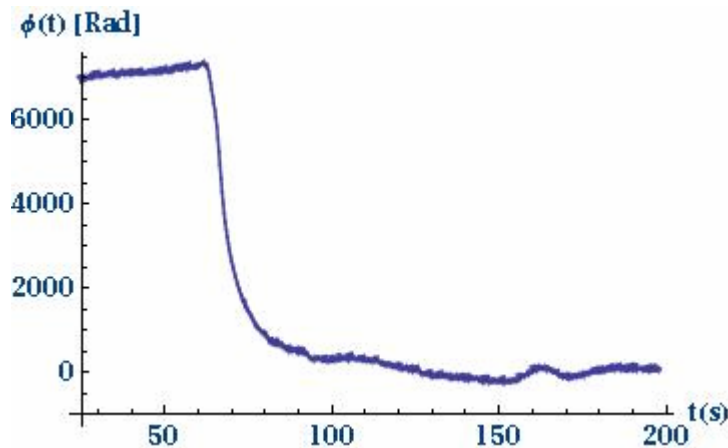


Figure 5.5 Phase noise versus time for steady state operation and after turn off of the amplifier.

initial rapid decrease in phase immediately after turn off of the amplifier, a slower trend is observed and similar fluctuation occur due, again, to the industrial chiller. The change in phase due to this effect after turn off is 561 radians, which is very similar to the previous measurement while the amplifier was on and at steady state. A similar calculation as that above results in $\Delta T = 2.6^{\circ}C$. Interestingly, long after turn off of the amplifier, the chiller caused the phase drift to reach a value that was less than the initial phase recorded prior to amplifier operation, indicating that the temperature of the fiber was cooled below that which it was at initial amplifier operation.

The phase structure function (PSF) is computed in steady state operation [7]. This calculation quantifies the average phase noise deviation after a time τ and is given by

$$PSF(\tau) = \left\langle \left| \Delta\phi(t) - \Delta\phi(t + \tau) \right|^2 \right\rangle \quad (55)$$

where, in this calculation, t varies over a 7.5 second time period. The phase over this time period is shown in Figure 5.6 and the the PSF curve is shown in Figure 5.7.

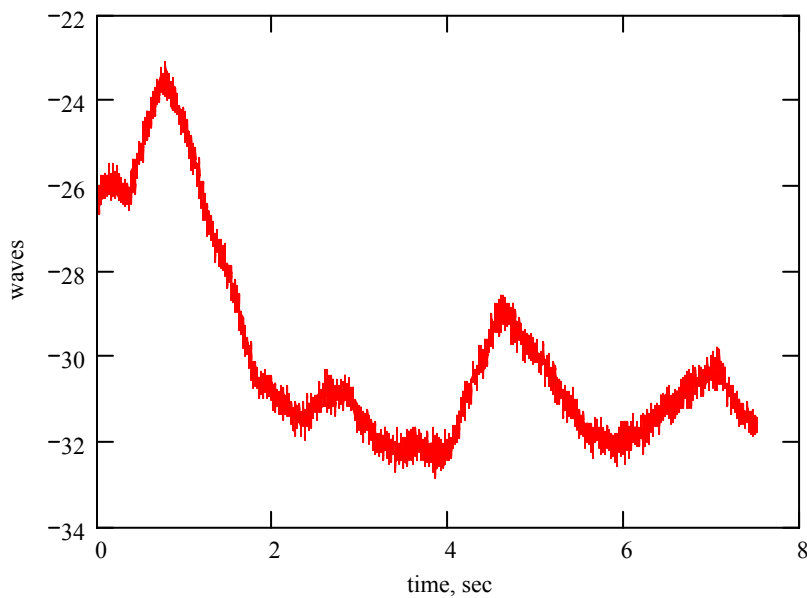


Figure 5.6 Phase noise versus time for short time span in steady state.

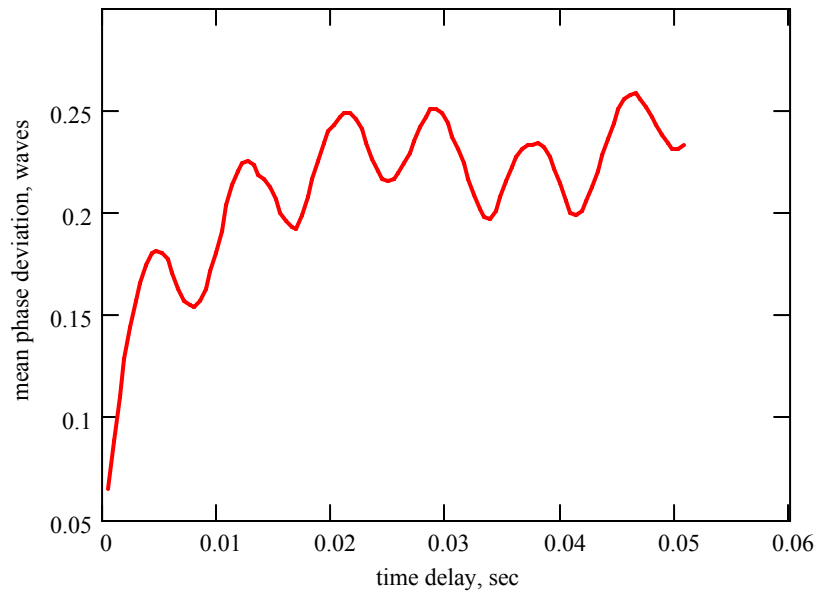


Figure 5.7 Phase structure function curve for open loop phase noise in steady state.

This shows that the average phase deviation between adjacent data points is over .05 waves and is greater than 0.15 waves within msec, indicating that a very robust phase control loop is required to control the phase to a tenth of a wave or better. The data become more stable after a time delay of approximately 20 msec but continue to display an interesting oscillation between approximately 0.2 and 0.25 waves. This data differs widely from the data collected in by Jones [7], where the mean phase deviation was found to be much more linear and accumulated at a slower rate. In those experiments, 20 msec was required to attain a mean phase deviation of 0.05 waves, and the maximum after 50 msec was 0.10 wave.

To gain further insight into the rapid phase noise, a plot of the phase noise in steady state over a very short time period of 100 msec is shown in Figure 5.8. This plot

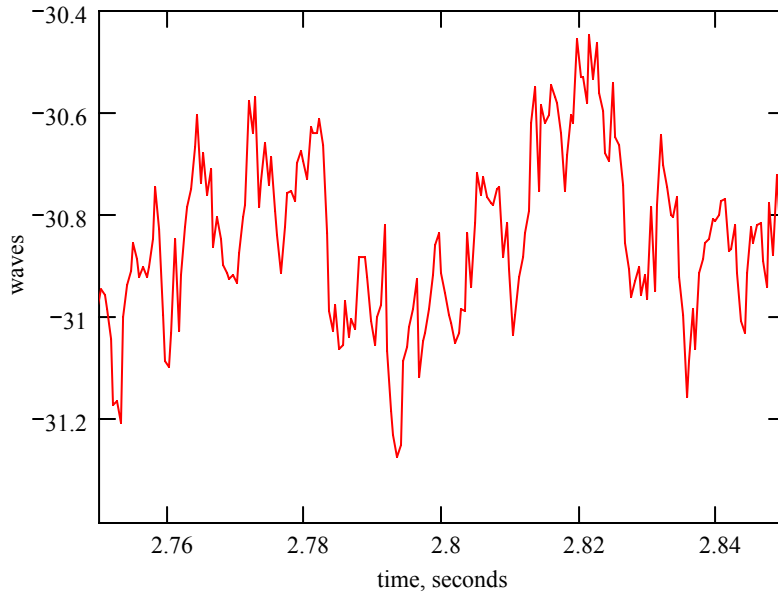


Figure 5.8 Phase noise versus time over very short time duration.

further illustrates the rapid phase changes encountered in these amplifiers and the need for a robust high speed phase control loop.

Section 5.2. Analysis of Open Loop Phase Noise Power Spectrum

A phase noise power spectrum was computed for each of the three runs discussed in the previous section. As with the data in the time domain, the two runs where the amplifier was run continuously were very similar, and only one representative data set requires discussion. The data was separated into three spectra from 0-1 Hz, 0-100 Hz, and 100-1000 Hz.

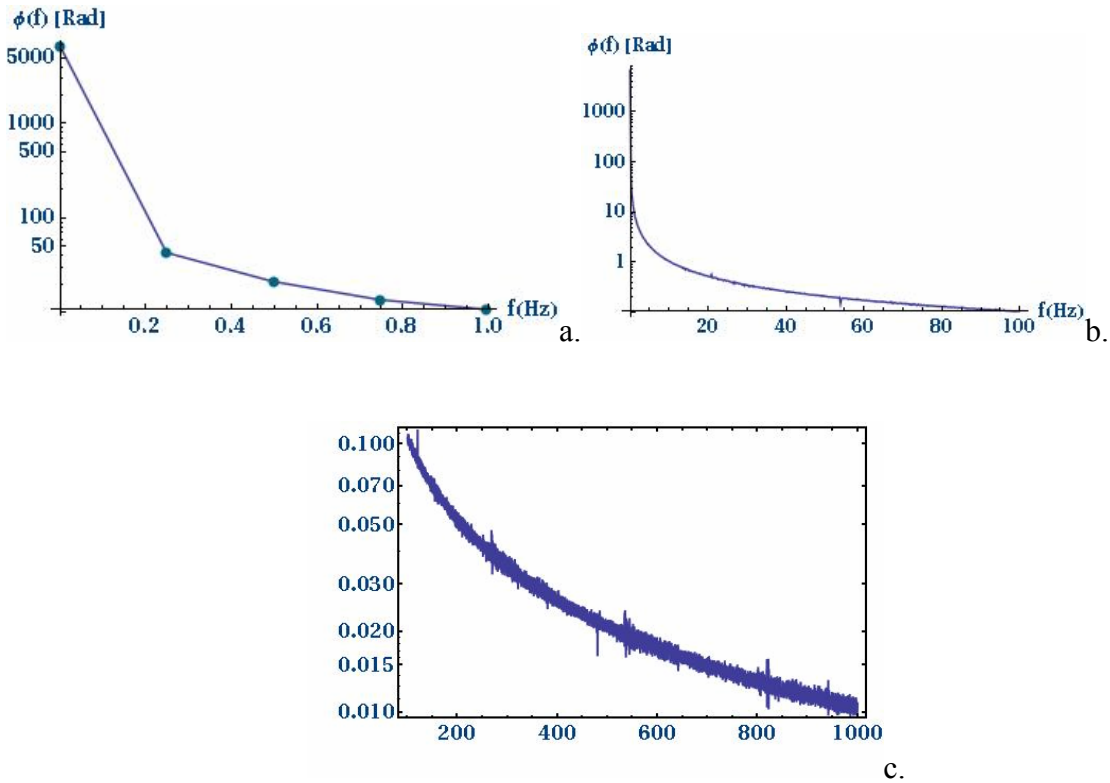


Figure 5.9 Phase noise power spectrum versus frequency for three spectra. a) 0-1 Hz, b) 0-100 Hz, and c) 100-1000 Hz.

Representative data when the amplifier was operated continuously for 200 seconds is shown in Figure 5.9. The maximum is over 1000 radians at the lowest frequency and drops off very sharply to less than one at approximately 20 Hz. Compared to the Augst data [6], a drop of the first three orders of magnitude was at approximately 1 kHz. This implies much more of the noise in the AFRL amplifiers is at lower frequencies. That is, a much sharper decrease is

evident in the AFRL amplifiers than was reported for the MIT/LL results. The drop off continues to the extent of the analysis at 1 kHz, where a five order of magnitude total drop off is recorded. The MIT/LL data also shows a five order of magnitude total drop off reaching that level at approximately 200 kHz. The frequency of two different regions in the time domain was analyzed separately for one of the data sets. A frequency spectrum from 0-45 seconds, which incorporates the phase transient data, and a spectrum from 45-200 seconds, which includes only steady state phase noise data, were analyzed separately. These data and the spectrum for the entire data set are shown in Figure 5.10. This demonstrates that all frequencies dominate during the initial turn on of the amplifier and all frequencies are

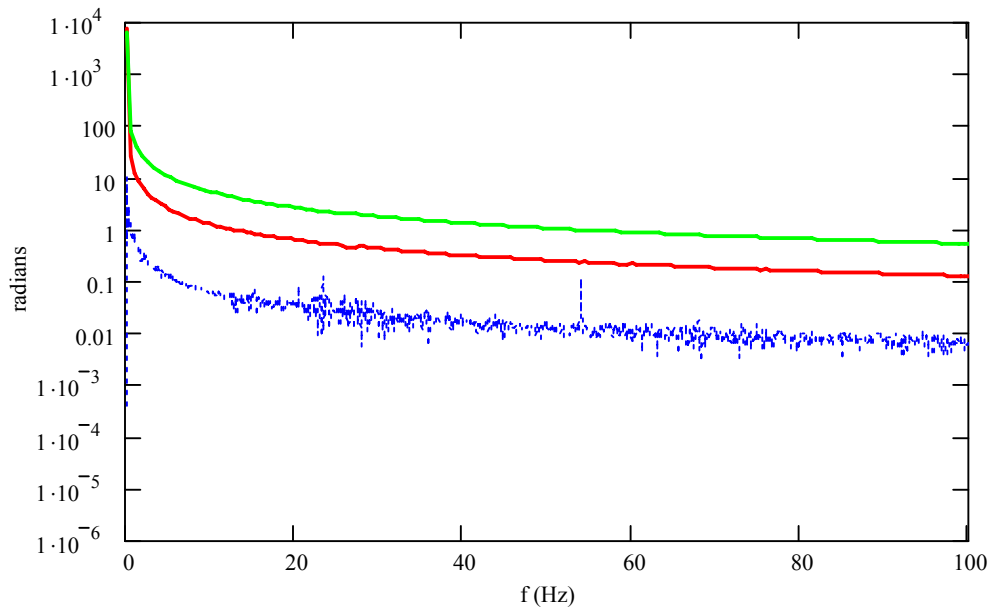


Figure 5.10. Phase noise power spectrum for 0-45 seconds (green), 45-200 seconds (blue) and 0-200 seconds (red).

at a lower magnitude during steady state operation. Consequently, any phase control loop would be most challenged during the initial turn on of the amplifier.

Section 5.3. Modeling of Open Loop Phase Noise and LOCSET Bandwidth

The model was prepared for both a generic 16 element of input data and for the specific case of two elements. The two element model was run using actual open loop phase noise data. The two elements are extremely similar, so only one case is illustrated. Figure 5.11 shows the actual phase noise data versus frequency plotted with the modeled closed loop phase noise versus frequency. A logarithmic scale must be used to illustrate the magnitude

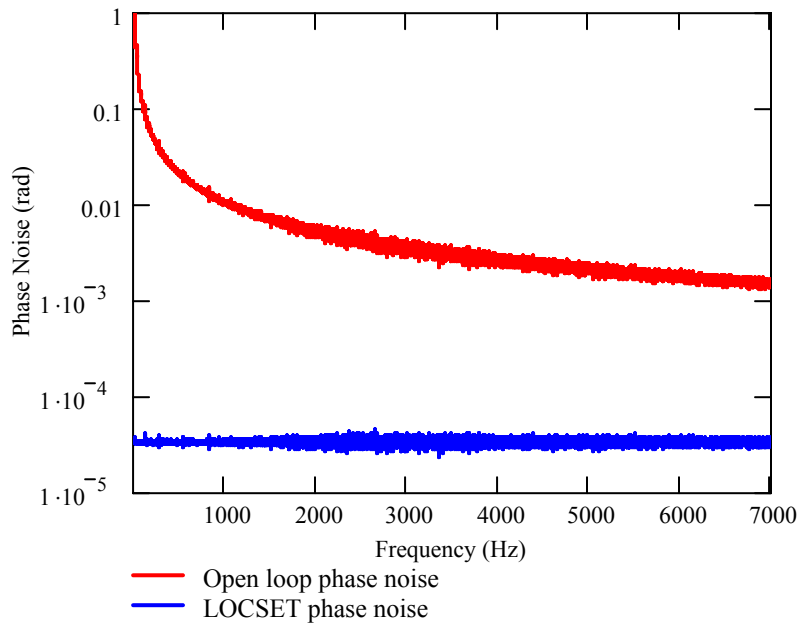


Figure 5.11 Actual open loop phase noise and LOCSET modeled closed loop phase noise versus frequency.

of the suppression of phase noise due to LOCSET. As can be seen, the LOCSET model predicts well over an order of magnitude of phase noise suppression. An interesting feature of the model is the near constant value of the modeled closed loop phase noise.

From equation (42) the control loop gain for the *i*th element can be calculated. That is, since

$$\delta\phi_i(s) = \frac{s\Delta\phi_i}{s + \frac{A_e K_{PM}}{\tau} \sum_{\substack{j=1 \\ j \neq i}}^N K_{ij}}$$

the loop gain, G_L can be written as

$$G_L = \left| \frac{s}{s + 2\pi BW} \right|^{-1} = 1 + \frac{2\pi BW}{s} \quad (56)$$

where BW is the bandwidth of control loop for that element as defined in Equation (44). As can be seen, the loop gain and bandwidth of a control element will increase when the total number of elements increases. To illustrate this, the LOCSET model was executed with two elements and with 16 elements, and the control loop gain as a function of frequency was determined. These results are shown in Figure 5.12. As can be seen the gain increases by

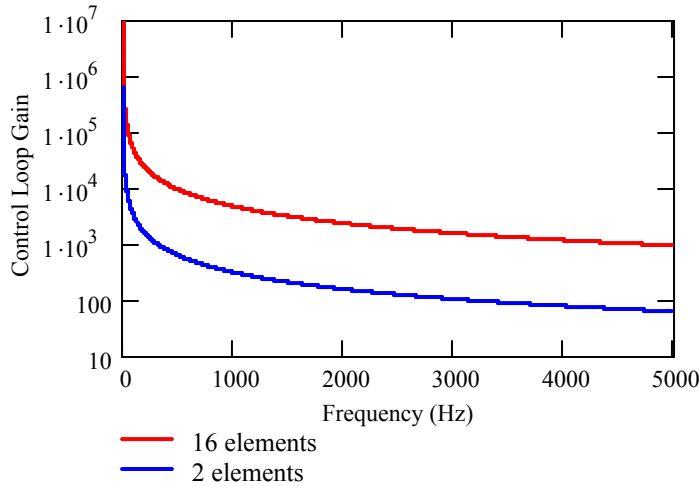


Figure 5.12 LOCSET Control Loop Gain for 2 elements (blue) and 16 elements (red).

approximately an order of magnitude due to the additional elements. This corresponds to the decrease in phase noise predicted by the model. The bandwidth for each case is calculated

and is found to be 3.1×10^5 and 4.7×10^6 Hz for the two and 16 element systems, respectively. The feature of the loop gain curve helps explain the linear nature of the modeled closed loop phase noise noted above. That is, a near constant value is foreseeable when the open loop phase noise is divided by the loop gain. The increase in loop gain for additional elements will provide more suppression of open loop phase noise, thus further illustrating the advantages that LOCSET has for larger number of elements. The conclusion drawn is that higher frequencies are controlled with greater number of elements. In this case, an order of magnitude advantage is realized with 16 elements over 2 elements.

Section 5.4. Analysis of Closed Loop Data and LOCSET Model Results

The data collected at the power detector with the loops open is shown in Figure 5.13. As can be seen, the random phase changes within both amplifiers are uncorrelated resulting

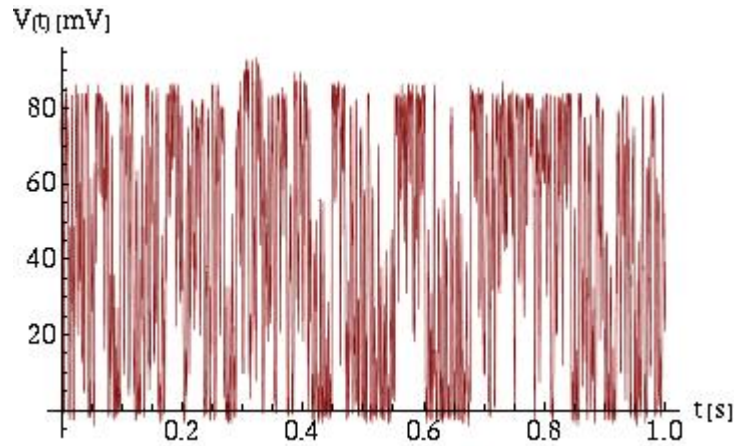


Figure 5.13 Intensity of two beams with random phase versus time.

in random constructive and destructive interference of the light. In contrast, Figure 5.14 shows the power collected at the detector with the phase lock loops turned on, resulting in a

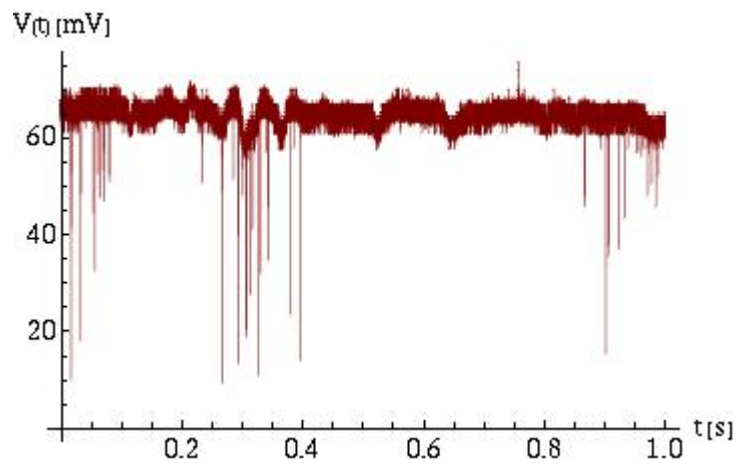


Figure 5.14 Intensity of two high power beams with phases locked by LOCSET.

very stable intensity in the combined power into the detector, indicating the beams are very much in phase. Observing the data, several drops in power can be seen. This is attributed to the intensity fluctuations observed in the amplifiers during their operation. As an example of this fluctuation, data was taken with only one beam present and is shown in Figure 5.15.

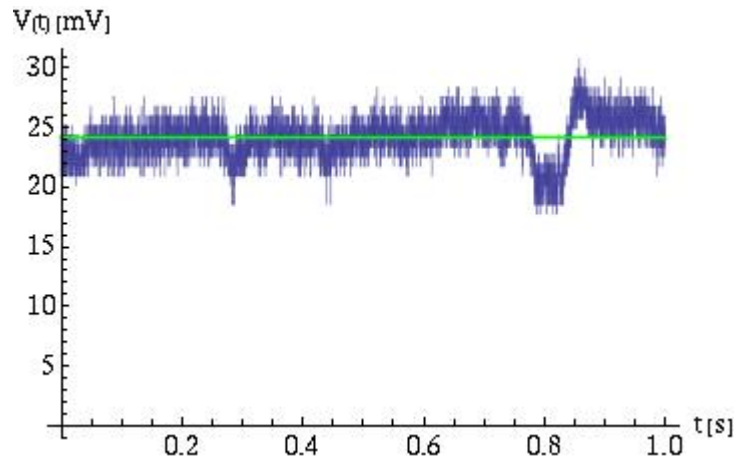


Figure 5.15 Intensity of a single high power beam.

These intensity fluctuations when combined can result in the behavior seen in the combined beams. Even with no amplification, there is a substantial amount of intensity noise in the

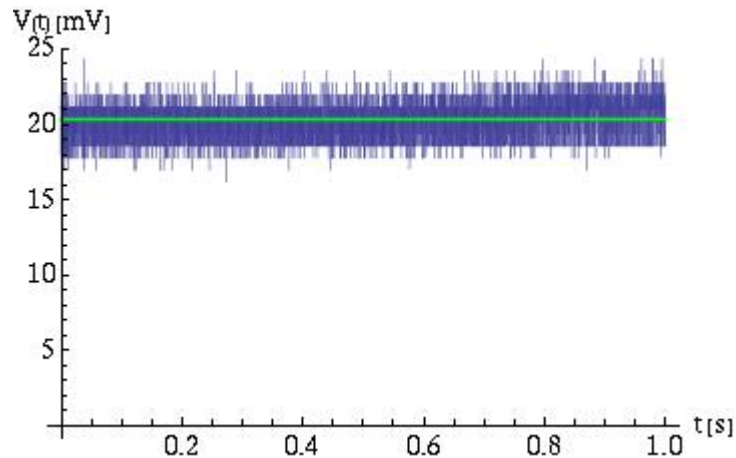


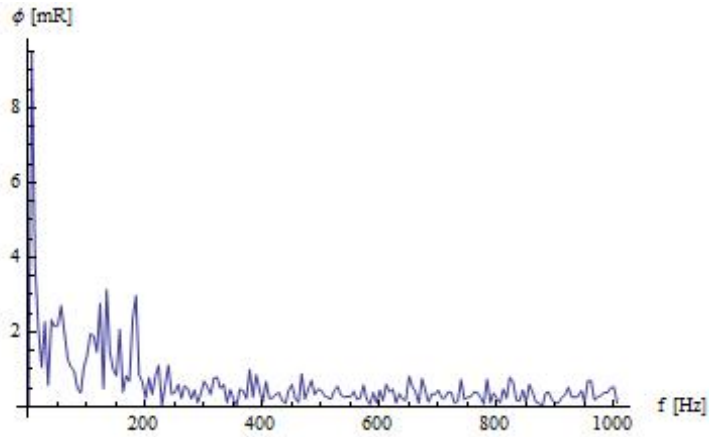
Figure 5.16 Intensity of single reference (low power) beam only.

system. Figure 5.16 shows data collected with the reference beam only and no high power beam providing further illustration of the noise in the system. This does not fully explain the sharp spikes seen in the closed loop data of Figure 5.14. These spikes appear to be resets in the LOCSET control system where the system is not coherently combining the beams but is, albeit for a very short time, resetting itself.

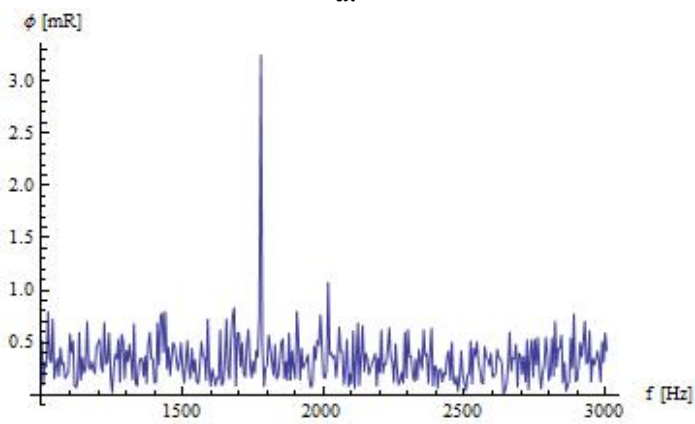
As discussed in Section 4.2, closed loop phase noise was not collected during these experiments, but the data discussed above was post-processed and analyzed, and a relative phase noise measurement versus frequency was determined. This data is shown in Figure 5.17.

The observations of the data shows some higher magnitude phase noise under 200 Hz but is substantially lower, except at very low frequencies, than the phase noise observed in the open loop case (Figure 5.10). The open loop phase noise at very low frequencies (less than 10 Hz) is between 20 and 1 radians, while the closed loop for this band is less than 10 milli-radians and mostly only a few milli-radian. The remaining closed loop data, although quite noisy, is relatively constant at an average of about 0.5 milli-radian. The open loop data drops well below a radian but never below 10 milli-radian. An interesting observation from the data is the spikes at approximately 1800 Hz and a very dominate spike between 15,600 and 15,700 Hz. The later spike is due to the frequency of the LOCSET circuit. This frequency is used to provide LOCSET the ability to control very slow varying changes in phase. It is a small imposed phase error. The spike at 1800 Hz is not easily explained.

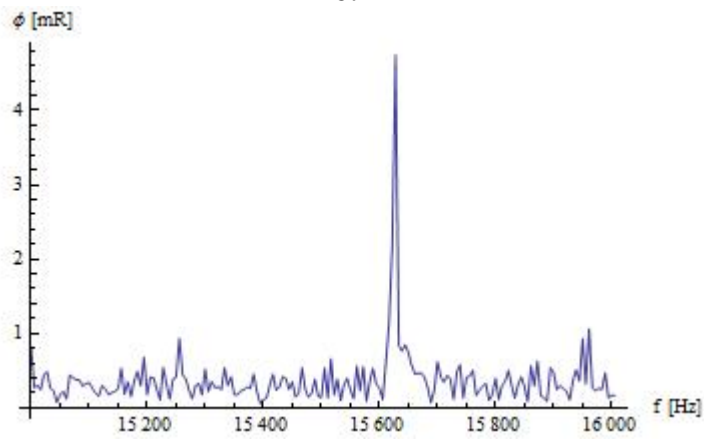
The actual closed loop data was compared to the closed loop data predicted from the LOCSET model that was presented in Section 5.3. Those two data sets are plotted together



a.

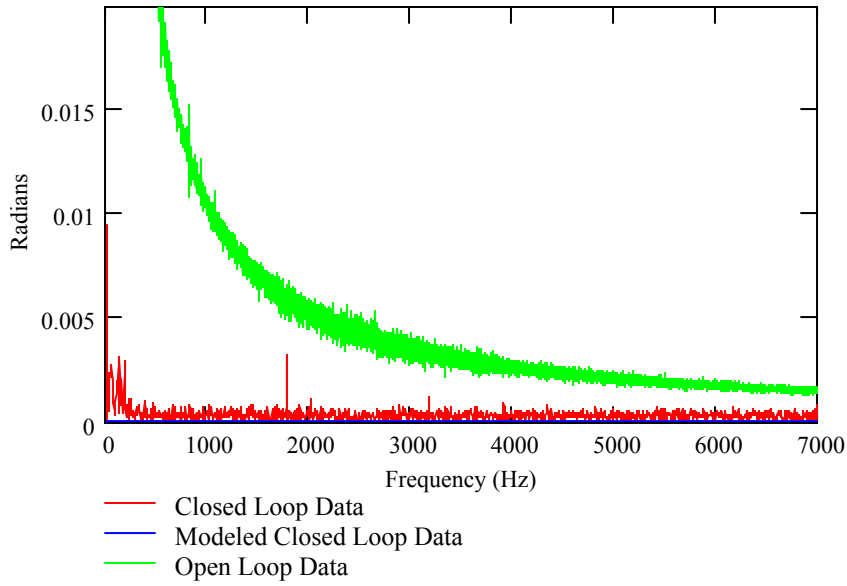


b.

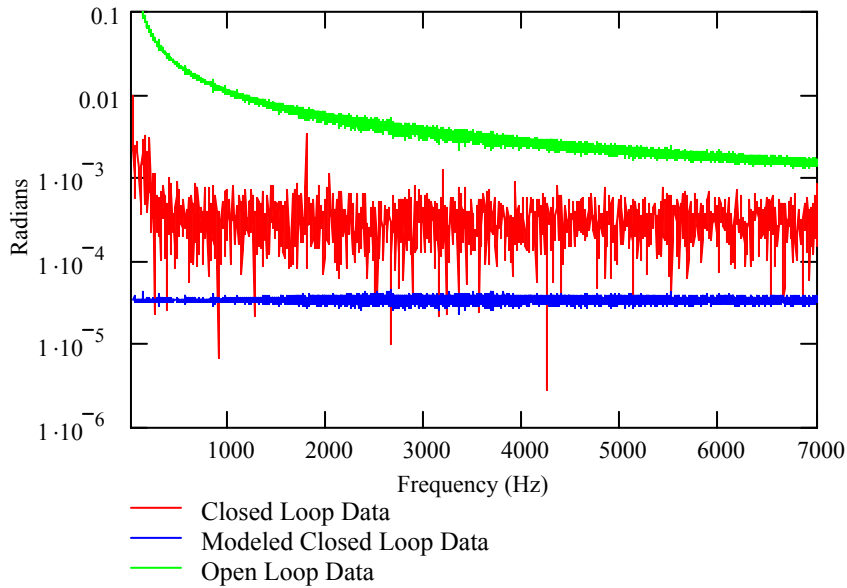


c.

Figure 5.17. Phase noise frequency spectrum for closed loop phase noise as analyzed. a) is from 0 to 1000 Hz, Figure b) is 1000 to 3000 Hz. and c) is from 15,000 to 16,000 Hz.



a.



b.

Figure 5.18 Modeled closed loop data, closed loop data calculated from intensity data and open loop data plotted versus frequency. a. is a standard plot, b. is a logarithmic plot.

with the actual open loop data and is presented in Figure 5.18. As can be seen, the modeled closed loop data is overestimating the phase noise reduction that is observed in the actual

closed loop data. To better illustrate this, the same data is plotted on a log scale in Figure 5.18b. This clearly shows approximately an order of magnitude discrepancy between the actual closed loop phase noise data computed from the intensity data and the closed loop phase noise data modeled from the open loop data. A variety of reasons for this discrepancy are apparent. First, the control electronics introduce noise into the system that is not was not accounted for in the LOCSET model. Specifically, the inherent noise in the signal processing electronics and the deadband was not modeled. Secondly, some of the electronic

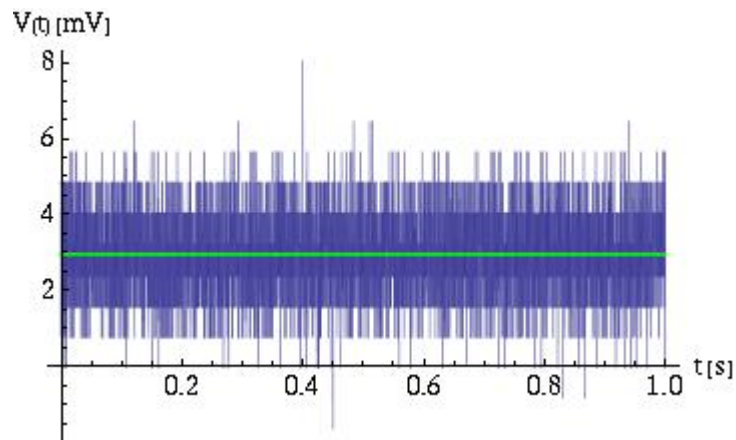


Figure 5.19 Power detector signal with no light.

constants may have been determined from catalogue values of the components used in the system and may not have been measured accurately, thus providing a source of error into the model. The third is, as discussed above, inherent noise in the system resulting in the large noise floor seen in Figure 5.16 when no high power beam was present. To further illustrate this last point, a measurement of the background intensity at the power detector was made. This data is shown in Figure 5.19. On the other hand, the LOCSET model successfully

predicts the steady nature of the phase noise. That is, the modeled closed loop phase noise is relatively constant as is the closed loop phase noise computed from the intensity data.

In conclusion of this section, a valid attempt to provide a model of LOCSET was provided. Noise inherent in the signal processing electronics and the deadband were not able to be taken into account, and the model, while matching some characteristics of the closed loop phase noise was consistently inaccurate by an order of magnitude due to unaccounted noise in the system.

Section 5.5 Results of Two Element Analysis

The two element analysis discussed in Section 2.5 was executed by evaluating per Equation (48) with various input for $\Delta\phi_1$ and $\Delta\phi_2$. The Mathcad program shown in Appendix 3 was executed with several functions for each input variable. Several functions were used. A cosine function, $\Delta\phi(t) = \cos(at)$, which has the Laplace transform of

$$\Delta\phi(s) = \frac{s^2}{s^2 + a^2}. \text{ This was used for both a low and high frequency input with } a = 100 \text{ and}$$

4000 respectively, which are termed ‘‘Cosine Low’’ and ‘‘Cosine High’’ and a unit step

Case No.	$\Delta\phi_1$	$\Delta\phi_2$
1	Cosine High	Cosine Low
2	Cosine Low	Cosine High
3	Step	Cosine Low
4	Cosine Low	Step
5	Step	Cosine High
6	Cosine High	Step

Table 5.2. Cases examined in two element analysis.

function $\Delta\phi(t) = u(t)$, which has the Laplace transform of $\Delta\phi(s) = \frac{1}{s}$. As discussed in

Section 2.5, cases when the input variables are equal are trivial as the output is equal to those

inputs. Consequently, only cases when the inputs are not equal are examined. The bandwidth for the system, BW , is purposefully kept low to better illustrate the effect of the coupling. As discussed in Section 2.5, a large bandwidth only results in the averaging of the two inputs. The inputs used are summarized in Table 5.2. The first result, case 1, was for two cosine waves with different frequencies. The results are shown in Figure 5.20. As can be seen, there is very little observable coupling of the element 2 into element 1. The coupling from element 1 is evident but is suppressed due to the control loop.

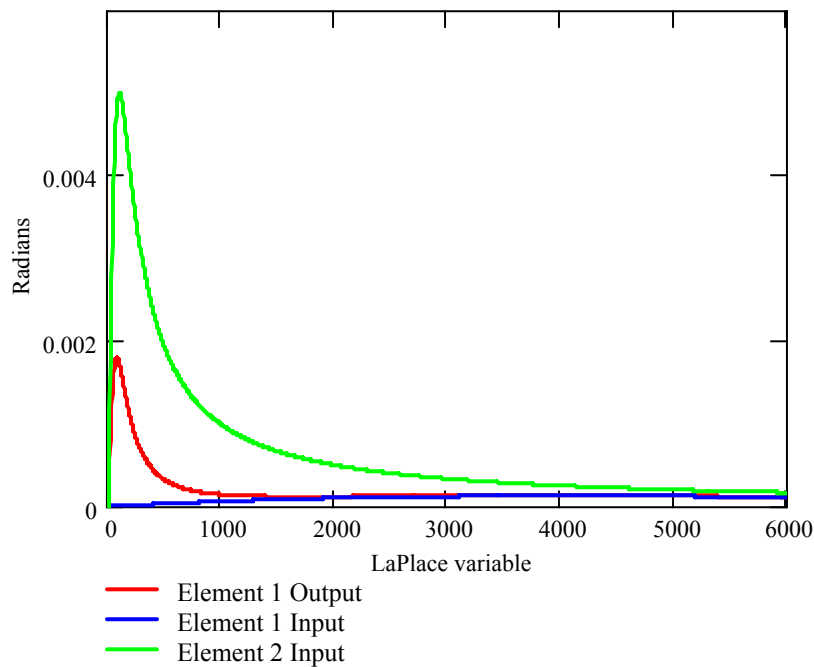


Figure 5.20 Two element analysis. High frequency and low frequency. Results of a low frequency and high frequency inputs to the two element analysis LOCSET model. Figure demonstrates some coupling of same element into the output and very weak coupling from the other element.

The next execution of the two element analysis was to switch these inputs and observe the coupling of a low frequency from the second element onto the first while a high

frequency was placed on the input of the first element. This result is shown in Figure 5.21 and shows the result where there is no evidence of any coupling of the high frequency from element 2 into the output signal for element 1. However, the stronger coupling of element 1 input into element 1 output is very evident, suggesting that, indeed, the control loops suppress coupling between the elements.

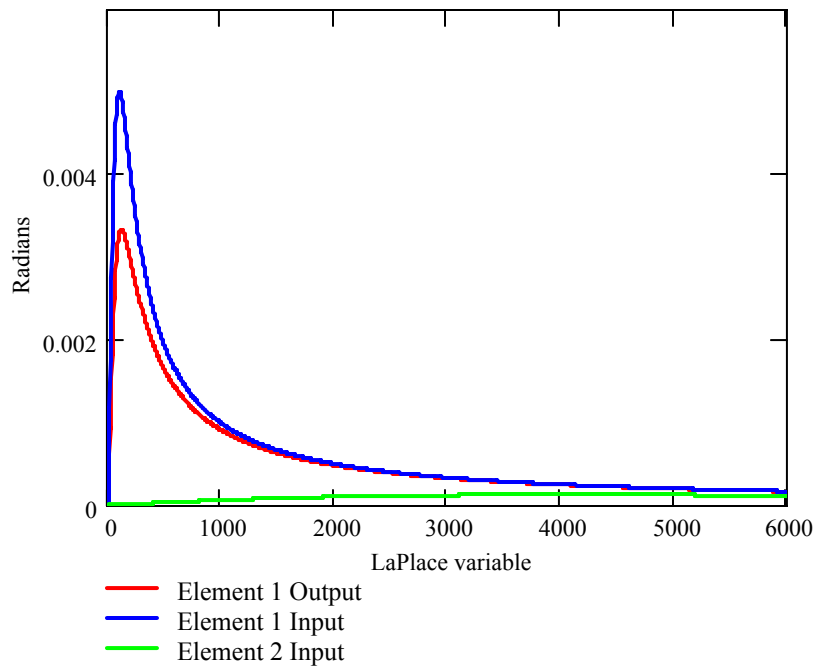


Figure 5.21 Two element analysis. Low frequency and high frequency. Results of element 1 control signal from a low frequency input from the open loop of element 1 and high frequency input from element 2. More coupling from the same element is observed and even less than previous case observed at high frequency.

The next case examined was a step function input on element 1 and a low frequency cosine on element 2. This result is shown in Figure 5.22. As can be seen, the step function

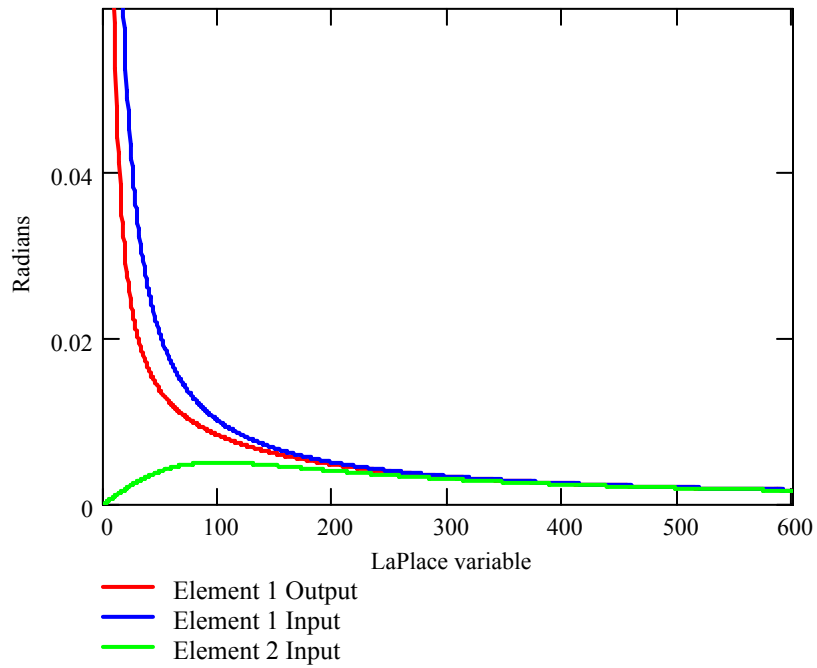


Figure 5.22. Two element analysis. Step function and low frequency. Results of element 1 control signal from a step function input from the open loop of element 1 and low frequency from element 2. Very little coupling from element 2 is observable onto element 1 output.

from the input of element 1 dominates the output of element 1 at low frequencies. Very little

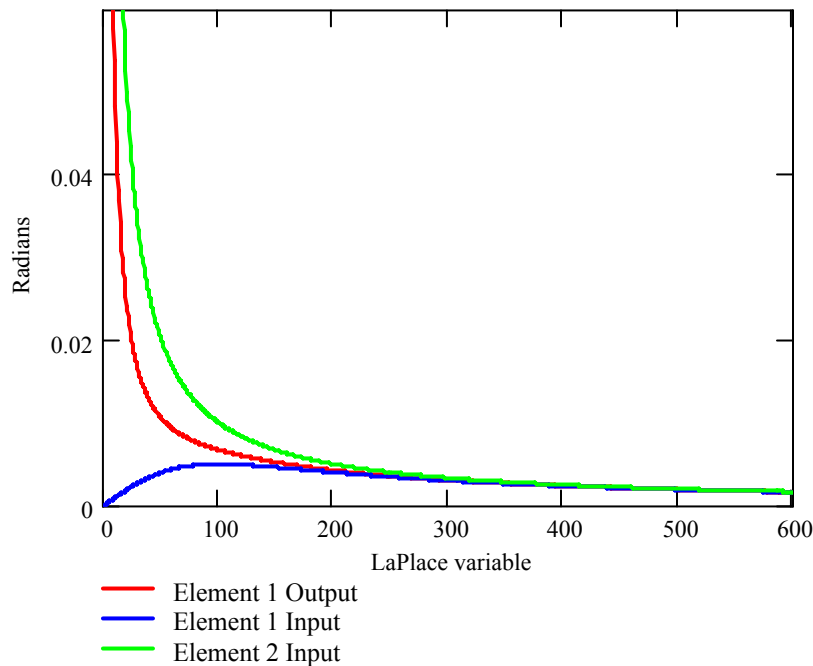


Figure 5.23. Two element analysis. Low frequency and step function. Results of element 1 control signal from a low frequency input from the open loop of element 1 and a step function from element 2. Less coupling from the step function is evident when it is not on the same element.

coupling from element two is observable as the output of element 1. Element 1 at low frequencies is dominated by the step function from the input of element 1.

The next case examined is with the step function on element 2 and a low frequency cosine on element 1. This result is shown in Figure 5.23. In this case, more coupling of a low frequency component occurred but much less coupling of the step function is obvious. This shows that less of the frequencies from the other element will couple into the control element, which validates the conclusions drawn regarding the LOCSET theory that little coupling from other elements is present. The final two cases are shown in Figures 5.24 and 5.25. These are the same cases as those shown in Figures 5.22 and 5.23, respectively, except that high frequency cosine inputs are used with step functions rather than low frequencies.

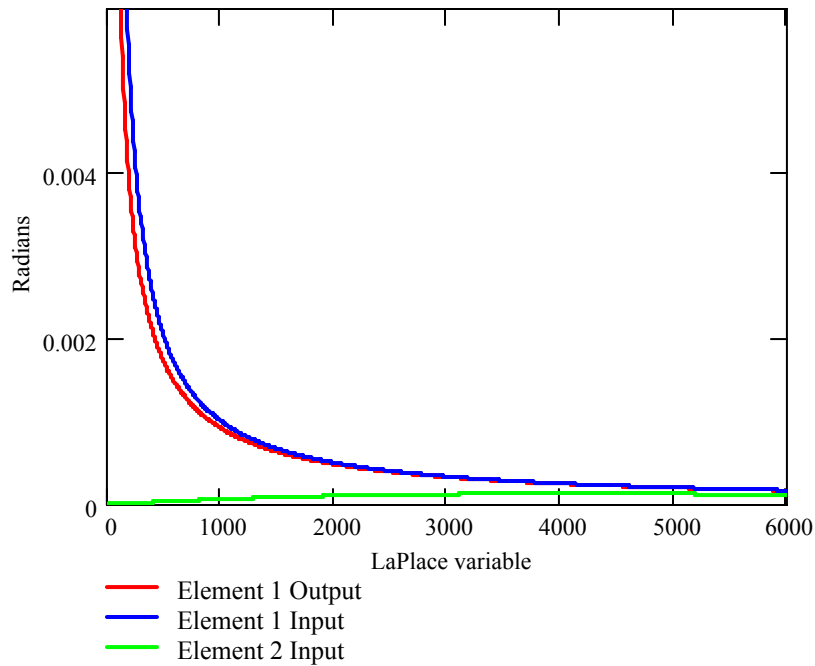


Figure 5.24 Two element analysis. Step function and high frequency. Results of element 1 control signal from a step function input from the open loop of element 1 and low frequency from element 2. The output is dominated by the step function. Very little coupling from element 2 is observable onto element 1 output.

The two element analysis demonstrates that with a lower bandwidth, much less coupling of frequencies from adjacent elements will be on the output elements. It demonstrates the control loops ability to control output phase to the average of the input phases. The output phase of the element will be somewhat dominated by the input phase and some coupling does occur from the adjacent element, but that coupling is less than what is from the input to that element.

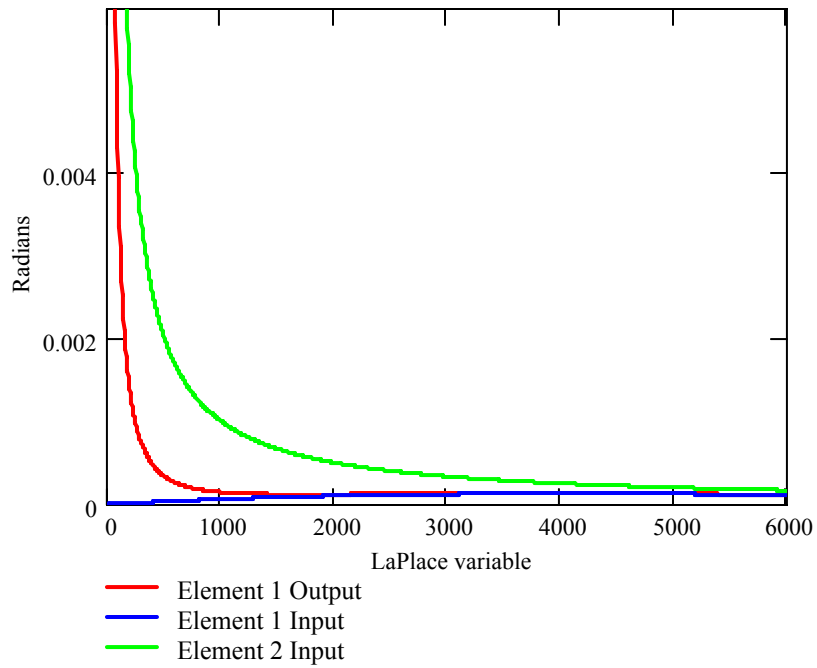


Figure 5.25 Two element analysis. High frequency and step function. Results of element 1 control signal from a low frequency input from the open loop of element 1 and a step function from element 2. Much less coupling from the step function is evident when it is not on the same element.

VI. Conclusion and Future Work

Section 6.1. Summary of Work and Results.

This thesis examined several topics whose understandings are important in the science of coherently combined high power fiber laser arrays. The basics of ytterbium fiber laser amplifiers were presented. The relative advantages of ytterbium over other rare-earth dopants were presented, and the benefits of dual-core pumping for these systems were discussed. The theory of stimulated Brillouin scattering was presented to illustrate the challenges in scaling the high power fiber arrays, further justifying the need for combining multiple amplifiers to attain the very high powers needed for military applications. A theoretical analysis of fiber laser amplifier phase noise due to amplified spontaneous emission was presented. It was determined, however, that this theory would often overestimate the phase noise, particularly in experiments using ytterbium, and potential reasons for this were presented. Previous experiments in understanding and measuring phase noise were researched, summarized, and presented. The theory of LOCSET, an excellent method of coherently combining fiber laser arrays, was studied in detail. A thorough derivation of LOCSET was provided, and a mathematical model of LOCSET was constructed and executed to examine the capability of LOCSET. Using this model, the bandwidth of LOCSET for a two element and sixteen element arrays were computed and compared, which demonstrated that LOCSET does indeed provide better control of the phase with a larger number of elements. The first analysis of LOCSET that analyzes the cross coupling of phase noise between elements was developed and presented. To examine this, a two element linear LOCSET model was examined, and equations describing the coupling of the phase noise between elements were derived. These equations were modeled, and the effect of

phase noise coupling between elements was presented. The theoretical loss of combining efficiency due to phase deviation was presented in terms of reduced Strehl ratio, which measures the intensity of the central core of the combined beam. Strehl ratio was chosen as the figure of merit to compare performance.

Phase noise data provided from the AFRL test bed was examined in detail. The rate of phase transient was analyzed for several data sets. The unique behavior of these data were studied and explained in terms of the physical configuration and design of the AFRL system. These data were compared to other research at other power levels, and it was shown that this rate increases linearly with power. This led to the conclusion that as fiber amplifiers increase in power, the rate of phase transient at the beginning of lasing will increase, thus requiring a faster phase control system when phase needs to be controlled at the beginning of the operation, which is certainly the case for military systems. Steady state phase noise data was analyzed and shown to be very dynamic. Rapid and large phase changes were evident in the data, again demonstrating the need for a fast phase control system. These changes were quantified and characterized by computing the phase structure function and compared to another experiment. It was shown that in a short time span, the AFRL amplifiers have much larger phase deviations than a laboratory-controlled environment and concluded that the industrial nature of the AFRL laboratory cooling systems contributed to these rapid changes. Indeed, the temperature changes of the industrial cooling system can be seen in the steady state phase noise data, and it was shown that the temperature changes related directly to the optical path length expansion and contraction of the silicon fiber. The phase noise power spectrum was analyzed for a full run to include start up and steady state, and that phase noise spectrum compared to spectra from start up and steady state separately. It was shown that

the frequency spectrum was dominated by the start up, again supporting the need for a robust phase control system during the initial operation of the system.

Output phase noise of the amplifiers during operation of LOCSET closed loop data was examined. This data was examined and seen to be several orders of magnitude decreased from the open loop data studied. Lastly, the open loop phase noise was inputted into the LOCSET model and compared to closed loop data. It was shown that this data was approximately an order of magnitude decreased from the open loop phase noise that was inputted into the LOCSET model and compared to closed loop phase noise. It was argued that this discrepancy was most likely due to the electronic noise of the control loop that was not taken into account in the LOCSET model. It was shown that the model correctly predicted a very steady frequency from the closed loop data with little change over the large spectrum studies.

In conclusion of this research, enough information about phase noise and the electronics needed to control that noise has been gathered to begin to make system engineering trade decisions on the scalability of these systems to higher power systems. Clearly, a stressing case for management of phase noise is during the initial operation of these systems. In order to use these systems in military operations, it would be impractical to have them continuously operating, and the threats that need to be considered for such systems occur with little warning. It was shown that a rapid phase change is present on the initial operation both at the AFRL fiber test bed and other experiments. But the rapid phase noise after steady state must also be taken into account. It was stated the integration time constant, τ , discussed in the theory of LOCSET, Chapter III, needed to be

$$\tau \gg 2\pi / |(\omega_i - \omega_j)| \text{ for all } i \text{ and } j \text{ when } i \neq j, \text{ and } \tau \ll T_{Phase_Noise} \text{ where } T_{Phase_Noise} \text{ is the}$$

period of the phase excursion that needs to be controlled for efficient coherent combination.

The typical values for the LOCSET modulation frequencies are 100-150 MHz with the

individual frequencies separated by 1-3 MHz. This gives a value of $\frac{2\pi}{|\omega_i - \omega_{i+1}|}$ to be

between 0.33 and 1 μ sec. The value of τ used in these experiments is, from Table 3.1,

0.16 μ sec which meets the first criterion. To determine the value of T_{Phase_Noise} , the phase

transient data discussed in Section 5.1 gave a value of 122 waves/sec during fiber amplifier

warm up, which gives a value of $T_{Phase_Noise} = 8m$ sec. Compare this with the implications of

Figure 5.7, where the Phase Structure Function indicates that a control over less than 1 msec

is required to maintain phase noise with $\lambda / 10$. This implies τ is properly selected or even

too small for this system. However, if the amplifiers reach higher power to even a kilowatt

and this rapid initial phase transient is indeed linear as discussed in Section 5.1 and illustrated

in Figure 5.3, then the phase transient, as predicted by the linear regression, would be on the

order of 1200 waves/sec, indicating a $T_{Phase_Noise} = 0.8m$ sec. This is still well within the

condition set forth by the LOCSET theory but is a concern as these systems scale.

Development of a high power fiber laser amplifier at a kilowatt remains a very challenging effort, and a better approach to scaling these systems may be more elements.

The limits of the modulation frequency as used in LOCSET are between 100-150 MHz, and, as shown above, a separation of 1 MHz is the maximum that is typically used. This implies a

maximum array size of 50 elements. It is beyond the scope of this paper to examine the

electronic considerations going into the selection of the frequency band and its limit for the

selection of the ω . The good news in scaling element is that the bandwidth of LOCSET

increases as does the loop gain, so the system should be more robust with more elements.

The discussion of the last two paragraphs leads to the conclusion that this paper begins to explore the engineering trade space needed to optimize a high power coherently combined fiber laser system. Scaling in power and scaling the number of elements both have their respective advantages and disadvantages. This research takes an important step toward providing the fundamental understanding to fully explore this trade space. A thorough system engineering analysis of this trade space would require a multi-discipline approach. The physics of the laser amplification process to take into account the increased phase noise from higher power amplifiers; the impact of the mechanical disturbances and the technologies that reduce this noise into these systems; and the electronic consideration on the bandwidth, integration time, modulation frequencies and electronic noise are some of the issues that need to be addressed to fully explore this trade space and make the systems engineering decisions on the proper path forward to scale high power fiber laser amplifier array systems.

Section 6.2. Suggestions for Future Work.

The work presented provides significant understanding in the phase noise characteristics of fiber laser amplifiers and, in particular, the phase noise of the AFRL fiber amplifiers and the ability of the LOCSET phase control technique to control that noise and maintain the amplifiers at the same phase. Unfortunately, the work load of the AFRL fiber laser test bed prevented several experiments from taking place that would further characterize those amplifiers' phase noise characteristics. In particular, data was not taken when the amplifiers were subjected to mechanical disturbances. A desired experiment would be to subject an amplifier to controlled and known acoustic and mechanical disturbances in order to understand the coupling of these disturbances into the phase noise of the beams. These experiments would be conducted when LOCSET is not operating in order to understand the coupling into the fiber amplifiers and also when LOCSET is operating to verify the control capabilities of LOCSET. It is extremely important to understand this coupling as these systems continue to mature into military hardware and the harsh vibration and acoustic environments in which they must operate.

The operation of LOCSET for greater number of amplifiers at high powers are additional experiments that must also be made to fully understand the capabilities of LOCSET. Although experiments at low power have verified and the theory indicates that the operation of the phase control system will improve as the number of elements increases, it remains to be verified in high power experiments. LOCSET has operated successfully for sixteen elements at low power and five elements at higher power, but the phase noise during those experiments was not measured. It is anticipated that LOCSET will be operated while controlling all or nearly all of the sixteen elements in the AFRL fiber laser test bed. The

phase noise data collected during those experiments would provide incredible insight into the ability of LOCSET to scale to high numbers of elements at high power.

Lastly, a complete and thorough theoretical analysis of phase noise would provide incredible insight into the causes of phase noise and help engineers to understand the potential problems of high power fiber laser systems as those systems develop and mature. Such analysis would take into account the noise due to mechanical disturbances, the noise from the dynamic thermal factors during the operation of the amplifiers, and the inherent noise due to the amplification process.

APPENDICES

Appendix 1. Derivation of LOCSET

From equation (34), equation (35) is derived. For an arbitrary element k , the photo current is modulated by $Sin(\omega_k t)$. Substituting equation (33) into (34)

$$S_{SSk} = \frac{1}{\tau} \int_0^{\tau} i_{PD}(t) Sin(\omega_k t) dt =$$

$$\frac{1}{\tau} \int_0^{\tau} \frac{R_{PD}}{2} \sum_{i=1}^N \sqrt{P_i} \sum_{j=1}^N \sqrt{P_j} \left(\begin{array}{l} Cos(\phi_i - \phi_j) (J_0(\beta_i) + 2 \sum_{n_i=1}^{\infty} J_{2n_i}(\beta_i) \cos(2n_i \omega_i t)) \bullet \\ (J_0(\beta_j) + 2 \sum_{n_j=1}^{\infty} J_{2n_j}(\beta_j) \cos(2n_j \omega_j t)) - \\ Sin(\phi_i - \phi_j) (2 \sum_{n_i=1}^{\infty} J_{2n_i-1}(\beta_i) \sin((2n_i - 1)\omega_i t)) \bullet \\ (J_0(\beta_j) + 2 \sum_{n_j=1}^{\infty} J_{2n_j}(\beta_j) \cos(2n_j \omega_j t)) - \\ Sin(\phi_i - \phi_j) (J_0(\beta_i) + 2 \sum_{n_i=1}^{\infty} J_{2n_i}(\beta_i) \cos(2n_i \omega_i t)) \bullet \\ (2 \sum_{n_j=1}^{\infty} J_{2n_j-1}(\beta_j) \sin((2n_j - 1)\omega_j)) + \\ (Cos(\phi_i - \phi_j) (2 \sum_{n_i=1}^{\infty} J_{2n_i-1}(\beta_i) \sin((2n_i - 1)\omega_i t)) \bullet \\ (2 \sum_{n_j=1}^{\infty} J_{2n_j-1}(\beta_j) \sin((2n_j - 1)\omega_j)) \end{array} \right) Sin(\omega_k t) dt \quad (57)$$

Evaluating the right hand side of (57), the terms within each term that multiplies a cosine or sine difference is simplified to obtain:

$$\begin{aligned}
& \frac{1}{\tau} \int_0^\tau \frac{R_{PD}}{2} \sum_{i=1}^N \sqrt{P_i} \sum_{j=1}^N \sqrt{P_j} \left(\begin{aligned}
& \text{Cos}(\phi_i - \phi_j) \left[\begin{aligned}
& (J_o(\beta_i)J_o(\beta_j) + \\
& J_o(\beta_i)2\sum_{n_j=1}^{\infty} J_{2n_j}(\beta_j) \cos(2n_j\omega_j t)) + \\
& J_o(\beta_j)2\sum_{n_i=1}^{\infty} J_{2n_i}(\beta_i) \cos(2n_i\omega_i t) + \\
& 2\sum_{n_i=1}^{\infty} J_{2n_i}(\beta_i) \cos(2n_i\omega_i t)2\sum_{n_j=1}^{\infty} J_{2n_j}(\beta_j) \cos(2n_j\omega_j t) \end{aligned} \right] - \\
& \text{Sin}(\phi_i - \phi_j) \left[\begin{aligned}
& (J_o(\beta_j)2\sum_{n_i=1}^{\infty} J_{2n_i-1}(\beta_i) \sin((2n_i - 1)\omega_i t)) + \\
& 2\sum_{n_i=1}^{\infty} J_{2n_i-1}(\beta_i) \sin((2n_i - 1)\omega_i t)2\sum_{n_j=1}^{\infty} J_{2n_j}(\beta_j) \cos(2n_j\omega_j t) \end{aligned} \right] - \\
& \text{Sin}(\phi_i - \phi_j) \left[\begin{aligned}
& J_o(\beta_i)2\sum_{n_j=1}^{\infty} J_{2n_j-1}(\beta_j) \sin((2n_j - 1)\omega_j) + \\
& 2\sum_{n_i=1}^{\infty} J_{2n_i}(\beta_i) \cos(2n_i\omega_i t)2\sum_{n_j=1}^{\infty} J_{2n_j-1}(\beta_j) \sin((2n_j - 1)\omega_j) \end{aligned} \right] + \\
& (\text{Cos}(\phi_i - \phi_j) \left[\begin{aligned}
& 2\sum_{n_i=1}^{\infty} J_{2n_i-1}(\beta_i) \sin((2n_i - 1)\omega_i t)2\sum_{n_j=1}^{\infty} J_{2n_j-1}(\beta_j) \sin((2n_j - 1)\omega_j) \end{aligned} \right]) \end{aligned} \right) \text{Sin}(\omega_k t) dt
\end{aligned}
\end{aligned}
\tag{58}$$

The $\text{Sin}(\omega_k t)dt$ is multiplied within each of these nine terms within the cosine or sine differences to obtain

$$\frac{1}{\tau} \int_0^\tau \frac{R_{PD}}{2} \sum_{i=1}^N \sqrt{P_i} \sum_{j=1}^N \sqrt{P_j} \left(\begin{array}{l} \left[\begin{array}{l} (J_o(\beta_i)J_o(\beta_j)Sin(\omega_k t) + \\ J_o(\beta_i)2\sum_{n_j=1}^{\infty} J_{2n_j}(\beta_j) \cos(2n_j\omega_j t))Sin(\omega_k t) + \\ J_o(\beta_j)2\sum_{n_i=1}^{\infty} J_{2n_i}(\beta_i) \cos(2n_i\omega_i t))Sin(\omega_k t) + \\ 2\sum_{n_i=1}^{\infty} J_{2n_i}(\beta_i)2\sum_{n_j=1}^{\infty} J_{2n_j}(\beta_j) \cos(2n_i\omega_i t) \cos(2n_j\omega_j t))Sin(\omega_k t) \end{array} \right] - \\ \left[\begin{array}{l} (J_o(\beta_j)2\sum_{n_i=1}^{\infty} J_{2n_i-1}(\beta_i) \sin((2n_i-1)\omega_i t))Sin(\omega_k t) + \\ 2\sum_{n_i=1}^{\infty} J_{2n_i-1}(\beta_i)2\sum_{n_j=1}^{\infty} J_{2n_j}(\beta_j) \sin((2n_i-1)\omega_i t) \cos(2n_j\omega_j t))Sin(\omega_k t) \end{array} \right] - \\ \left[\begin{array}{l} J_o(\beta_i)2\sum_{n_j=1}^{\infty} J_{2n_j-1}(\beta_j) \sin((2n_j-1)\omega_j)Sin(\omega_k t) + \\ 2\sum_{n_i=1}^{\infty} J_{2n_i}(\beta_i)2\sum_{n_j=1}^{\infty} J_{2n_j-1}(\beta_j) \cos(2n_i\omega_i t) \sin((2n_j-1)\omega_j)Sin(\omega_k t) \end{array} \right] + \\ (Cos(\phi_i - \phi_j) \left[\begin{array}{l} 2\sum_{n_i=1}^{\infty} J_{2n_i-1}(\beta_i)2\sum_{n_j=1}^{\infty} J_{2n_j-1}(\beta_j) \sin((2n_i-1)\omega_i t) \sin((2n_j-1)\omega_j)Sin(\omega_k t) \end{array} \right] \end{array} \right) dt$$

The integral is then distributed within each term that contains a dependence upon time.

$$\begin{aligned}
& \frac{R_{PD}}{2\tau} \sum_{i=1}^N \sqrt{P_i} \sum_{j=1}^N \sqrt{P_j} \left[\begin{aligned}
& \text{Cos}(\phi_i - \phi_j) \left[\begin{aligned}
& (J_o(\beta_i)J_o(\beta_j) \int_0^\tau \text{Sin}(\omega_k t) dt + \\
& J_o(\beta_i)2 \sum_{n=1}^\infty J_{2n}(\beta_j) \int_0^\tau \cos(2n\omega_j t) \text{Sin}(\omega_k t) dt + \\
& J_o(\beta_j)2 \sum_{n=1}^\infty J_{2n}(\beta_i) \int_0^\tau \cos(2n\omega_i t) \text{Sin}(\omega_k t) dt + \\
& 2 \sum_{n=1}^\infty J_{2n}(\beta_i) 2 \sum_{n=1}^\infty J_{2n}(\beta_j) \int_0^\tau \cos(2n\omega_i t) \cos(2n\omega_j t) \text{Sin}(\omega_k t) dt \end{aligned} \right] - \\
& \text{Sin}(\phi_i - \phi_j) \left[\begin{aligned}
& (J_o(\beta_j)2 \sum_{n=1}^\infty J_{2n-1}(\beta_i) \int_0^\tau \sin((2n-1)\omega_i t) \text{Sin}(\omega_k t) dt + \\
& 2 \sum_{n=1}^\infty J_{2n-1}(\beta_i) 2 \sum_{n=1}^\infty J_{2n}(\beta_j) \int_0^\tau \sin((2n-1)\omega_i t) \cos(2n\omega_j t) \text{Sin}(\omega_k t) dt \end{aligned} \right] - \\
& \text{Sin}(\phi_i - \phi_j) \left[\begin{aligned}
& J_o(\beta_i)2 \sum_{n=1}^\infty J_{2n-1}(\beta_j) \int_0^\tau \sin((2n-1)\omega_j) \text{Sin}(\omega_k t) dt + \\
& 2 \sum_{n=1}^\infty J_{2n}(\beta_i) 2 \sum_{n=1}^\infty J_{2n-1}(\beta_j) \int_0^\tau \cos(2n\omega_i t) \sin((2n-1)\omega_j) \text{Sin}(\omega_k t) dt \end{aligned} \right] + \\
& (\text{Cos}(\phi_i - \phi_j) \left[2 \sum_{n=1}^\infty J_{2n-1}(\beta_i) 2 \sum_{n=1}^\infty J_{2n-1}(\beta_j) \int_0^\tau \sin((2n-1)\omega_i t) \sin((2n-1)\omega_j) \text{Sin}(\omega_k t) dt \right]
\end{aligned} \right]
\end{aligned}
\tag{59}$$

Using the trigonometric identity for the product of cosines and sines, the expression is then written as:

The integration of each term can now be completed to obtain:

$$\frac{R_{PD}}{2\tau} \sum_{i=1}^N \sqrt{P_i} \sum_{j=1}^N \sqrt{P_j}$$

$$\begin{aligned}
& \left[\begin{aligned}
& (J_o(\beta_i)J_o(\beta_j)) \left(\frac{1 - \cos(\omega_k \tau)}{\omega_k} \right) + \\
& J_o(\beta_i)2 \sum_{n_j=1}^{\infty} J_{2n_j}(\beta_j) \frac{1}{2} \left(\frac{1 - \cos(2n_j \omega_j \tau + \omega_k \tau)}{2n_j \omega_j + \omega_k} - \frac{1 - \cos(2n_j \omega_j \tau - \omega_k \tau)}{2n_j \omega_j - \omega_k} \right) + \\
& J_o(\beta_j)2 \sum_{n_i=1}^{\infty} J_{2n_i}(\beta_i) \frac{1}{2} \left(\frac{1 - \cos(2n_i \omega_i \tau + \omega_k \tau)}{2n_i \omega_i + \omega_k} - \frac{1 - \cos(2n_i \omega_i \tau - \omega_k \tau)}{2n_i \omega_i - \omega_k} \right) + \\
& \left. \begin{aligned}
& \left(\frac{1 - \cos(2n_i \omega_i \tau + 2n_j \omega_j \tau + \omega_k \tau)}{2n_i \omega_i + 2n_j \omega_j + \omega_k} - \right. \\
& \left. \frac{1 - \cos(2n_i \omega_i \tau + 2n_j \omega_j \tau - \omega_k \tau)}{2n_i \omega_i + 2n_j \omega_j - \omega_k} \right) + \\
& 2 \sum_{n_i=1}^{\infty} J_{2n_i}(\beta_i)2 \sum_{n_j=1}^{\infty} J_{2n_j}(\beta_j) \frac{1}{4} \left(\frac{1 - \cos(2n_i \omega_i \tau - 2n_j \omega_j \tau + \omega_k \tau)}{2n_i \omega_i - 2n_j \omega_j + \omega_k} - \right. \\
& \left. \frac{1 - \cos(2n_i \omega_i \tau - 2n_j \omega_j \tau - \omega_k \tau)}{2n_i \omega_i - 2n_j \omega_j - \omega_k} \right) \right] - \\
& \left[\begin{aligned}
& (J_o(\beta_j)2 \sum_{n_i=1}^{\infty} J_{2n_i-1}(\beta_i) \frac{1}{2} \left(\frac{\sin((2n_i - 1)\omega_i \tau - \omega_k \tau)}{(2n_i - 1)\omega_i - \omega_k} - \frac{\sin((2n_i - 1)\omega_i \tau + \omega_k \tau)}{(2n_i - 1)\omega_i + \omega_k} \right) + \\
& \left. \begin{aligned}
& \left(\frac{\sin((2n_i - 1)\omega_i \tau + 2n_j \omega_j \tau - \omega_k \tau)}{(2n_i - 1)\omega_i + 2n_j \omega_j - \omega_k} - \right. \\
& \left. \frac{\sin((2n_i - 1)\omega_i \tau + 2n_j \omega_j \tau + \omega_k \tau)}{(2n_i - 1)\omega_i + 2n_j \omega_j + \omega_k} \right) + \\
& 2 \sum_{n_i=1}^{\infty} J_{2n_i-1}(\beta_i)2 \sum_{n_j=1}^{\infty} J_{2n_j}(\beta_j) \frac{1}{4} \left(\frac{\sin((2n_i - 1)\omega_i \tau - 2n_j \omega_j \tau - \omega_k \tau)}{(2n_i - 1)\omega_i - 2n_j \omega_j - \omega_k} - \right. \\
& \left. \frac{\sin((2n_i - 1)\omega_i \tau - 2n_j \omega_j \tau + \omega_k \tau)}{(2n_i - 1)\omega_i - 2n_j \omega_j + \omega_k} \right) \right] - \\
& \left[\begin{aligned}
& J_o(\beta_i)2 \sum_{n_j=1}^{\infty} J_{2n_j-1}(\beta_j) \frac{1}{2} \left(\frac{\sin((2n_j - 1)\omega_j \tau - \omega_k \tau)}{(2n_j - 1)\omega_j - \omega_k} - \frac{\sin((2n_j - 1)\omega_j \tau + \omega_k \tau)}{(2n_j - 1)\omega_j + \omega_k} \right) + \\
& \left. \begin{aligned}
& \left(\frac{\sin(2n_i \omega_i \tau + (2n_j - 1)\omega_j \tau - \omega_k \tau)}{2n_i \omega_i + (2n_j - 1)\omega_j - \omega_k} - \right. \\
& \left. \frac{\sin(2n_i \omega_i \tau + (2n_j - 1)\omega_j \tau + \omega_k \tau)}{2n_i \omega_i + (2n_j - 1)\omega_j + \omega_k} \right) - \\
& 2 \sum_{n_i=1}^{\infty} J_{2n_i}(\beta_i)2 \sum_{n_j=1}^{\infty} J_{2n_j-1}(\beta_j) \frac{1}{4} \left(\frac{\sin(2n_i \omega_i \tau - (2n_j - 1)\omega_j \tau - \omega_k \tau)}{2n_i \omega_i - (2n_j - 1)\omega_j - \omega_k} + \right. \\
& \left. \frac{\sin(2n_i \omega_i \tau - (2n_j - 1)\omega_j \tau + \omega_k \tau)}{2n_i \omega_i - (2n_j - 1)\omega_j + \omega_k} \right) \right] + \\
& \left[\begin{aligned}
& (Cos(\phi_i - \phi_j)) 2 \sum_{n_i=1}^{\infty} J_{2n_i-1}(\beta_i)2 \sum_{n_j=1}^{\infty} J_{2n_j-1}(\beta_j) \frac{1}{4} \left(\frac{1 - \cos((2n_i - 1)\omega_i \tau - (2n_j - 1)\omega_j \tau + \omega_k \tau)}{(2n_i - 1)\omega_i - (2n_j - 1)\omega_j + \omega_k} - \right. \\
& \left. \frac{1 - \cos((2n_i - 1)\omega_i \tau - (2n_j - 1)\omega_j \tau - \omega_k \tau)}{(2n_i - 1)\omega_i - (2n_j - 1)\omega_j - \omega_k} \right) + \\
& \left. \left(\frac{1 - \cos((2n_i - 1)\omega_i \tau + (2n_j - 1)\omega_j \tau + \omega_k \tau)}{(2n_i - 1)\omega_i + (2n_j - 1)\omega_j + \omega_k} - \right. \right. \\
& \left. \left. \frac{1 - \cos((2n_i - 1)\omega_i \tau + (2n_j - 1)\omega_j \tau - \omega_k \tau)}{(2n_i - 1)\omega_i + (2n_j - 1)\omega_j - \omega_k} \right) \right] +
\end{aligned}
\end{aligned}
\end{aligned}$$

Notice in each term an RF frequency term ω will appear in the denominator for all n_i and n_j , except for the two that are highlighted in red, and in those terms only when $n_i = 1$ and $\omega_i = \omega_k$ or $n_j = 1$ and $\omega_j = \omega_k$ do the RF frequency terms cancel. In all cases that have an RF frequency term in the denominator, the value of those terms becomes negligible and can be neglected. In the cases when the RF frequency term cancels, the denominator is equal to zero, and the integral must be reevaluated separately. Consequently, every term can be removed from equation (59), except those two terms where the RF frequency terms cancel in the denominator and the integrals are reevaluated.

$$\frac{R_{PD}}{2\tau} \sum_{i=1}^N \sqrt{P_i} \sum_{j=1}^N \sqrt{P_j} \left(\begin{array}{l} -\text{Sin}(\phi_i - \phi_j) \left[(J_o(\beta_j) 2 \sum_{n=1}^{\infty} J_{2n-1}(\beta_i) \int_0^{\tau} \sin((2n-1)\omega_i t) \text{Sin}(\omega_k t) dt) \right] - \\ \text{Sin}(\phi_i - \phi_j) \left[J_o(\beta_i) 2 \sum_{n=1}^{\infty} J_{2n-1}(\beta_j) \int_0^{\tau} \sin((2n-1)\omega_j) \text{Sin}(\omega_k t) dt \right] \end{array} \right) \quad (61)$$

As discussed, all terms where $i \neq k$ can be neglected and the summation over i are dropped. Also, the second term can be dropped when $i \neq j$ because of the RF frequency terms and can be dropped when $i = j$ because $\sin(\phi_i - \phi_j)$ goes to zero. Equation (61) can now be written as

$$\frac{R_{PD}}{2\tau} \sqrt{P_i} \sum_{j=1}^N \sqrt{P_j} \left(-\text{Sin}(\phi_i - \phi_j) \left[(J_o(\beta_j) 2 \sum_{n_i=1}^{\infty} J_{2n_i-1}(\beta_i) \int_0^{\tau} \sin((2n_i-1)\omega_i t) \text{Sin}(\omega_i t) dt) \right] \right) \quad (62)$$

Looking specifically at the case where $n_i = 1$

$$\frac{R_{PD}}{2\tau} \sqrt{P_i} \sum_{j=1}^N \sqrt{P_j} \left(-\text{Sin}(\phi_i - \phi_j) \left[(J_o(\beta_j) 2 \left(J_1(\beta_i) \int_0^\tau \sin^2(\omega_i t) dt + \sum_{n_i=1}^{\infty} J_{2n_i-1}(\beta_i) \int_0^\tau \sin((2n_i - 1)\omega_i t) \text{Sin}(\omega_i t) dt \right) \right] \right) \right) \quad (63)$$

Performing the integration equation (63) becomes

$$\frac{R_{PD}}{2\tau} \sqrt{P_i} \sum_{j=1}^N \sqrt{P_j} \left(-\text{Sin}(\phi_i - \phi_j) \left[(J_o(\beta_j) 2 \left(J_1(\beta_i) \left(\frac{\tau}{2} - \frac{\sin(2\omega_i \tau)}{4\omega_i} \right) + \sum_{n_i=2}^{\infty} J_{2n_i-1}(\beta_i) \left(\frac{1}{2} \frac{\sin((2n_i - 2)\omega_i \tau)}{(2n_i - 2)\omega_i} - \frac{\sin(2n_i \omega_i \tau)}{2n_i \omega_i} \right) \right) \right] \right) \right) \quad (64)$$

The second and third terms in the last brackets will also be neglected because of the RF frequency terms in the denominator, so equation (64) becomes

$$\frac{R_{PD}}{2\tau} \sqrt{P_i} \sum_{j=1}^N \sqrt{P_j} \left(-\text{Sin}(\phi_i - \phi_j) \left[(J_o(\beta_j) 2 \left(J_1(\beta_i) \left(\frac{\tau}{2} \right) \right) \right] \right) \quad (65)$$

Simplifying,

$$\frac{R_{PD}}{2} \sqrt{P_i} (J_1(\beta_i)) \sum_{j=1}^N \sqrt{P_j} (J_o(\beta_j)) \text{Sin}(\phi_j - \phi_i) \quad (66)$$

Remembering that this is the right hand side of equation (57), the phase control signal for the i th element in a self synchronous LOCSET array of N elements is given by

$$S_{SSi} = \frac{R_{PD}}{2} \sqrt{P_i} (J_1(\beta_i)) \sum_{j=1}^N \sqrt{P_j} (J_o(\beta_j)) \text{Sin}(\phi_j - \phi_i). \quad (67)$$

Appendix 2. LOCSET Electronic Schematic

Appendix 3. Mathcad Programs

Generic LOCSET Model-16 element example

LOCSET Model-2 elements actual data

Two element analysis

This program is a N element LOCSET model where the input phase noise data for each element have the same number of data points but frequencies values are not necessarily equal, Power per element are not necessarily equal, and β are not necessarily equal

Electronic_Constants :=



Read the input data for the run from an Excel file "Electronic Constants".

$$R_{pd} := \text{Electronic_Constants}_1 \cdot \frac{\text{V}}{\text{W}}$$

$$R_{pd} = 5 \frac{1}{\text{A}}$$

$$A_e := \text{Electronic_Constants}_2$$

$$A_e = 3.15 \times 10^4$$

$$K_{pm} := \text{Electronic_Constants}_3 \cdot \frac{\text{rad}}{\text{V}}$$

$$K_{pm} = 1.26 \frac{\text{s}^3 \text{A}}{\text{kg m}^2}$$

$$\tau := \text{Electronic_Constants}_4 \cdot \text{s} \cdot 10^{-6}$$

$$\tau = 1.6 \times 10^{-7} \text{ s}$$

$$\text{Nelements} := \text{Electronic_Constants}_5$$

$$\text{Nelements} = 16$$

$$\text{range} := 1.. \text{Nelements}$$

Define the number of amplifier elements.

$$\beta_{\text{range}} := \text{Electronic_Constants}_{6+\text{range}} \cdot \text{rad}$$

Power_Data :=



Read the power for each element that reaches the detector.

$$\text{POWER}_{\text{range}} := \text{Power_Data}_{\text{range}} \cdot \text{W}$$

Define the power for each element.

PN :=



Read in the open loop phase noise data for element 1.

Define range variable for number of data points for each element.

$$\text{RANGEF} := 1.. \text{Electronic_Constants}_6$$

A-1

$$\text{RANGEG} := 2.. \text{Electronic_Constants}_6$$

RANGEG is defined to avoid the zero frequency.

$$\text{BESS}0_{\text{range}} := \text{J0}(\beta_{\text{range}})$$

Calculates the value of the zero and first order Bessel functions of β_i .

$$\text{BESS}1_{\text{range}} := \text{J1}(\beta_{\text{range}})$$

range1 := 1.. Nelements

$$\text{KVALUE}_{\text{range}, \text{range1}} := \text{Rp}d \cdot \sqrt{\text{POWER}_{\text{range}} \cdot \text{BESS}1_{\text{range}}} \cdot \sqrt{\text{POWER}_{\text{range1}} \cdot \text{BESS}0_{\text{range1}}}$$

Calculate Kij for all i and j.

$$\text{Ksum}_{\text{range}} := \begin{cases} \text{sum} \leftarrow 0 \\ \text{for } j \in 1.. \text{Nelements} \\ \quad \text{sum} \leftarrow \text{sum} + \text{KVALUE}_{\text{range}, j} \\ \text{sum} \leftarrow \text{sum} - \text{KVALUE}_{\text{range}, \text{range}} \end{cases}$$

Calculate the ith summation over j for each Kij.

$$\text{BW}_{\text{range}} := \text{Ae} \cdot \text{Kpm} \cdot \frac{\text{Ksum}_{\text{range}} \cdot \text{rad}}{\tau}$$

Calculate the control bandwidth for each element in radians/sec.

$$\Delta\phi_{\text{RANGEF}, \text{range}} := (\text{PN})_{\text{RANGEF}, 2 \cdot \text{range} - 1} \cdot \text{rad}$$

$\Delta\phi$ is the open loop phase noise in radians.

$$BW_{hzt} := \frac{BW}{2 \cdot \pi}$$

$$BW_{hzt}_1 = 2.212 \times 10^6 \text{ Hz}$$

Compute the control bandwidth in Hertz.

$$Frequencies_{RANGEF, range} := PN_{RANGEF, 2range} \cdot \frac{1}{sec}$$

Define the frequency data for each element.

$$SVAR_{RANGEF, range} := 2i \cdot \pi \cdot Frequencies_{RANGEF, range} \cdot rad$$

A-2

Define the LaPlace variable for each element corresponding to the frequencies.

Model closed loop phase noise $\delta\phi$ for each element.

$$\delta\phi_{RANGEF, range} := \frac{\left[(SVAR_{RANGEF, range}) \cdot \Delta\phi_{RANGEF, range} \right]}{SVAR_{RANGEF, range} + Ae \cdot \frac{K_{pm} \cdot K_{sum}}{\tau}_{range}}$$

$$\delta\phi_{MAG}_{RANGEF, range} := \sqrt{\text{Re}(\delta\phi_{RANGEF, range})^2 + \text{Im}(\delta\phi_{RANGEF, range})^2}$$

Calculate magnitude of closed loop phase noise for each element.

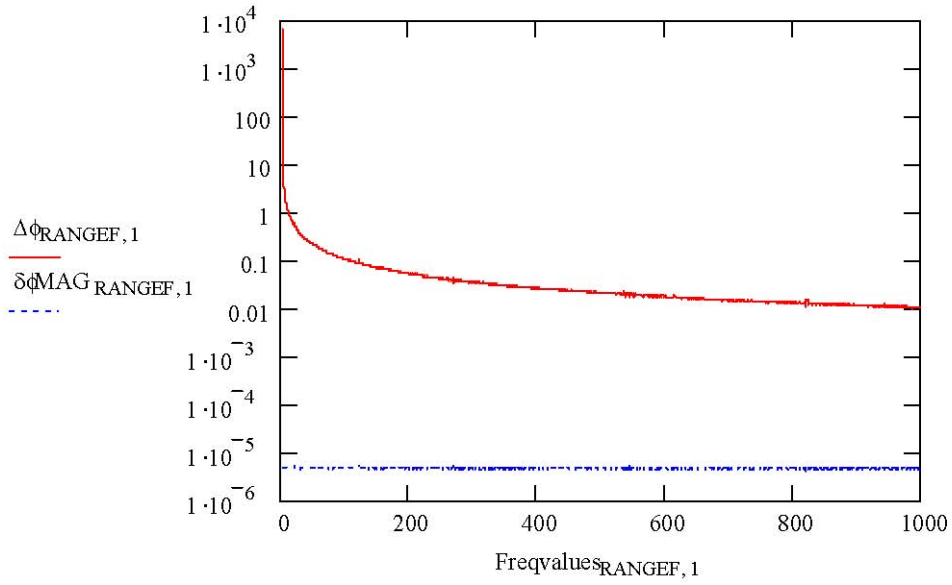
$$BW_{Gain}_{RANGEG, range} := \frac{1}{\left[\frac{SVAR_{RANGEG, range}}{(SVAR_{RANGEG, range} + BW_{range})} \right]}$$

Calculate loop gain for each element.

$$BW_{MAG}_{RANGEG, range} := \left(\sqrt{\text{Re}(BW_{Gain}_{RANGEG, range})^2 + \text{Im}(BW_{Gain}_{RANGEG, range})^2} \right)$$

Calculate magnitude of loop gain for each element.

A-3

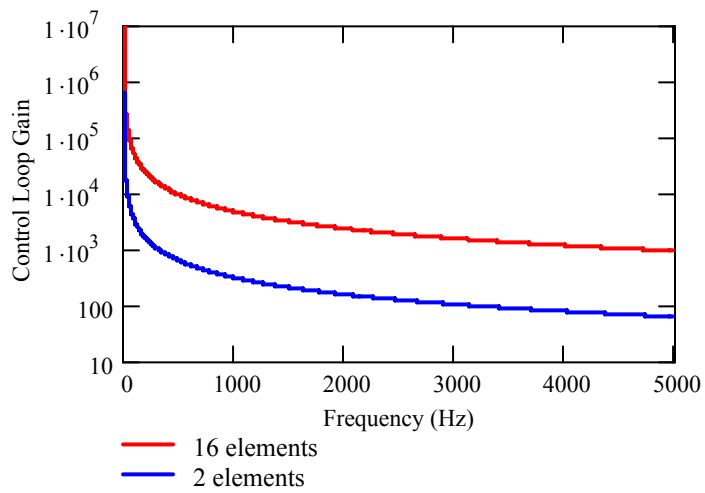


$\delta\phi_{\text{MAG}}$



BWGMAG

Compare bandwidths for 2 and 16 elements.



BWGMAG2:=



This program is a 2 element locset model where the input phase noise data for each element have different frequencies values and the number of data points are different. Power per element is equal and β is equal.

Read the input data for the run from an Excel file "Electronic Constants".

Electronic_Constants :=



$$Rpd := \text{Electronic_Constants}_1 \cdot \frac{V}{W}$$

$$Rpd = 1.883 \times 10^3 \frac{1}{A}$$

$$Ae := \text{Electronic_Constants}_2$$

$$Ae = 177.5$$

$$Kpm := \text{Electronic_Constants}_3 \cdot \frac{\text{rad}}{V}$$

$$Kpm = 1.26 \frac{s^3 A}{kg m^2}$$

$$\tau := \text{Electronic_Constants}_4 \cdot s \cdot 10^{-6}$$

$$\tau = 1.6 \times 10^{-7} s$$

$$\text{Nelements} := \text{Electronic_Constants}_5$$

$$\text{Nelements} = 2$$

$$\text{range} := 1.. \text{Nelements}$$

Define the number of amplifier elements.

$$\beta_{\text{range}} := \text{Electronic_Constants}_{5+\text{range}} \cdot \text{rad}$$

$$\text{POWER}_{\text{range}} := 15 \cdot 10^{-6} \cdot W$$

Define the power for each element that reaches the detector.

PN1 :=



Read in the open loop phase noise data for element 1. Phase noise is in column 1, frequency in column 2.

Defines range variable for number of data points for element 1.

RANGEF1:= 1..14067

PN2 :=



Read in the open loop phase noise data for element 2.

Defines range variable for number of data points for element 2.

RANGEF2:= 1..13658

RANGEG1:= 2..14067

RANGEG 1 and 2 are defined to avoid the zero frequency.

RANGEG2:= 2..13658

BESS0_{range} := J0(β_{range})

Calculates the value of the zero and first order Bessel functions of β_i .

BESS1_{range} := J1(β_{range})

range1 := 1..Nelements

$KVALUE_{range, range1} := Rpd \cdot \sqrt{POWER_{range}} \cdot BESS1_{range} \cdot \sqrt{POWER_{range1}} \cdot BESS0_{range1}$

Calculate Kij for all i and j.

$$Ksum_{range} := \begin{cases} \text{sum} \leftarrow 0 \\ \text{for } j \in 1..Nelements \\ \quad \text{sum} \leftarrow \text{sum} + KVALUE_{range, j} \\ \quad \text{sum} \leftarrow \text{sum} - KVALUE_{range, range} \end{cases}$$

Calculate the ith summation over j for each Kij.

Calculates the control bandwidth for each element in radians/sec.

$$BW_{\text{range}} := Ae \cdot K_{\text{pm}} \cdot \frac{K_{\text{sum}} \cdot \text{range} \cdot \text{rad}}{\tau}$$

$$BW = \begin{pmatrix} 1.967 \times 10^6 \\ 1.967 \times 10^6 \end{pmatrix} \text{Hz}$$

$$\Delta\phi_{\text{RANGEF1},1} := \text{PN1}_{\text{RANGEF1},1} \cdot \text{rad}$$

$\Delta\phi$ is the open loop phase noise in radians. Column 1 is element 1, column 2 is element 2.

$$\Delta\phi_{\text{RANGEF2},2} := \text{PN2}_{\text{RANGEF2},1} \cdot \text{rad}$$

Compute the control bandwidth in Hertz.

$$BW_{\text{hzt}} := \frac{BW}{2 \cdot \pi}$$

$$BW_{\text{hzt}} = \begin{pmatrix} 3.13 \times 10^5 \\ 3.13 \times 10^5 \end{pmatrix} \text{Hz}$$

$$\text{SVAR}_{\text{RANGEF1},1} := 2i\pi \cdot (\text{PN1}_{\text{RANGEF1},2}) \cdot \frac{\text{rad}}{\text{sec}}$$

Define the LaPlace variable for each element. Column 1 is element 1, column 2 is element 2.

$$\text{SVAR}_{\text{RANGEF2},2} := 2i\pi \cdot (\text{PN2}_{\text{RANGEF2},2}) \cdot \frac{\text{rad}}{\text{sec}}$$

Model closed loop phase noise $\delta\phi$ for each element.

$$\delta\phi_{\text{RANGEF1},1} := \frac{\left[(\text{SVAR}_{\text{RANGEF1},1}) \cdot \Delta\phi_{\text{RANGEF1},1} \right]}{\text{SVAR}_{\text{RANGEF1},1} + Ae \cdot \frac{K_{\text{pm}} \cdot K_{\text{sum}}}{\tau}}$$

$$\delta\phi_{\text{RANGEF2},2} := \frac{\left[(\text{SVAR}_{\text{RANGEF2},2}) \cdot \Delta\phi_{\text{RANGEF2},2} \right]}{\text{SVAR}_{\text{RANGEF2},2} + Ae \cdot \frac{K_{\text{pm}} \cdot K_{\text{sum}}}{\tau}}$$

Calculate magnitude of closed loop phase noise for each element.

$$\delta\phi_{\text{MAGRANGEF1},1} := \sqrt{\text{Re}(\delta\phi_{\text{RANGEF1},1})^2 + \text{Im}(\delta\phi_{\text{RANGEF1},1})^2}$$

$$\delta\phi_{\text{MAG}_{\text{RANGE}2,2}} := \sqrt{\text{Re}(\delta\phi_{\text{RANGE}2,2})^2 + \text{Im}(\delta\phi_{\text{RANGE}2,2})^2}$$

$$\text{BWGain}_{\text{RANGE}1,1} := \frac{1}{\left[\frac{\text{SVAR}_{\text{RANGE}1,1}}{(\text{SVAR}_{\text{RANGE}1,1} + \text{BW}_1)} \right]}$$

Calculate loop gain for each element.

$$\text{BWGain}_{\text{RANGE}2,2} := \frac{1}{\left(\frac{\text{SVAR}_{\text{RANGE}2,2}}{\text{SVAR}_{\text{RANGE}2,2} + \text{BW}_2} \right)}$$

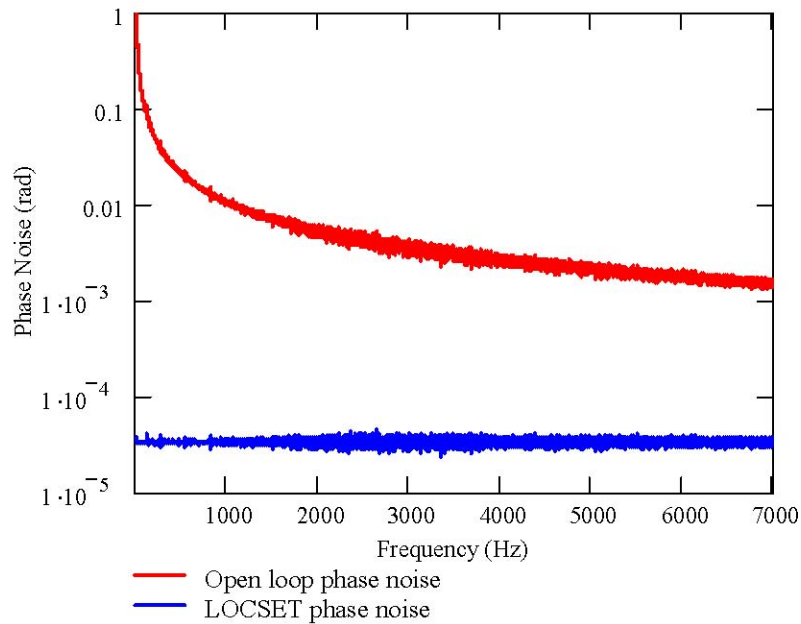
$$\text{BWGMAG}_{\text{RANGE}1,1} := \left(\sqrt{\text{Re}(\text{BWGain}_{\text{RANGE}1,1})^2 + \text{Im}(\text{BWGain}_{\text{RANGE}1,1})^2} \right)$$

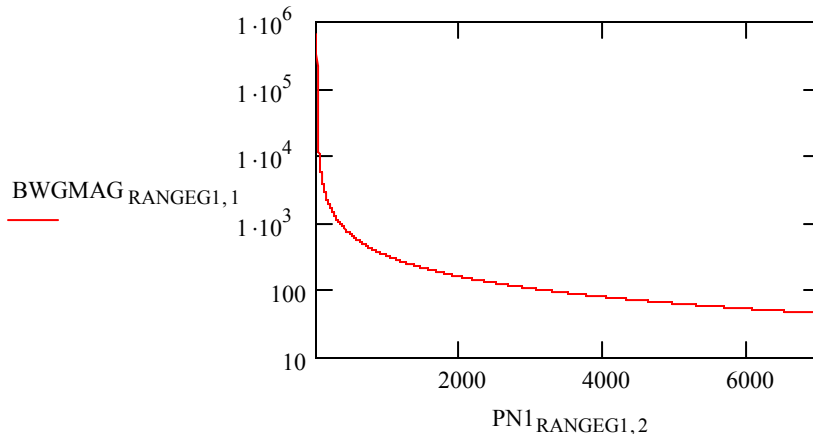
$$\text{BWGMAG}_{\text{RANGE}1,2} := \left(\sqrt{\text{Re}(\text{BWGain}_{\text{RANGE}1,2})^2 + \text{Im}(\text{BWGain}_{\text{RANGE}1,2})^2} \right)$$

Calculate magnitude of loop gain for each element.



BWGMAG





Read the closed loop phase noise data computed from the closed loop intensity.

$\delta\phi$ data :=

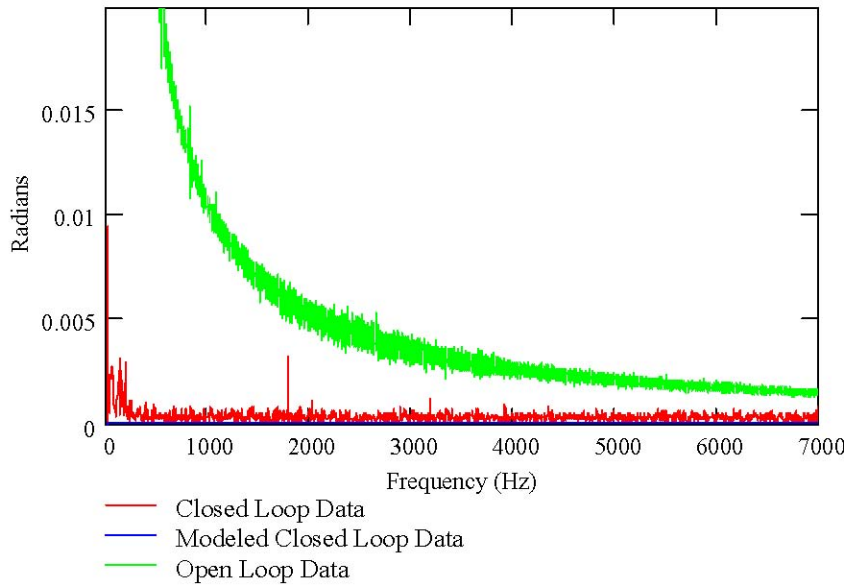


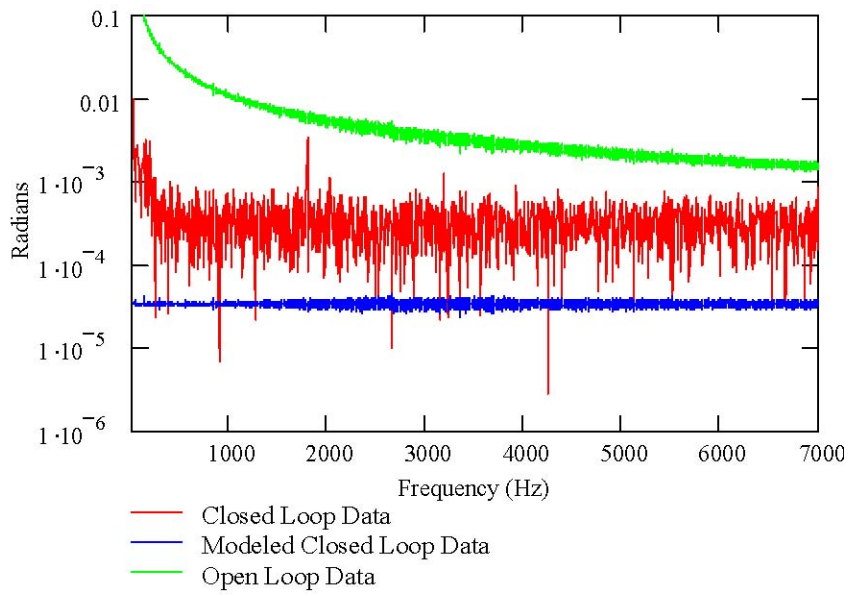
..\Closed loop F data\01_Phivsf_

RANGE3:= 1..1350

Define the number of elements in $\delta\phi$ data.

Plot shows the closed loop phase noise data (red), modeled closed loop phase noise data (green) and open loop phase noise data (blue) vs.frequency. Lower plot is log scale.





This is the two element LOCSET model as discussed in Sections 2.5 and 5.5.

$$\text{RPD} := 5.9\%$$

$$\text{KPM} := 1.2\%$$

Define the electronic constants.

$$P := .000015 \text{ W}$$

$$\text{AE} := 3.150\%$$

$$\tau := 0.00000016$$

$$\text{KSUM} := \text{RPD} \cdot \sqrt{P} \cdot \text{J1}(0.1) \cdot \sqrt{P} \cdot \text{J0}(0.1)$$

$$\text{BW} := \text{AE} \cdot \text{KPM} \cdot \frac{\text{KSUM}}{\tau}$$

$$\text{KSUM} = 4.431 \times 10^{-6} \text{ W}$$

Case 1

$$a1 := 10\%$$

$$\text{BW} = 109.913 \text{ W}$$

Define the frequencies used.

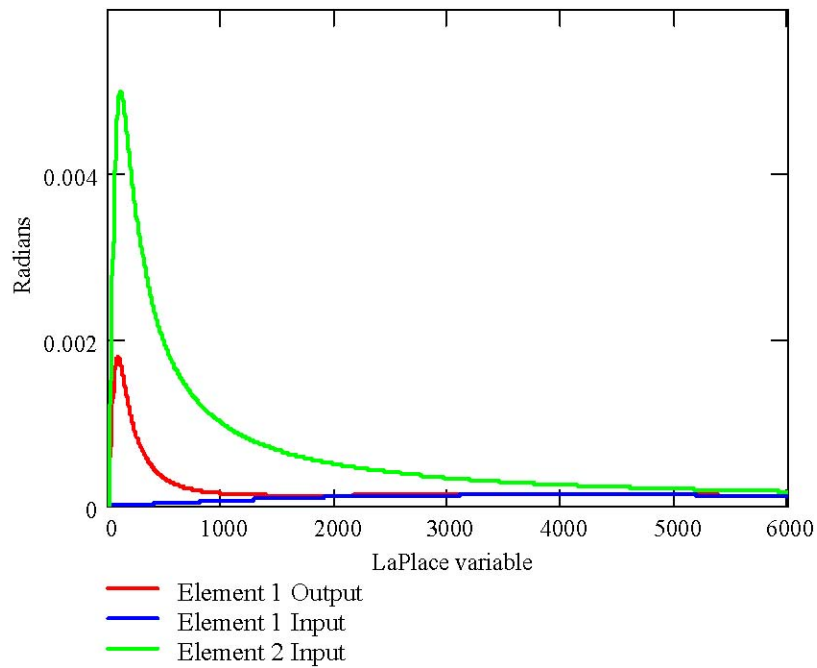
$$a2 := 400\%$$

Case 1

$$\Delta\phi1(\text{svar}) := \frac{\text{svar}}{\text{svar}^2 + a2^2}$$

$$\Delta\phi2(\text{svar}) := \frac{\text{svar}}{\text{svar}^2 + (a1)^2}$$

$$\delta\phi(\text{svar}) := \frac{[(\text{BW} + \text{svar}) \cdot \Delta\phi1(\text{svar}) + \Delta\phi2(\text{svar}) \cdot \text{BW}]}{2 \cdot \text{BW} + \text{svar}}$$



Case 2

$$BW := AE \cdot KPM \cdot \frac{KSUM}{\tau}$$

$$a1 := 100$$

$$BW = 109.913W$$

Define the frequencies used.

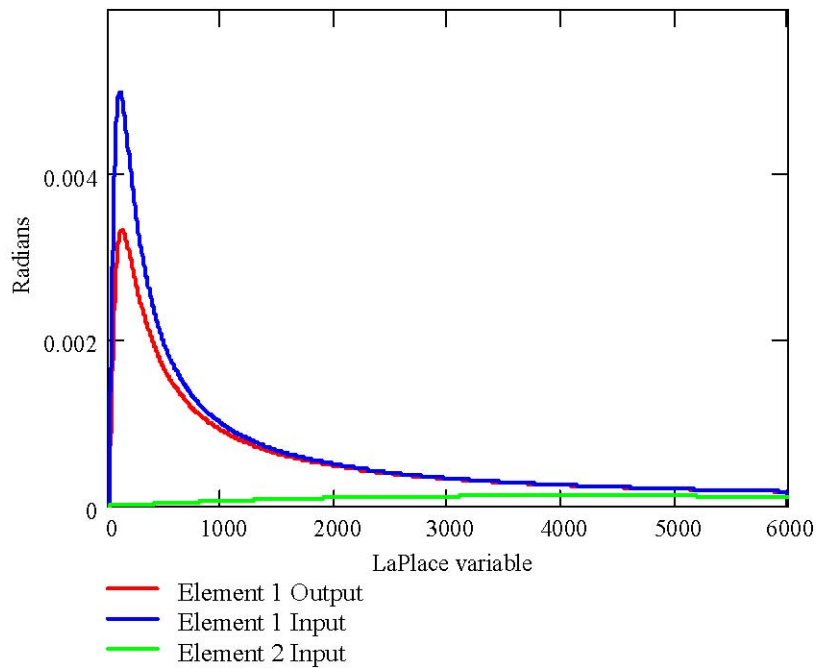
$$a2 := 4000$$

Case 2

$$\Delta\phi1(svar) := \frac{svar}{svar^2 + a1^2}$$

$$\Delta\phi2(svar) := \frac{svar}{svar^2 + (a2)^2}$$

$$\delta\phi(svar) := \frac{[(BW + svar) \cdot \Delta\phi1(svar) + \Delta\phi2(svar) \cdot BW]}{2 \cdot BW + svar}$$



Case 3

$$BW := AE \cdot KPM \cdot \frac{KSUM}{\tau}$$

$$a1 := 100$$

$$BW = 109.913W$$

Define the frequencies used.

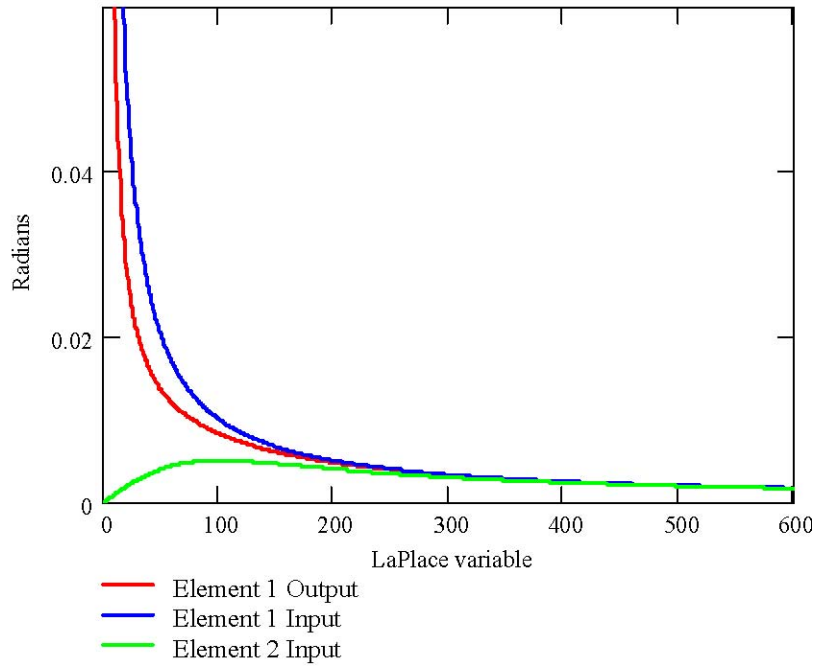
$$a2 := 4000$$

Case 3

$$\Delta\phi1(svar) := \frac{1}{svar}$$

$$\Delta\phi2(svar) := \frac{svar}{svar^2 + (a1)^2}$$

$$\delta\phi(svar) := \frac{[(BW + svar) \cdot \Delta\phi1(svar) + \Delta\phi2(svar) \cdot BW]}{2 \cdot BW + svar}$$



Case 4

$$BW := AE \cdot KPM \cdot \frac{KSUM}{\tau}$$

$$a1 := 100$$

$$BW = 109.913W$$

Define the frequencies used.

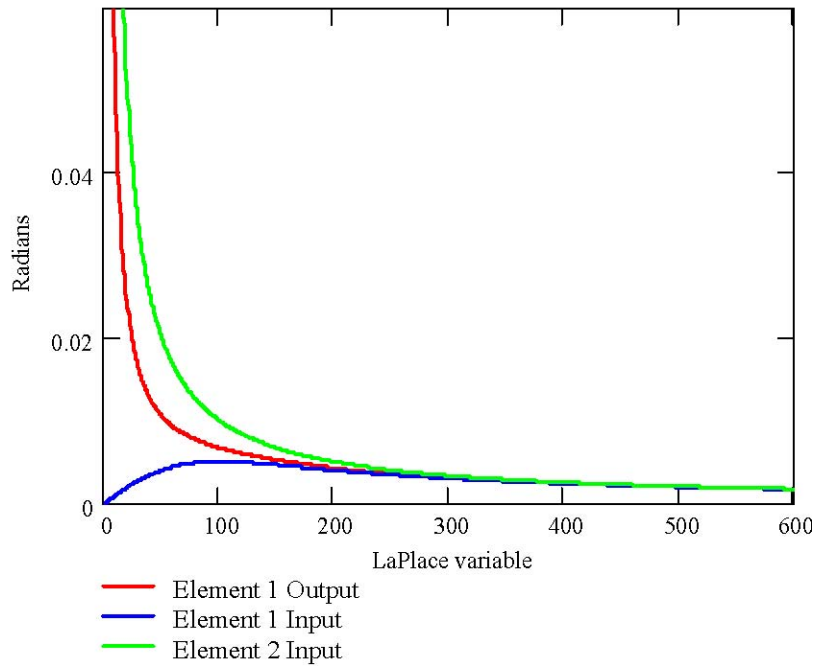
$$a2 := 4000$$

Case 4

$$\Delta\phi2(svar) := \frac{1}{svar}$$

$$\Delta\phi1(svar) := \frac{svar}{svar^2 + (a1)^2}$$

$$\delta\phi1(svar) := \frac{[(BW + svar) \cdot \Delta\phi1(svar) + \Delta\phi2(svar) \cdot BW]}{2 \cdot BW + svar}$$



Case 5

$$BW := AE \cdot KPM \cdot \frac{KSUM}{\tau}$$

$$a1 := 100$$

$$BW = 109.913W$$

Define the frequencies used.

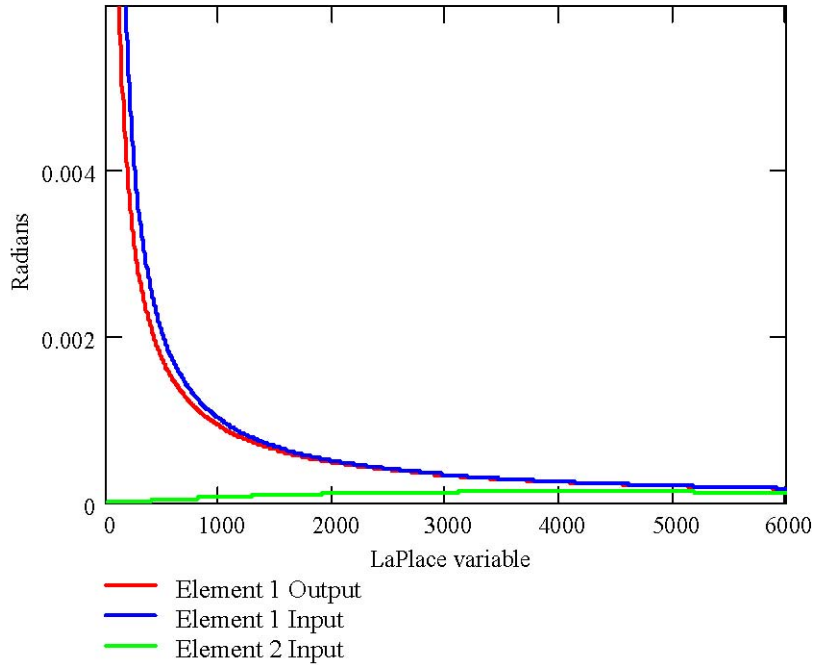
$$a2 := 4000$$

Case 5

$$\Delta\phi1(svar) := \frac{1}{svar}$$

$$\Delta\phi2(svar) := \frac{svar}{svar^2 + (a2)^2}$$

$$\delta\phi(svar) := \frac{[(BW + svar) \cdot \Delta\phi1(svar) + \Delta\phi2(svar) \cdot BW]}{2 \cdot BW + svar}$$



Case 6

$$BW := AE \cdot KPM \cdot \frac{KSUM}{\tau}$$

a1 := 100

BW = 109.913W

Define the frequencies used.

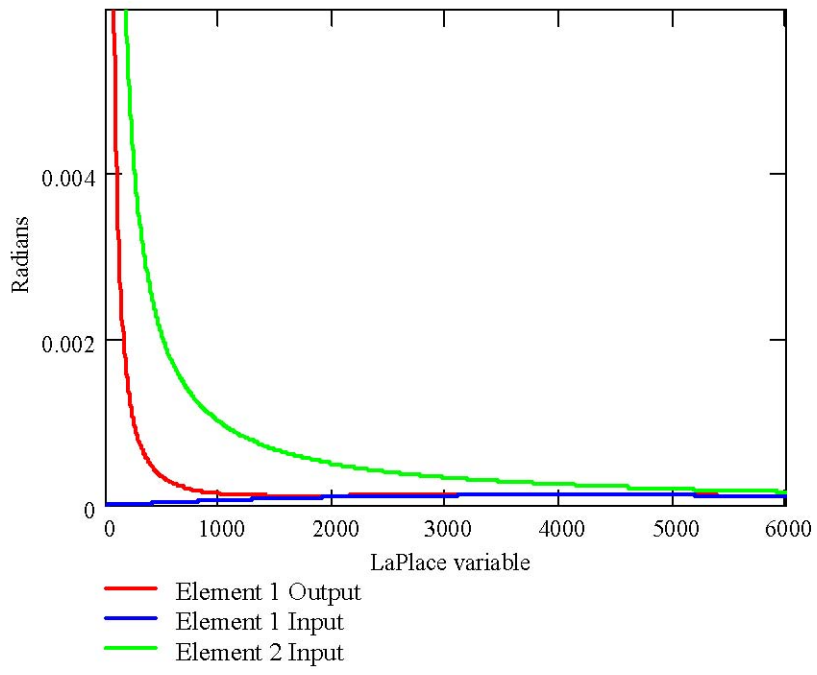
a2 := 4000

Case 6

$$\Delta\phi_2(svar) := \frac{1}{svar}$$

$$\Delta\phi_1(svar) := \frac{svar}{svar^2 + (a2)^2}$$

$$\delta\phi(svar) := \frac{[(BW + svar) \cdot \Delta\phi_1(svar) + \Delta\phi_2(svar) \cdot BW]}{2 \cdot BW + svar}$$



References

1. Shwartz, J, Wilson, G. T., & Avidor, J. (2002). Tactical High Energy Laser. SPIE Proceedings on Laser and Beam Control Technologies, Vol. 4632.
2. Seeley, D., Neice, M., Slater, J. & Mani, S. (2009). HEL-JTO Programs in Directed Energy. PhAST Proceedings on Defense Applications of Lasers and Electro-Optics Technologies, PWA3.
3. McNaught, S.J., Komine, H., Weiss, S. B., Simpson, R., Johnson, A. M. F., Machan, J., Asman, C. P., Weber, M., Jones, G. C., Valley, M. M., Jankevics, A., Burchman, D., McClellan, M., Sollee, J., Marmo, J., & Injeyan, H. (2009). 100 kW Coherently Combined Slab MOPAs. CLEO Proceedings on High power Solid-State Lasers, CLEO Symposium I: Multikilowatt Solid-State Lasers, CTHA1.
4. Augst, S. J., Goyal, A. K., Aggarwal, R. L., Fan, T. Y., & Sanchez, A. (2003). Wavelength Beam Combining of Ytterbium Fiber Lasers. Optics Letters, Vol. 28, No. 5, 331-333.
5. Shay, T. M., Baker, J., Robin, C., Vergien, C., Zeringue, C., Gallant, D., Sanchez, A., Pilkington, D., Bronder, T. J., & Lu, C. A. (2008) Active Phasing of Fiber Amplifier Arrays Using LOCSET. Proceedings from the Solid State Diode and Laser Technology Review.
6. Augst, S. J., Fan, T.Y., & Sanchez, A. (2004). Coherent Beam Combining and Phase Noise Measurements of Ytterbium Fiber Amplifiers. Optics Letters, Vol. 29, No. 5. 474-476.
7. Jones, D. C., Stacey, C. D., & Scott, A. M. (2007). Phase Stabilization of a Large-mode-area Ytterbium-doped Fiber Amplifier. Optics Letters, Vol. 32, No. 5. 466-468.
8. Desuivre, E. (1994). Erbium-Doped Fiber Amplifiers. John Wiley & Sons, Inc.
9. Paschotta, R., Nilsson, J., Tropper, A. C., & Hanna, D. C. (1997). Ytterbium-Doped Fiber Amplifiers. IEEE Journal of Quantum Electronics, Vol. 33, No. 7, 1049-1056.
10. Boyd, R. W. (2003). Nonlinear Optics, Second Edition. Academic Press.
11. Bass, M. (2001). Handbook of Optics, Volume IV Fiber Optics & Non Linear Optics. McGraw-Hill.
12. Henry, C. H. (1982). Theory of the Linewidth of Semiconductor Lasers. IEEE Journal of Quantum Electronics, Vol. QE-18, No. 2, 259-264.

13. Crowle, G. J. (1994). Narrow-linewidth Erbium-doped Fibre Lasers. Ph.D. Dissertation, University of Southampton (United Kingdom).
14. Yariv, Y. (1976). Introduction to Optical Electronics. Holt, Rinehart & Winston.
15. Möller, L. (1998). Novel Aspects of Spectral Broadening Due to Fiber Amplifier Phase Noise. IEEE Journal of Quantum Electronics, Vol. 34, No. 9. 1554-1558.
16. Nicolaescu, R., Walther, T., Fry, E. S., & Muendel, M. (1999). Ultranarrow-linewidth, Efficient Amplification of Low-Power Seed Sources by a Fiber Amplifier. Applied Optics, Vol. 38, No. 9, 1784-1787.
17. Höfer, S., Liem, A., Limpert, J., Zellmer, H., Tünnermann, A., Unger, S., Jetschke, S., Müller, H.-R., & Freitag, I. (2001). Single-frequency master-oscillator fiber power amplifier system emitting 20 W of power. Optics Letters, Vol. 26, No. 17, 1326-1328.
18. Cancio, P., Zeppini, P., De Natale, P., Taccheo, S., & Laporta, P. (2000). Noise Characteristics of a High power Ytterbium-doped Fibre Amplifier at 1083 nm. Applied Physics B. Vol. 70. 736-738.
19. Jones, D. C., & Scott, A. M. (2007). Characterisation and stabilising dynamic phase fluctuations in large mode area fibres. Proc. of SPIE Fiber Lasers IV: Technology, Systems, and Applications, Vol. 6453.
20. Shay, T. M., (2006). Theory of Electronically Phased Coherent Beam Combination without a Reference Beam. Optics Express, Vol. 14. 12188-12195.
21. Arfken, G. (1970). Mathematical Methods for Physicists. Academic Press.
22. Shay, T. M., Benham, V., Baker, J. T., Sanchez, A. D., Pilkington, D., & Lu, C. A. (2007). Self-Synchronous and Self-Referenced Coherent Beam Combination for Large Optical Arrays. IEEE Selected Topics in Quantum Electronics, Vol. 13, No. 3. 480-486.
23. Nabors, C. D. (1994). Effects of Phase Errors on Coherent Emitter Arrays. Applied Optics, Vol. 33, No. 12. 2284-2289.